Development of Diagnostic Tools for Use in a Gas Turbine Engine Undergoing Solid Particulate Ingestion

Kristopher T. Olshefski

Dissertation submitted to the Faculty of the
Virginia Polytechnic Institute and State University
in partial fulfillment of the requirements for the degree of

Doctor of Philosophy
in
Aerospace Engineering

K. Todd Lowe, Co-Chair
Wing F. Ng, Co-Chair
Christine Gilbert
John Palmore Jr.

April 19, 2023
Blacksburg, Virginia

Keywords: foreign object damage, engine health monitoring, particle ingestion, particle-laden flow, gas-solid flow

Development of Diagnostic Tools for Use in a Gas Turbine Engine Undergoing Solid Particulate Ingestion

Kristopher T. Olshefski

(Abstract)

Aircraft propulsion systems can be exposed to a variety of solid particulates while operating in either arid or other hazardous environments. For conventional takeoff and landing aircraft, debris can be ingested directly into the gas turbine powerplant which is exposed to the ambient environment. For helicopters and other vertical takeoff and landing (VTOL) aircraft, rotor down wash presents a particular threat during takeoff and landing operations as significant amounts of ground-level particles can be entrained in the surrounding air and subsequently ingested into the engine. Prolonged exposure to particle ingestion events leads to premature engine wear and, in extreme cases, rapid engine failure. Expanding our current understanding of these events is the first step to enabling engine manufacturers to mitigate these damage mechanisms through novel engine designs.

The work described in this dissertation is aimed at increasing the scientific understanding of these ingestion events through the development of two distinct diagnostic instruments. First, an anisokinetic particle sampling probe is designed to be used for in-situ particle sampling inside of a gas turbine engine compressor. Offtake of particles during engine operation in dusty conditions will provide researchers with an improved understanding of particle breakage tendency and component erosion susceptibility. Both experimental and numerical investigations of the probe present a comprehensive realization of probe performance characteristics. Secondly, a novel particle visualization technique is developed to provide users with particle distribution and particle mass flow estimates at the inlet of a gas turbine engine. This technique yields both time-resolved and time-averaged quantities, allowing users to have a comprehensive account of particles entering the engine.

(262 words)

This work was supported by the Office of Naval Research under grant numbers N00014-20-1-2538 and N00014-21-1-2397.

Development of Diagnostic Tools for Use in a Gas Turbine Engine Undergoing Solid Particulate Ingestion

Kristopher T. Olshefski

(General Audience Abstract)

Foreign debris ingested into aircraft engines can cause serious damage and degrade their performance. The source of these ingested particles may be from atmospherically suspended ash due to volcanic eruption, high altitude ice crystals, or ground-level sand and dust. Both conventional takeoff and landing aircraft and vertical takeoff and landing (VTOL) aircraft are at risk. In extreme cases, exposure to a particle-laden atmosphere has resulted in catastrophic engine failure and loss of life. For this reason, researchers are intensely focused on mitigating the effects of these harmful particulates.

The work described in this dissertation establishes two novel diagnostic capabilities. These are aimed at providing the research community with an increased understanding of how particles enter an aircraft powerplant as well as describe the behavior of these particles as they traverse the initial stages of an engine. The first instrument described is a particle sampling probe which is meant to be inserted into the compressor section of a gas turbine engine. This probe will offtake particles as they enter the engine after they have had an opportunity to interact with the rotating components of the compressor. In doing so, researchers gain an improved understanding of particle breakage tendency and component erosion susceptibility. The second instrument provides a snapshot of particle distribution at the inlet of the engine as well as estimates of total particle mass flow. This capability allows researchers to have a precise understanding of the quantity of ingested material as well as a qualitative understanding of how the inflow distribution of particles looks. Each of the developed tools represent a first step to enabling engine manufacturers to mitigate these damage mechanisms through novel engine designs.

Dedication

Dedicated to the memory of my late grandfather, to whom I owe… so much. And who taught me what it means to be a good man. I miss our talks greatly. But, I know that you are still here, *Vibrating to a different measure — behind a veil I cannot see through.*

> *Picture a wave. In the ocean. You can see it, measure it, its height, the way the sunlight refracts when it passes through. And it's there. And you can see it, you know what it is. It's a wave.*
>
> *And then it crashes on the shore and it's gone. But the water is still there. The wave was just a different way for the water to be, for a little while. You know it's one conception of death for Buddhists: the wave returns to the ocean, where it came from and where it's supposed to be.*

And to my wife, Paige, whose countless sacrifices have made this journey possible and whose love makes me feel like anything is possible. Without you, there is no *Why*. I love you more than I have ever found a way to say to you. I am the luckiest. I can't wait to see what the next chapter holds.

> *"What is REAL?" asked the Rabbit one day, when they were lying side by side near the nursery fender, before Nana came to tidy the room. "Does it mean having things that buzz inside you and a stick-out handle?"*
>
> *"Real isn't how you are made," said the Skin Horse. "It's a thing that happens to you. When a child loves you for a long, long time, not just to play with, but REALLY loves you, then you become Real."*
>
> *"Does it hurt?" asked the Rabbit.*
>
> *"Sometimes," said the Skin Horse, for he was always truthful. "When you are Real you don't mind being hurt."*
>
> *"Does it happen all at once, like being wound up," he asked, "or bit by bit?"*
>
> *"It doesn't happen all at once," said the Skin Horse. "You become. It takes a long time. That's why it doesn't happen often to people who break easily, or have sharp edges, or who have to be carefully kept. Generally, by the time you are Real, most of your hair has been loved off, and your eyes drop out and you get loose in the joints and very shabby. But these things don't matter at all, because once you are Real you can't be ugly, except to people who don't understand."*

Acknowledgements

None of this would have been possible without the countless people who have helped and encouraged me throughout this process. I'd like to first express my heartfelt appreciation to my advisors, Dr. Todd Lowe and Dr. Wing Ng, for their unwavering support, guidance, mentorship, and technical expertise. They have played a crucial role in shaping me into the researcher I am today. Their dedication has greatly contributed to the significant improvement of my capabilities since my arrival at Virginia Tech. I consider it a genuine honor to have had the opportunity to work under both of you and learn from your wealth of knowledge. I would also like to express my appreciation to my dissertation committee members, Dr. Christine Gilbert and Dr. John Palmore Jr., for their invaluable support, encouragement, and guidance throughout my research. Their expert advice helped me to refine my research focus and complete my dissertation successfully. I feel immensely grateful to have had the opportunity to work with Dr. Gwi Bo Byun and Mr. John Gillespie, whose contributions have been instrumental to this project's success. Countless hours of head-scratching, long conversations, and late nights have culminated in work that I am proud of. I am deeply appreciative of their patience and guidance throughout the process. I would also like to thank Diana Israel, Sherry Gong, Gregg Perley, Randall Monk, and Jason Doby, who without this dissertation would not have been possible. To say that their contributions in purchasing, scheduling, moving, machining, constructing, philosophizing, and problem-solving were critical to the successful completion of this work would be an understatement. Their enduring dedication and tireless efforts were absolutely essential. Finally, I have had the pleasure to work along side some truly amazing peers whose advice, friendship, and insight have enriched my time at Virginia Tech. I would like to specifically thank Dr. Adit Acharya, Dr. Sean Powers, Dr. Aldo Gargiulo, Dr. Carlos Michelen-Ströfer, Tomas Vlach, Brandon Weindorf, Dhruv Apte, and Jared Banks. I consider myself fortunate to have crossed paths with all of you, and I wish each of you the best of luck in your future endeavors.

Kristopher Olshefski

April 2023

Contents

List of Figures

List of Tables

[this page intentionally left blank]

1. Introduction

The performance of aircraft propulsion systems can be significantly affected by a variety foreign objects which may be encountered while operating under diverse conditions. In particular, the ingestion of solid matter from natural phenomena such as sandstorms and volcanic eruptions can cause engine failure within minutes of exposure. Although many studies have explored the effects of particle ingestion on the component level through computational and experimental means, few studies have focused on full-engine tests to determine the impacts these ingestion events can have on the entire propulsion system.

Providing a comprehensive account of the behavior of particles as they traverse an gas turbine power plant would be incredibly valuable to researchers and engine manufacturers alike. Having a complete description of these events and their effects would allow for tailored preventative measures to be implemented in key areas of these systems and could ultimately lead to engine life extension. Due to the complex and expensive nature of engine deterioration tests, effective diagnostic tools are essential to ensuring the maximum amount of information can be taken from each experimental investigation.

The research in this dissertation focuses on the development of an engine test cell facility at Virginia Tech as well as the development and application of two diagnostic tools for use in engine tests whereby particle ingestion is taking place. The development of the Virginia Tech particle ingestion research test cell provides researchers with a means for investigating this phenomena on full-scale engine tests, a unique capability for a university. Next, a novel particle illumination technique is presented. This method allows users to visualize particles as they enter the inlet plane of a gas turbine engine and is the first step in providing the research community with a comprehensive picture of the behavior of particles as they traverse the engine. This capability is especially beneficial for computational researchers as it provides a complete and accurate account of the distribution of particles present at the inlet, allowing for a more accurate assignment of simulation boundary conditions. The second diagnostic tool presented is a physical probe which is capable of capturing particles as they move through the engine. By sampling these particles and analyzing their size and shape, researchers can gain valuable insight into particle breakage trends and preferential concentration of particles at various locations throughout the engine. These contributions serve as the foundation for a longstanding research program investigating engine-particle interaction at Virginia Tech.

1.1 Structure and Content

This dissertation consists of eight chapters, as described below:

Chapter 1 introduces the topics, contributions, and achievements of the present dissertation.

Chapter 2 provides a review of highly relevant literature to inform the reader of the body of work which has been previously investigated, with emphasis on the gaps addressed by the present dissertation.

Chapter 3 is a peer-reviewed conference proceeding which has been accepted to the 2023 American Society of Mechanical Engineers Turbomachinery Technical Conference & Exposition. This paper provides a description of the Virginia Tech particle ingestion research test cell and details some of its capabilities.

Chapter 4 is a research article which is currently under preparation for submission to the journal *Measurement Science and Technology* entitled, "An illumination scattering technique for measuring particle distribution at a gas turbine engine inlet". This work presents a novel particle distribution visualization technique which provides users with a qualitative and quantitative description of particles as they enter a gas turbine engine.

Chapter 5 is a peer-reviewed research article published in the journal *Frontiers in Mechanical Engineering* entitled, "Development of an anisokinetic particle sampling probe for use in a gas turbine engine compressor". Here, a novel particle sampling instrument is presented and performance is demonstrated in a free jet at engine relevant flow conditions.

Chapter 6 is a standalone chapter which provides a detailed explanation of an experimental investigation of the sampling instrument introduced in Chapter 5. The results in this chapter offer valuable conclusions about the probe's performance which are not available from previous data. However, additional work will need to be done to make this work comprehensive enough for archival publication.

Chapter 7 is a standalone chapter which serves as the basis for a publication to be finalized at a later date. In this chapter, the results of Chapter 5 are revisited and computational tools are used to assess the aerodynamic performance of the previously described particle sampling probe. New insights are provided through numerical investigation.

Chapter 8 concludes the dissertation with a summary and an outlook for future work.

While several chapters have been submitted to journals which require specific formatting, all work included has been formatted to match the dissertation format. As such, these chapters will differ in appearance from their published format.

1.2 Attributions

The research presented in this dissertation was planned and conducted under the guidance of the two co-chairs of the Ph.D. degree committee.

Dr. K. Todd Lowe serves as the primary advisor and committee co-chair for the creation of the present dissertation. He provided considerable guidance for the planning, data acquisition, data analysis, and writing involved. Additionally, he acquired funding funding that partially supported this project in partnership with Dr. Ng.

Dr. Wing F. Ng serves as the co-advisor and committee co-chair for the creation of the present dissertation. He supervised and provided extensive feedback on the planning, data acquisition, data analysis, and writing involved. Additionally, he acquired funding that partially supported this project in partnership with Dr. Lowe.

Dr. Gwi Bo Byun and John Gillespie are research scientists at the Advanced Propulsion and Power Lab. They provided extensive feedback and assisted in the experiment detailed in Chapter 4.

Tomas Vlach, Britt Antous, Addison Collins, and Thomas Coulon are fellow graduate students who provided assistance and editorial guidance for work presented in Chapters 3, 4, and 5.

1.3 Achievements

The major achievements of this work are:

- Experiments were performed using a turboshaft engine operating at ground idle conditions to measure the inlet distribution of solid particulates being ingested. An illumination imaging technique was designed, developed, and implemented to calculate and validate the particle mass flow rate and local concentration mapping of the ingested material.
- A particle sampling probe has been developed to capture solids from a particle-laden flow. Particles as large as 1.3 mm were sampled at Mach numbers where M = (0.25, 0.70) and yaw angles ranging from 0° to 45° relative to free stream, conditions not previously investigated.

- Experiments were performed whereby the previously described imaging technique and sampling probe were coupled together to assess the accuracy of concentration measurements made by the probe. To the author's knowledge, this is the first evidence to support the local concentration value which is reported by the sampling probe, a significant step toward realizing the initial objective of the instrument.
- Observation of aerodynamic deficiencies in the previously described sampling probe have been investigated using computational analysis. Based on these findings, design improvements have been advised and potential efficiency gains have been quantified.

1.4 List of Publications

This list contains all scientific publications associated with the author which are relevant to the current dissertation, including those whose results are not included herein.

Peer-reviewed Journal Publications

- **Olshefski, K.**, Collins, A., Coulon, T., Lowe, T., Ng, W. (2022) "Development of an Anisokinetic Particle Sampling Probe for Use in a Gas Turbine Engine Compressor", *Front. Mech. Eng.* 8:951986. doi:10.3389/fmech.2022.951986
- **Olshefski, K.**, Byun G., Lowe, T., Ng, W. (2023) *"An Illumintation Scattering Technique for Measuring Particle Distribution at the Inlet Plane of a Gas Turbine Engine"*, Measurement Science and Technology, Manuscript under preparation.

Peer-reviewed Conference Proceedings

- Vlach, T.,**Olshefski, K.**, Bunin, D., Ehlers, A., Caddick, M., Lowe, T., Ng, W. (2023) *"Analysis of C-Spec Particle Breakage in a Turbine Engine Particle Ingestion Test Cell"*, *Proceedings of the ASME Turbo Expo 2023: Turbomachinery Technical Conference and Exposition*. Boston, Massachusetts, USA. June 26–30, 2023.

Conference Proceedings

- **K. Olshefski**, A. Collins, T. Coulon, W. Ng, T. Lowe *Development of a particle sampling probe for use in a gas turbine engine compressor.* First International Conference on Advanced Instrumentation, Diagnostics and Controls for Applications in Turbomachinery (AIDCAT), State College, PA. 2022.

- T. Vlach, **K. Olshefski**, W. Ng, T. Lowe *Virginia Tech Particle Ingestion Research Test Cell.* First International Conference on Advanced Instrumentation, Diagnostics and Controls for Applications in Turbomachinery (AIDCAT), State College, PA. 2022.

2. Literature Review

The primary research areas focused on within this dissertation are aerodynamic probe development, particle-laden flows, and particle visualization, three heavily researched areas. Therefore, the literature presented below aims to present the current state of theory and application of these concentrations. However, there are aspects of the problem statement which are outside of the scope of the current investigation. For example, the particle sampling probe will be positioned within an operational rotating axial compressor environment. While the complex flow within a compressor will certainly have an effect on the particles (and thereby probe performance) through the introduction of vane interaction, vortex shedding from blade trailing edge, shocks, acoustic waves, etc., consideration for these dynamics is not necessary for a first order estimation of probe performance, which is the intent of this work. The interested reader is directed to the recent work of Sandberg and Michelassi for a review of axial turbomachinary fluid dynamics [1]. Similarly, the visualization technique described below does not attempt to characterize particles which are smaller than the wavelength of the incident light. Such particles would be described by Rayleigh scattering theory instead of Mie scattering theory. The reader is directed to [2] for a current review of this material.

2.1 Particle-laden Flows

Describing a system as a particle-laden flow can include a multitude of scenarios. However, investigations of gas flows entrained with solid inertial particles (particles which do not respond easily to changes in fluid flow) are of particular interest to researchers due to their near ubiquity in industrial and natural flows and will be the primary focus of this work. Literature shows that these flows are incredibly complex and continue to challenge computationalists and experimentalists alike. Recent advancements in computational power and measurement capabilities have reignited interest in these flows within the research community. This has led to a significant body of literature which has been summarized herein to inform the current investigation. We will restrict the following discussion to spherical rigid particles with density greater than the fluid in which they are suspended. For a discussion on the effects of non-sphericity, the recent review of Voth and Soldati provides an exceptional commentary [3].

2.1.1 Characterization

Like many engineering and fluids related problems, the determination of relevant non-dimensional parameters is invaluable to adequately characterizing and defining the system as well as gaining a high-level understanding the behavior of the flow. In the following discussion, we highlight common parameters of interest to particle-laden flows in an attempt to extrapolate their effects to our flow scenario. The parameters which characteristically define a gas-particle flow include the density ratio, size ratio, particle concentration, and Stokes number. Undoubtedly, the number of particles suspended in a given flow relative to the overall structure can dominate the behavior of that system. For example, having relatively few particles in a flow, it may be easy to assume the particles do not interact with each other. Conversely, as the number of particles gets very large particle-particle interactions become increasingly common and may be necessary for a researcher to include in analysis. This parameter, commonly referred to in literature as the particle volume fraction, particle density, or simply as the particle concentration, can be expressed several different ways. First, consider the mass flow ratio given by

$$m = W/Q \tag{2.1}$$

where $W \& Q$ are the mass flow rates of the particles and the fluid, respectively. If we multiply the mass flow ratio (m) by the density of the fluid (ρ_f), we can determine the flow concentration $c(kg/m^3)$ as

$$c = m\rho_f. \tag{2.2}$$

Dividing out the density of the particles (ρ_p), we arrive at the non-dimensionalized volumetric concentration

$$c_{\mathcal{V}} = c/\rho_p. \tag{2.3}$$

It is easy to see that the non-dimensional volumetric concentration can be equivalently expressed using the total number of particles in a flow (N) and the ratio of particle to total volume as

$$\Phi = \frac{N \mathcal{V}_p}{\mathcal{V}_T} \tag{2.4}$$

where $\mathcal{V}_p$ is the volume of an individual particle and $\mathcal{V}_T$ represents the entire volume of the system. This term is typically called the particle volume fraction (Φ) and is the most commonly referenced parameter with respect to concentration in literature [4]. This is the most common distinguishing feature between characterizing a flow as either dense or dilute which is a distinguishing feature of studies [5]. A dense flow may represent a system such as a slurry or a granular flow while a dilute flow may be representative of a dusty gas as is the case in the current investigation. Depending on the level of particle volume fraction, phase coupling considerations become important [6]. This will be expanded upon in later discussion.

Another non-dimensional quantity of importance is the Stokes number(St). This value is a ratio of particle to fluid inertia and represents how quickly a particle responds to changes in the surrounding velocity field. Particles with $St \leq 1$ tend to follow streamlines of the flow while particles with $St > 1$ remain unaffected by changes in the surrounding flow field. The Stokes number associated with particle velocity is defined as

$$St = \frac{\tau_p}{\tau_f} \tag{2.5}$$

where τ_p is the momentum response time of a particle and the characteristic time scale of the carrier phase is τ_f [7]. The particle response time is typically represented as

$$\tau_p = \frac{\rho_p d_p^2}{18\mu_f}. \tag{2.6}$$

While several different iterations of the Stokes number can be defined, typically this quantity is expressed as

$$St = \frac{\rho_p d_p^2 U_B}{18\mu_f D} \tag{2.7}$$

where d_p is the particle diameter, U_B is the fluid bulk velocity, μ_f is the fluid dynamic viscosity, and D is the characteristic diameter of the flow [7]. This definition assumes a low Reynolds number limit (Stokes flow) but, is the standard definition used in relevant literature [8, 9]. Examining Figure 2.1 we can see that for large particles with high Stokes number, and high density ratios, geometric effects become increasingly dominant, particle settling behavior is inversely proportional to Stokes number, and inertial clustering likelihood increases with density ratio and is maximized where particle diameter is approximately on the order of the Kolmogorov length scale (η). The ratio of particle to fluid density can have a dramatic impact on the particle behavior in a given flow. Low density ratios can result in gravitational settling while high density ratios can produce flows with inertial clustering [10]. Particle size ratio can be incredibly valuable in assessing the dependence of the system on wake effects. As the diameter gets close to and exceeds the Kolmogorov length scale, turbulence modification may become significant [10].

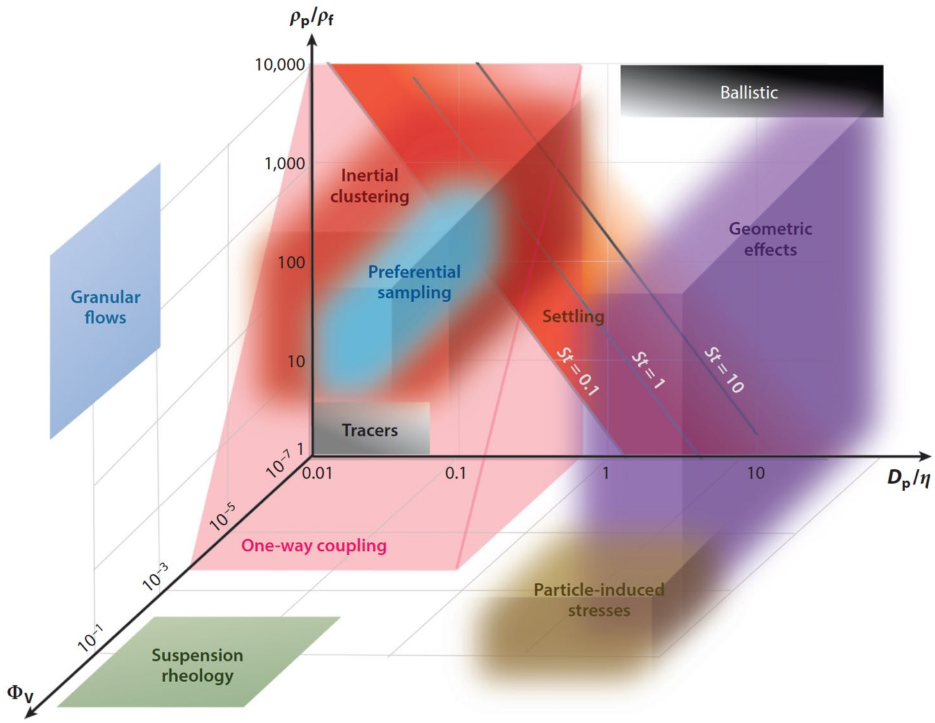

Figure 2.1: Three-dimensional characterization map of Brandt & Coletti [10]

2.1.2 Computational Investigations

Much of the recent literature surrounding particle-laden flows is focused on enhancing high-order models such as particle-resolved direct numerical simulations (PR-DNS) [11] or increases capabilities of Large Eddy Simulations(LES) [12] as these simulations still present considerable challenge despite recent advancements in computational power. However, Reynolds Averaged Navier-Stokes Simulations (RANS) remain the workhorse of industry due to their low computational expense. Within the computational community its recognized that method selection (DNS vs. LES vs. RANS) often attempts to strike balance between numerical accuracy and simulation time. Often, acceptable results may be achieved through low fidelity models even though they do not comprehensively capture the physics of the flow. Having an understanding of model limitations is critical in making the decision as to whether low fidelity modeling is robust enough to consider for evaluation of a given system. Additionally, it is important to recognize that the limitations that exist in higher fidelity models may also be present in RANS simulations and having an understanding of the reaches of these issues can ensure a researcher is properly informed prior to starting simulations. For example, if particle dispersion is of particular interest to a research prob-

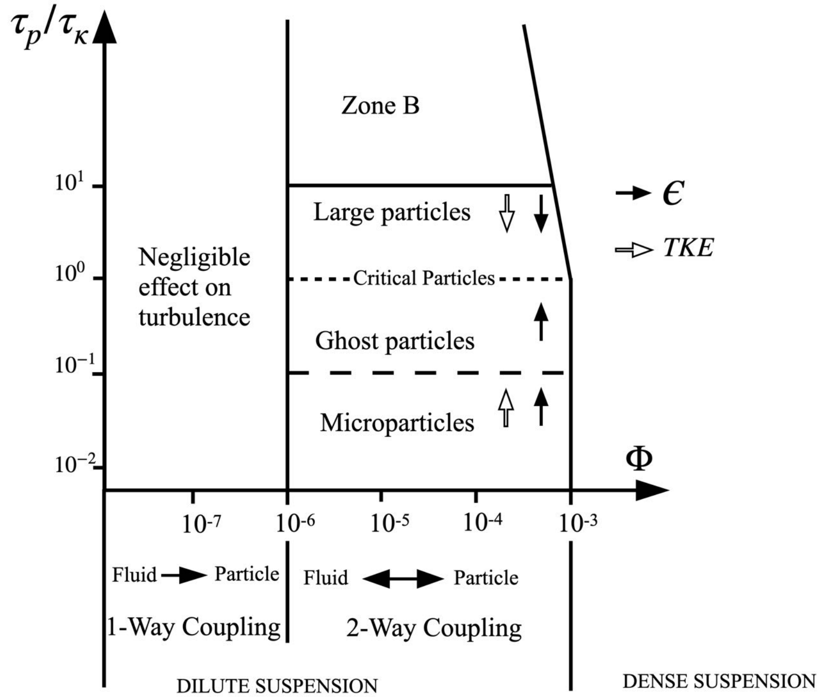

Figure 2.2: Classification map of Elghobashi [4]

lem and the highest fidelity models are unable to accurately capture these dynamics, it would be unwise to draw conclusions about dispersion patterns from results provided by a model which is of lower fidelity. However, the detailed complexities of model development for these flows is outside the scope of the current investigation. Instead, focus will be on lessons learned from successful implementations of RANS simulations in particle-laden flows and how their application may inform the current investigation.

As previously discussed, particle volume fraction should be a primary consideration in model selection as it is a dominate characterization feature of a flow. The classification map shown in Figure 2.2 first introduced by Elghobashi in [13] and later expanded upon in [4], provides a framework for the degree of phase coupling necessary for a given simulation based on Stokes number and particle volume fraction. Here we see that for very dilute suspensions, a one-way coupling scheme should be sufficient. As particle volume increases, Stokes number will dictate turbulence modulation behavior and two-way coupling schemes should be considered. For very dense flows ($\Phi \geq 10^{-3}$), four-way coupling may be necessary. The validity of this map was recently reinforced for gas-solid flows by Peterson et. al. [14].

The predominant method of introducing phase coupling used in commercial and non-commercial

CFD codes is through the point-particle approach. This approach stems from the Maxey-Riley-Gatigol equation which describes the equation of motion for a small rigid sphere in non-uniform motion [15, 16]. The governing equations of motion for an incompressible Newtonion fluid which is laden with point particles are

$$\begin{aligned} &\frac{\partial u_i}{\partial x_i} = 0 \\ &\frac{\partial u_i}{\partial t} + \frac{\partial u_i u_j}{\partial x_j} = \frac{-1}{\rho}\frac{\partial p}{\partial x_i} + v\frac{\partial^2 u_i}{\partial x_j \partial x_j} - \frac{1}{\rho_f} f_{pi} \end{aligned} \tag{2.8}$$

where f_{pi} is a local force which is applied by the fluid onto particles and gravity has been neglected [17]. Despite being the predominant method used in CFD, the point particle approach is not without shortcomings, especially for high Re applications [10]. Namely, point particle methods do not show good agreement with transport and dispersion behavior [18, 19]. Therefore, caution should be taken if these qualities are of particular relevance to the research problem.

It is now commonplace for researchers to incorporate simulation results with experimental findings due to the prevalence and accuracy of commercially available software. Dr. Widen Tabakoff, a pioneer in particle structure interaction, conducted extensive studies on the impacts of particles interacting with coupons in engine relevant conditions [20–29]. Subsequently he also conducted early simulations of particle trajectories through a single compressor stage [20, 21]. Longmire and Eaton conducted early studies on the sturcture of a particle-laden jet where they determined important information about jet spreading rate and the impacts that particle have on it [30]. Recently, Ghenaiet examined particle behavior through the first stage of a PW-JT8-D17 turbofan and analyzed the effects of varying concentration of MIL E-5007C (C-Spec) crushed quartz [31, 32]. Saxena explored modeling flow laden with sand particles through a mulit-stage axial compressor and explored the impacts of centrifugal forces on particle behavior as particle traversed the system [33]. For these simulations, a $\kappa - \omega\, SST$ turbulence model was employed and effects of varying particle size were investigated. They found that large particles were more prevalent toward the compressor walls and that large particles were more affected by centrifugal force than smaller ones [33]. Of particular interest, a recent study provides an assessment of Euler-Lagrange particle tracking methods in RANS simulations using Ansys FLUENT [34]. The researchers showed that Ansys FLUENT is capable of adequately representing dilute dispersed phase flows to good agreement with experimental results for various canonical flows. The researchers also note that the flow domain should be simulated in three dimensions, even if it is reasonable to assume a 2D simplification. Neglecting to do so results in incorrect particle dispersion.

2.1.3 Experimental Techniques

The predominant approach to experimentally investigating particle laden flows is through the employment of imaging techniques which track particle motion namely, either Particle Image Velocimetry (PIV) or Particle Tracking Velocimetry (PTV). These techniques return either Eulerian or Lagrangian particle field information respectively [35]. These techniques were originally developed to visualize single-phase flow and many studies reinforce the robustness of these techniques in these regimes[36–38]. However, while investigations have adapted these techniques to dispersed phase flows, doing so should be approached with caution.

PIV uses small tracer particles which are sized to ideally match the velocity and flow path of the surrounding fluid. Typically, these are a maximum of $1\mu m$ in diameter and uniformly sized[35]. Carter et. al. comment that while PIV measurements provide a robust description of main velocity components, the technique is bound to correlated motion of the flow. But, residual uncorrelated motion can be critical to the evolution of the flow in polydispersed, inertial flows [39]. PTV techniques contrast PIV techniques in that they aim to track individual particle motion across several successive images [40]. This strategy may become compromised if inertial particles collide with one another or with objects in the flow or walls [10]. Additionally, one well-known limitation of PTV that can be exacerbated in particle-laden flows is that high particle density may limit the ability to track particles [39]. It has been suggested that a method for fully characterizing a particle-laden flow is to use simultaneous PIV/ PTV techniques on the carrier and dispersed phases, respectively [10]. In this vein, Baker and Coletti showed that information from one technique, say the PIV velocity field, can be used to inform the other, the PTV algorithm in this case [41]. One approach to mitigating the complication of particle collision may be through the use of multi-camera volumetric imaging techniques which provide 3D reconstruction of particle trajectories [40]. The algorithm of of Schanz et. al. known as Shake-the-Box has made it possible to perform this technique with relevant particle number densities [42]. The approach works by ‘shaking’ particle images to improve particle matching between successive frames. This technique was recently demonstrated using inertial glass bead particles by Ebrahimian et. al. [43].

Although there have been efforts to understand particle flow paths through an engine and accurately depict particle behavior at the inlet plane, there is still a need for greater understanding in these areas. Papadopoulos et al. conducted preliminary level demonstrations of an in-situ particle detector that identifies plasma interaction and dissociation with particles to determine particle size and relative concentration [44]. Similarly, Moon et al. have developed a scattering-extinction based technique that leverages a machine-learning library to assess particle size, shape, and concentration at a gas turbine inlet [45, 46]. Additionally, others have sought to develop airborne instrumentation that can provide particle information about atmospheric aerosols and ice crystals [47–50]. Baumgardner et al. developed an on-wing instrument that combines five separate probes into one to assess atmospheric particle concentration and liquid water content [47]. However, these instruments typically sample particles in the sub-to-single-micron range and are point measurements rather than providing particle distribution over an area. Furthermore, each of these methods listed is limited by its complexity and does not yield a comprehensive description of the inlet particle distribution.

To address these limitations, significant effort has been aimed at capturing particle characteristics using extinction and scattering based planar imaging techniques, particularly in the liquid sprays field [51–53]. The Structured Laser Illumination Planar Imaging (SLIPI) technique, developed by Berrocal and Kristensson, is an optical-imaging technique primarily used to visualize a liquid spray and has become a primary characterization method in the atomization and sprays field [54–56]. Similarly, Gaigalas, Wang, and Choquette used a commercial spectrometer and integrating sphere to assess the scattering and absorption cross section of microspheres suspended in water, fitting the data with Lorenz-Mie scattering cross section and a correction factor to find the relative reduction in scattering cross section by absorption [57]. Evanoff and Chumanov showed that a method, termed standard subtraction, can be appropriate for determining the concentration of silver nanoparticles suspended in water independent of size or shape [58]. Lastly, Yu et al. developed a dust concentration measurement method based on laser scattering and showed that mass concentration has a linear relationship to scattered light intensity [59]. Despite these efforts, there is still room for improvement in understanding particle behavior in engines and providing a comprehensive description of the inlet particle distribution.

2.2 Aerodynamic Particle Sampling Probes

The use of aerodynamic probes immersed in flow has been a successful diagnostic approach for researchers for more than two centuries. The Pitot probe first introduced by Henri de Pitot in 1732 [60] and later improved upon by Darcy in 1858 [61] is now one of the most ubiquitous instruments used in aviation. A Pitot tube is a velocity measurement device which works by sensing differential pressure from the freestream and inside the tube. Then, using basic analysis techniques, the user can calculate current flow velocity [60]. In its simplest form, a pitot tube looks very much like a pipe with a 90 degree bend in it. There is an additional hole at some location on the tube where static pressure is sensed. While aerodynamic probes can now take on very different shapes, sizes, and purposes, they remain an invaluable tool for assessing complex flow conditions. Due to the rapid increase in computational abilities, it is becoming increasingly common to inform probe design decisions through informed computational fluid dynamics (CFD) studies. Recently, a study was conducted to determine the intrusive influence of a pressure probe placed downstream of an axial compressor stator row [62]. Researchers found that probe measurements with respect to an undisturbed test case may differ by as much as 30%. A radially traversing temperature probe for use on gas turbines was developed using CFD and Conjugate Heat transfer analysis [63]. Researchers were able to successfully modify existing probe geometries through insight gained using CFD analysis to increase efficiency and operating range [63]. Vincent et. al. also investigated the behavior of a total temperature probe using CFD and CHT. Here, the researchers gained an improved understanding of the probe geometry's influence on heat transfer properties [64]. Through this understanding, a generalized analysis methodology was presented for enhanced design capabilities. Shumeli et. al. used Ansys CFX RANS simulations to inform the design of a non-standard Pitot probe [65]. It is also possible to use sampling probes within gas-liquid systems. Researchers experimentally developed a novel sampling probe to sample void fraction for multi-phase flow characterization [66]. The resulting isokinetic sampling probe was used to take samples of a bubbly flow and samples provided researchers with a continuous local void fraction measurement.

Particle sampling studies can be traced to as early as the 1940's with the studies of Lapple and Shepard [67]. While the investigation of these systems has been ongoing for more than 80 years, their flawless deployment remains elusive due to several complexities. These may include particle bounce from wall interactions, particle-particle collisions, deposition, sampling probe intrusive effect on flow field, momentum transfer between phases, and departure from isokinetic conditions. However, this is not to say that progress has remained stagnant during this time. In fact, substantial progress has been made, particularly with regards to the isokinetic sampling of aerosol material.

2.2.1 Isokinetic Sampling

Foundational work on the development of isokinetic sampling systems is presented by Davies (1954), Watson(1954), Levin(1957), Badzioch(1959), and Davies(1968) [68–72]. Consideration for the effect of flow direction relative to sampling face has been studied in [73–75]. Measurement error due to anisokinetic sampling conditions has been extensively studied in [69, 76–80].

The literature shows that measurement error is minimized for a sampling probe that is sharp edged and thin-walled [81–83]. Measurement effect by probe bend is accounted by Sansone and Ruping [77, 84]. For large particles, there may exist a velocity slip between the carrier and dispersed phases [85]. This effect is investigated in [80, 86].

Isokinetic sampling systems are the standard method for capturing particulate samples from a moving gas stream. Achieving an isokinetic condition requires that the sampling probe be aligned isoaxially with the freestream and that the velocity at which the probe samples be equal to the undisturbed local flow velocity [85]. In this scenario, particles which are entrained in the flow upstream of the probe do not *"feel"* the effects of a body immersed in the flow. This ensures an undistorted stream tube upstream of the probe and assures particles flow smoothly into the probe. Meeting this condition is critical for accurate calculation of particle concentration and in many cases this can be achieved by aspirating the pressure within the probe with a suction flow [6]. Other work has modified inlet pressure by increasing the fluid temperature at the probe face by either a hot wire or electric heating [87]. Once particles have been sampled, it is customary to collect the sample to determine particle mass flux. To establish an accurate estimate of particle mass flow that mitigates effects of unsteady sampling, it is suggested that two samples, m_{p1} and m_{p2} be taken over two distinct sampling periods, Δt_1 and Δt_2 [88]. With these samples, a time-averaged particle mass flow rate can be established by

$$\dot{m}_p = \frac{m_{p1} - m_{p2}}{A(\Delta t_1 - \Delta t_2)} \tag{2.9}$$

where A is the effective sampling area [88]. This time-averaged particle mass flux can also be represented as a function of the time-averaged particle velocity U_p, the time-averaged particle concentration C_p, and the particle diffusive mass flux $\dot{m}_{pd}$ as

$$\dot{m}_p = U_p C_p + \dot{m}_{pd}. \tag{2.10}$$

Although, for fully-developed pipe flow, the diffusive mass flux may be negligibly small when compared to the particle mass flow rate [79]. So, what we learn from above is that a time-averaged particle concentration can be estimated given particle mass flux and the determination of time-averaged particle velocity. Literature suggests that for the sampling of aerosols, particle Reynolds number at terminal velocity remains within the Stokes regime for particles less than 60μm with a typical density of 2000 kg/m^3 [85]. For these particles, relaxation times are small($\leq 100ms$) and inertial range is short ($< 2cm$) , therefore assuming a no-slip velocity between particles and bulk

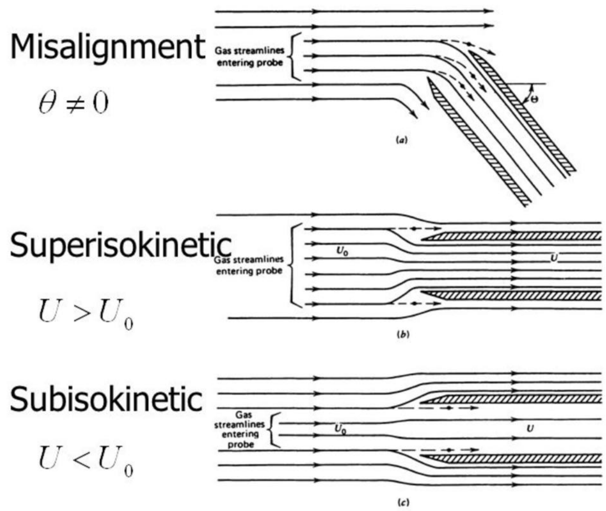

Figure 2.3: Anisokinetic Sampling Conditions (*taken from [88]*
)

flow may be appropriate [89]. This assumption may not be valid outside of this regime however.

2.2.2 Anisokinetic Sampling

While an isokinetic condition presents an ideal sampling scenario, this arrangement is rarely realized for practical flow applications. Instead, an anisokinetic condition occurs when sampling velocity does not match the bulk velocity, the sampling plane is not perpendicular to the freestream, or both. Flows with inconsistent or unsteady velocity fields make it impractical to reliably match the sampling velocity to that of the freestream. These cases motivate an investigation of the effects of anisokinetic conditions on the deviation from ideal measurement capability. As seen in Figure 2.3 the anisokinetic condition can be subdivided into three categories: super-ioskinetic, sub-isokinetic, and misalignment. If we again consider that the Stokes number provides information about how well a particle's trajectory follows flow streamlines, it is evident from the figure that small Stokesian particles will be over-sampled in a super-isokinetic condition. Those same particles will be under-sampled in a sub-isokinetic condition. Conversely, large particles ($St >> 1$) are inertially driven and are unaffected by the presence of the probe. Therefore, the mass flow measurement of very large particles is independent of the isokineticity. This conclusion is confirmed by Hemeon and Haines [90].

For small particles, such as aerosols, we previously discussed that it is reasonable to assume a negligible difference in particle and freestream velocity. In this case, the error in concentration can

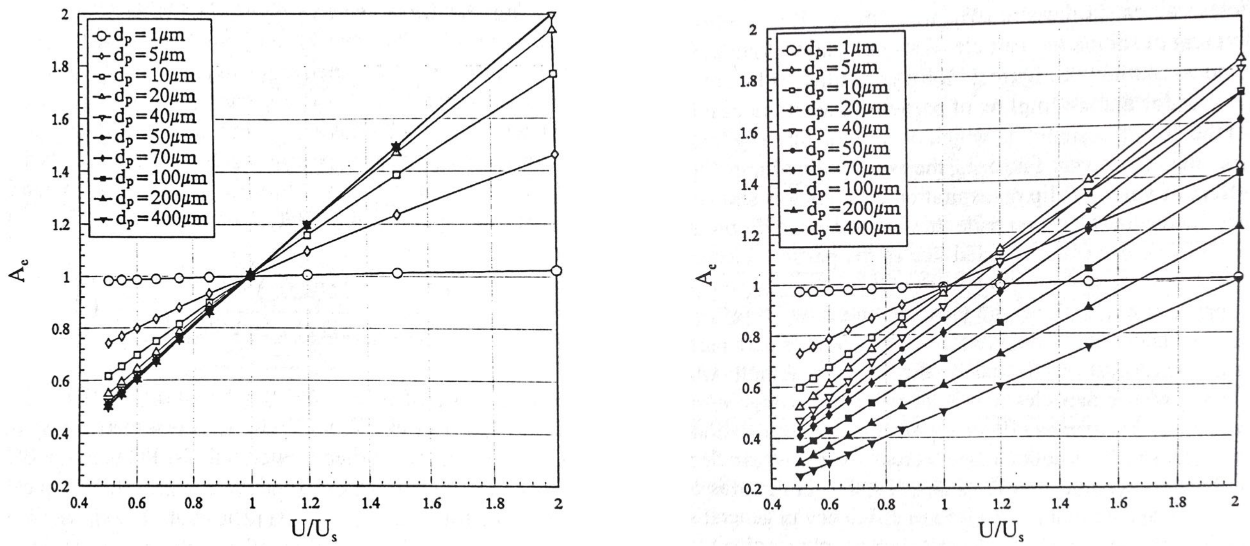

(a) No consideration of interphase velocity slip

(b) Interphase slip velocity considered

Figure 2.4: Anisokinetic Sampling Efficiencies (*taken from [80]*)

be estimated by the Aspiration efficiency A_e as

$$A_e = \frac{C_s}{C_0} = 1 + \frac{4St}{1 + 4St}(1 - \frac{U_0}{U_s}) \tag{2.11}$$

where C_s and C_0 are the freestream and particle concentrations, respectively, and U_0 and U_s are the freestream and particle velocities [72]. This equation matches well with experimental findings for the limiting cases of aerosol sampling, to include where $St >> 1$ [85]. However, this correlation was later improved upon by Belyaev and Levin as

$$A_e = 1 + \frac{(2 + 0.62U_s/U_0)St}{1 + (2 + 0.62U_s/U_0)St}(\frac{U_0}{U_s} - 1) \tag{2.12}$$

and is valid over the range of $0.18 < U_s/U_0 < 5$ and $0.18 < St < 2$ [91, 92]. Aspiration efficiency for typical aerosol particles can be seen in Figure 2.4a [85]. Additionally, the effects off considering a slip condition, which is necessary for very large particles can be seen in Figure 2.4b also from [85]. By inspection we see that even under isokinetic conditions, correct estimation of particle concentration is not practical for these ballistic particles. There has been suggestion within the aerosol sampling community that aspiration efficiency should be a function of Stokes number, yaw orientation, and particle to freestream velocity ratio [93]. It was found that for particles larger than $100\mu m$, sampling efficiency error can be as high as 10% for a yaw orientation of $25°$ [94].

The resulting adaptation of the aspiration efficiency was presented by Vincent as

$$A_e = 1 + [1 - \frac{1}{1 + GSt(cos\theta + 4\sqrt{(U_0/U_s)sin\theta})}](\frac{U_0}{U_s}cos\theta - 1) \tag{2.13}$$

where θ is yaw angle relative to freestream and $G = G(D, \theta, U_0/U_s)$ [95]. However, the author is unaware of a general form for G.

Despite the potential complexities associated with anisokinetic sampling, recent work has began exploring the utility of working within this constraint as the overwhelming majority of realistic flow scenarios present conditions where isokinetic sampling is impractical. The anisokinetic nozzle fitted with a surrounding shroud was first introduced by MacFarland as a method of sampling radio-nucleotide aerosols from the cooling stacks at nuclear facilities [96]. Chandra further demonstrated the utility of such a probe by showing an increased efficiency over that of the unshrouded probe [97]. Twohy implemented a similar design through CFD design analysis and showed that a shroud could be used to straighten particle trajectories to maintain an isokinetic condition [98]. This conclusion was then confirmed using wind tunnel testing. More recently, Heo improved upon this design by adding a double shroud to a sampling probe. This work resulted in the achievement of a sampling efficiency of unity at velocities not previously realized($M \approxeq 0.2$) [99, 100]. By surrounding a probe with a shroud, the flow becomes less dependent on flow direction as the flow can be straightened entering the shroud. Additionally, these probes sample at a standard rate as opposed to matching flow velocity like a standard isokinetic sampling probe. Although, not shielded, Briones introduced an internal dilution cross-flow to achieve isokinetic sampling conditions [101].

References

[1] R. D. Sandberg and V. Michelassi, “Fluid dynamics of axial turbomachinery: Blade- and stage-level simulations and models,” *Annual Review of Fluid Mechanics*, vol. 54, no. 1, pp. 255–285, 2022.

[2] S. Powers, G. Byun, and K. T. Lowe, “Auto-processing of filtered rayleigh scattering images including mie and background scattering contributions,” 2022.

[3] G. A. Voth and A. Soldati, “Anisotropic particles in turbulence,” *Annual Review of Fluid Mechanics*, vol. 49, no. 1, pp. 249–276, 2017.

[4] S. Elghobashi, *An updated classification map of particle-laden turbulent flows*. Springer, 2004, pp. 3–10.

[5] S. Balachandar and J. K. Eaton, "Turbulent dispersed multiphase flow," *Annual Review of Fluid Mechanics*, vol. 42, no. 1, pp. 111–133, 2010.

[6] Higashitani, *Powder Technology Handbook*, 2020.

[7] G. Rudinger, Ed., *Dedication*. Elsevier, 1980.

[8] J. D. Colmenares, M. M. Ameen, S. Wu, and S. Patel, *Large Eddy Simulation of Turbulent Particle-laden Jets using the Spectral Element Method*, 2021.

[9] A. A. Mostafa, H. C. Mongia, V. G. McDonell, and G. S. Samuelsen, "Evolution of particle-laden jet flows - a theoretical and experimental study," *AIAA Journal*, vol. 27, no. 2, pp. 167–183, 1989.

[10] L. Brandt and F. Coletti, "Particle-laden turbulence: Progress and perspectives," *Annual Review of Fluid Mechanics*, vol. 54, no. 1, pp. 159–189, 2022.

[11] J. Capecelatro and O. Desjardins, "An euler–lagrange strategy for simulating particle-laden flows," *Journal of Computational Physics*, vol. 238, pp. 1–31, 2013.

[12] R. O. Fox, F. Laurent, and A. Vié, "A hyperbolic two-fluid model for compressible flows with arbitrary material-density ratios," *Journal of Fluid Mechanics*, vol. 903, 2020.

[13] S. Elghobashi, *Particle-laden turbulent flows: direct simulation and closure models*. Springer, 1991, pp. 91–104.

[14] A. J. Petersen, L. Baker, and F. Coletti, "Experimental study of inertial particles clustering and settling in homogeneous turbulence," *Journal of Fluid Mechanics*, vol. 864, p. 925–970, 2019.

[15] M. R. Maxey, "Equation of motion for a small rigid sphere in a nonuniform flow," *Physics of Fluids*, vol. 26, no. 4, 1983.

[16] R. Gatignol, "The faxén formulae for a rigid particle in an unsteady non-uniform stokes flow." *Journal of Mechanical Theory: Applications*, vol. 2(2), pp. 143–160, 1983.

[17] J. K. Eaton, "Two-way coupled turbulence simulations of gas-particle flows using point-particle tracking," *International Journal of Multiphase Flow*, vol. 35, no. 9, pp. 792–800, 2009, special Issue: Point-Particle Model for Disperse Turbulent Flows.

[18] T. P. Sapsis, N. T. Ouellette, J. P. Gollub, and G. Haller, "Neutrally buoyant particle dynamics in fluid flows: Comparison of experiments with lagrangian stochastic models," *Physics of Fluids*, vol. 23, no. 9, p. 093304, 2011.

[19] J. G. M. Kuerten, "Point-particle dns and les of particle-laden turbulent flow - a state-of-the-art review," *Flow, Turbulence and Combustion*, vol. 97, no. 3, pp. 689–713, 2016. [Online]. Available: https://doi.org/10.1007/s10494-016-9765-y

[20] W. Tabakoff, "Review—turbomachinery performance deterioration exposed to solid

particulates environment," *Journal of Fluids Engineering*, vol. 106, no. 2, pp. 125–134, 1984. [Online]. Available: https://doi.org/10.1115/1.3243088

[21] ——, "Study of single-stage axial flow compressor performance deterioration," *Wear*, vol. 119, no. 1, pp. 51–61, 1987. [Online]. Available: https://www.sciencedirect.com/science/article/pii/0043164887900974

[22] G. Grant and W. Tabakoff, "Erosion prediction in turbomachinery resulting from environmental solid particles," *Journal of Aircraft*, vol. 12, no. 5, pp. 471–478, 1975.

[23] W. Tabakoff, A. Hamed, M. Metwally, and M. Pasin, "High-temperature erosion resistance of coatings for gas turbine," *Journal of Engineering for Gas Turbines and Power*, vol. 114, no. 2, pp. 242–249, 1992. [Online]. Available: https://doi.org/10.1115/1.2906579

[24] G. Grant and W. Tabakoff, "Erosion prediction in turbomachinery resulting from environmental solid particles," *Journal of Aircraft*, vol. 12, no. 5, pp. 471–478, 1975.

[25] W. Tabakoff, "Study of single-stage axial flow compressor performance deterioration," *Wear*, vol. 119, no. 1, pp. 51–61, 1987.

[26] ——, "High-temperature erosion resistance of coatings for use in turbomachinery," *Wear*, vol. 186-187, pp. 224–229, 1995, 8th International Conference on Erosion by Liquid and Solid Impact.

[27] W. Tabakoff and V. Shanov, "Erosion rate testing at high temperature for turbomachinery use," *Surface and Coatings Technology*, vol. 76-77, pp. 75–80, 1995.

[28] W. Tabakoff, "Erosion resistance of superalloys and different coatings exposed to particulate flows at high temperature," *Surface and Coatings Technology*, vol. 120-121, pp. 542–547, 1999.

[29] A. A. Hamed, W. Tabakoff, R. B. Rivir, K. Das, and P. Arora, "Turbine blade surface deterioration by erosion," *Journal of Turbomachinery*, vol. 127, no. 3, pp. 445–452, 2004. [Online]. Available: https://doi.org/10.1115/1.1860376

[30] E. K. Longmire and J. K. Eaton, "Structure of a particle-laden round jet," *Journal of Fluid Mechanics*, vol. 236, pp. 217–257, 1992.

[31] A. Ghenaiet, "Study of sand particle trajectories and erosion into the first compression stage of a turbofan," *Journal of Turbomachinery*, vol. 134, no. 5, 2012.

[32] A. Ghenaiet, S. C. Tan, and R. L. Elder, "Prediction of an axial turbomachine performance degradation due to sand ingestion," *Proceedings of the Institution of Mechanical Engineers, Part A: Journal of Power and Energy*, vol. 219, no. 4, pp. 273–287, 2005.

[33] S. Saxena, G. Jothiprasad, C. Bourassa, and B. Pritchard, "Numerical simulation of particulates in multistage axial compressors," *Journal of Turbomachinery*, vol. 139, no. 3, 2017.

[34] F. Greifzu, C. Kratzsch, T. Forgber, F. Lindner, and R. Schwarze, “Assessment of particle-tracking models for dispersed particle-laden flows implemented in openfoam and ansys fluent,” *Engineering Applications of Computational Fluid Mechanics*, vol. 10, no. 1, pp. 30–43, 2016.

[35] D. Estruch-Samper, “Particle image velocimetry, rj adrian and j. westerweel, cambridge university press, the edinburgh building, shaftesbury road, cambridge, cb2 2ru, uk. 2011. 558pp. 75. isbn 978-0-521-44008-0.” *The Aeronautical Journal*, vol. 116, no. 1176, pp. 219–220, 2012.

[36] R. D. Keane and R. J. Adrian, “Theory of cross-correlation analysis of piv images,” *Applied scientific research*, vol. 49, no. 3, pp. 191–215, 1992.

[37] Z. J. Taylor, R. Gurka, G. A. Kopp, and A. Liberzon, “Long-duration time-resolved piv to study unsteady aerodynamics,” *IEEE Transactions on Instrumentation and Measurement*, vol. 59, no. 12, pp. 3262–3269, 2010.

[38] R. J. Adrian, “Twenty years of particle image velocimetry,” *Experiments in fluids*, vol. 39, no. 2, pp. 159–169, 2005.

[39] D. Carter, R. Hassaini, J. Eshraghi, P. Vlachos, and F. Coletti, “Multi-scale imaging of upward liquid spray in the far-field region,” *International Journal of Multiphase Flow*, vol. 132, p. 103430, 2020.

[40] D. Dabiri and C. Pecora, *Particle tracking velocimetry*. IOP Publishing Bristol, 2020.

[41] L. J. Baker and F. Coletti, “Particle–fluid–wall interaction of inertial spherical particles in a turbulent boundary layer,” *Journal of Fluid Mechanics*, vol. 908, 2021.

[42] D. Schanz, S. Gesemann, and A. Schröder, “Shake-the-box: Lagrangian particle tracking at high particle image densities,” *Experiments in fluids*, vol. 57, no. 5, pp. 1–27, 2016.

[43] M. Ebrahimian, R. S. Sanders, and S. Ghaemi, “Dynamics and wall collision of inertial particles in a solid–liquid turbulent channel flow,” *Journal of Fluid Mechanics*, vol. 881, pp. 872–905, 2019.

[44] G. Papadopoulos, D. Bivolaru, and J. Lin, “Real time gas turbine engine particulate ingestion sensor for particle size and composition,” in *Turbo Expo: Power for Land, Sea, and Air*, vol. 51128. American Society of Mechanical Engineers, 2018, p. V006T05A029.

[45] C. Y. Moon, A. Panda, G. Byun, C. F. Smith, and K. T. Lowe, “Non-intrusive optical measurements of gas turbine engine inlet condensation using machine learning,” vol. 32, no. 4. IOP Publishing, 2021, p. 044001.

[46] C. Y. Moon, C. Edwards, G. Byun, and K. T. Lowe, “Particle characterization using optical measurements and neural networks,” vol. 34, no. 3. IOP Publishing, nov 2022, p. 035202.

[Online]. Available: https://dx.doi.org/10.1088/1361-6501/aca423

[47] D. Baumgardner, H. Jonsson, W. Dawson, D. O'Connor, and R. Newton, "The cloud, aerosol and precipitation spectrometer: a new instrument for cloud investigations," vol. 59. Elsevier, 2001, pp. 251–264.

[48] W. E. Steiner, S. J. Klopsch, W. A. English, B. H. Clowers, and H. H. Hill, "Detection of a chemical warfare agent simulant in various aerosol matrixes by ion mobility time-of-flight mass spectrometry," vol. 77, no. 15. ACS Publications, 2005, pp. 4792–4799.

[49] K. D. Froyd, D. M. Murphy, C. A. Brock, P. Campuzano-Jost, J. E. Dibb, J.-L. Jimenez, A. Kupc, A. M. Middlebrook, G. P. Schill, K. L. Thornhill *et al.*, "A new method to quantify mineral dust and other aerosol species from aircraft platforms using single-particle mass spectrometry," vol. 12, no. 11. Copernicus Publications Göttingen, Germany, 2019, pp. 6209–6239.

[50] P. H. McMurry, "A review of atmospheric aerosol measurements," vol. 34, no. 12-14. Elsevier, 2000, pp. 1959–1999.

[51] S. Sankar, K. Maher, D. Robart, and W. Bachalo, "Rapid characterization of fuel atomizers using an optical patternator," 1999.

[52] A. P. Kulkarni, V. D. Chaudhari, S. R. Bhadange, and D. Deshmukh, "Planar drop-sizing and liquid volume fraction measurements of airblast spray in cross-flow using slipi-based techniques," *International Journal of Heat and Fluid Flow*, vol. 80, p. 108501, 2019.

[53] R. K. Hanson, "Combustion diagnostics: planar imaging techniques," in *Symposium (International) on Combustion*, vol. 21, no. 1. Elsevier, 1988, pp. 1677–1691.

[54] E. Berrocal, E. Kristensson, M. Richter, M. Linne, and M. Aldén, "Application of structured illumination for multiple scattering suppression in planar laser imaging of dense sprays," *Optics express*, vol. 16, no. 22, pp. 17 870–17 881, 2008.

[55] E. Kristensson, E. Berrocal, M. Richter, S.-G. Pettersson, and M. Aldén, "High-speed structured planar laser illumination for contrast improvement of two-phase flow images," *Optics letters*, vol. 33, no. 23, pp. 2752–2754, 2008.

[56] E. Kristensson and G. Kristensson, "Physical explanation of the slipi technique by the large scatterer approximation of the rte," *Journal of Quantitative Spectroscopy and Radiative Transfer*, vol. 189, pp. 112–125, 2017.

[57] A. Gaigalas, L. Wang, and S. Choquette, "Measurement of scattering and absorption cross sections of microspheres for wavelengths between 240 nm and 800 nm," *Journal of Research of the National Institute of Standards and Technology*, vol. 118, p. 1, 2013.

[58] D. D. Evanoff and G. Chumanov, "Size-controlled synthesis of nanoparticles. 2. measure-

ment of extinction, scattering, and absorption cross sections," *The Journal of Physical Chemistry B*, vol. 108, no. 37, pp. 13 957–13 962, 2004.

[59] X. Yu, Y. Shi, T. Wang, and X. Sun, "Dust-concentration measurement based on mie scattering of a laser beam," *PLoS One*, vol. 12, no. 8, p. e0181575, 2017.

[60] G. O. Brown, "Henry darcy's perfection of the pitot tube," in *Henry PG Darcy and Other Pioneers in Hydraulics*, 2003, pp. 14–23.

[61] H. Darcy, "Note relative à quelques modifications à introduire dans le tube de pitot," in *Annales des ponts et chaussées*, vol. 1, 1858, pp. 351–359.

[62] Sanders, "Numerical studies on the intrusive influence of a five-hole pressure probe in a high-speed axial compressor," 2017.

[63] Wilson, "A robust radial traverse temperature probe for application to a gas turbine hp/ip stage," 2012.

[64] T. G. Vincent, "Total temperature probe performance for subsonic flows using mixed fidelity modeling," Thesis, 2019.

[65] A. Shmueli, T. E. Unander, and O. J. Nydal, "Experimental and numerical evaluation and optimization of a non standard pitot/sampling probe," *Engineering*, vol. 5, no. 12, p. 967, 2013.

[66] Yang, "Design and testing of instrumentation for multi-phase flow sampling and local void fraction measurement," 2011.

[67] Lapple, "Calculation of particle trajectories," 1940.

[68] C. N. Davies, *Dust is dangerous*. Faber & Faber, 1954.

[69] H. H. Watson, "Errors due to anisokinetic sampling of aerosols," *Am Ind Hyg Assoc Q*, vol. 15, no. 1, pp. 21–5, 1954. [Online]. Available: https://www.ncbi.nlm.nih.gov/pubmed/13138521

[70] L. Levin, "The intake of aerosol samples," *Izv. Akad. Nauk SSSR Ser. Geofiz*, vol. 7, pp. 914–925, 1957.

[71] Badzioch, "Collection of gas-borne dust particles by means of an aspirated sampling nozzle," 1959.

[72] Davies, "The entry of aerosols into sampling tubes and heads," 1968.

[73] H. Glauberman, "The directional dependence of air samplers," *American Industrial Hygiene Association Journal*, vol. 23, no. 3, pp. 235–239, 1962.

[74] P. Å. TUFTO and K. WILLEKE, "Dependence of particulate sampling efficiency on inlet orientation and flow velocities," *American Industrial Hygiene Association Journal*, vol. 43, no. 6, pp. 436–443, 1982.

[75] J. Vincent, D. Stevens, D. Mark, M. Marshall, and T. Smith, "On the aspiration characteristics of large-diameter, thin-walled aerosol sampling probes at yaw orientations with respect to the wind," *Journal of aerosol science*, vol. 17, no. 2, pp. 211–224, 1986.

[76] S. Badzioch, "Correction for anisokinetic sampling of gasborne dust particles," *J. Inst. Fuel.*, vol. 33, pp. 106–110, 1960.

[77] G. Ruping, "The importance of isokinetic suction in dust flow measurement by means of sampling probes," *Staub-Reinhalt. Luft*, vol. 28, no. 4, pp. 1–11, 1968.

[78] A. Addlesee, "Anisokinetic sampling of aerosols at a slot intake," *Journal of Aerosol Science*, vol. 11, no. 5-6, pp. 483–493, 1980.

[79] C. Zhu, "Dynamic behavior of unsteady turbulent motion in pipe flows of dense gas-solid suspensions," Ph.D. dissertation, University of Illinois at Urbana-Champaign, 1991.

[80] ——, "Isokinetic sampling and cascade samplers," in *Instrumentation for Fluid Particle Flow*. Elsevier, 1999, pp. 9–46.

[81] A. Whiteley and L. Reed, "The effect of probe shape on the accuracy of sampling flue gases for dust content," *J. Inst. Fuel*, vol. 32, p. 316, 1959.

[82] I. Davis, "Sampling probes for duct and stack sampling in: Acgih, editor," *Air sampling instruments for evaluation of atmospheric contaminants. 4th ed. Cincinnati, Ohio*, pp. L11–L13, 1972.

[83] N. Fuchs, "Sampling of aerosols," *Atmospheric Environment (1967)*, vol. 9, no. 8, pp. 697–707, 1975.

[84] E. B. Sansone and P. M. Giever, "Sampling airborne solids in a duct following a 90° bend," *Journal of the Air Pollution Control Association*, vol. 17, no. 9, pp. 605–606, 1967.

[85] S. L. Soo, *Instrumentation for fluid particle flow*. Univ. Press of Mississippi, 2013.

[86] K. Ito, S. Kobayashi, and M. Tokuda, "Mixing characteristics of a submerged jet measured using an isokinetic sampling probe," *Metallurgical Transactions B*, vol. 22, no. 4, pp. 439–445, 1991.

[87] R. Boothroyd, "An anemometric isokinetic sampling probe for aerosols," *Journal of Scientific Instruments*, vol. 44, no. 4, p. 249, 1967.

[88] S. L. Soo, J. J. Stukel, and J. M. Hughes, "Measurement of mass flow and density of aerosols in transport," *Environmental Science & Technology*, vol. 3, no. 4, pp. 386–393, 1969.

[89] W. C. Hinds, "Aerosol technology: Properties, behavior, and measurement of airborne particles(book)," *New York, Wiley-Interscience, 1982. 442 p*, 1982.

[90] W. Hemeon and G. F. Haines Jr, "The magnitude of errors in stack dust sampling," *Air repair*, vol. 4, no. 3, pp. 159–164, 1954.

[91] L. Belyaev, "Techniques for collection of representative aerosol samples," 1973.

[92] ——, "Investigation of aerosol aspiration by photographing particle tracks under flash illumination," 1971.

[93] T. Allen, "Microscopy," in *Particle Size Measurement*. Springer, 1990, pp. 217–248.

[94] K. May, "17th symposium of the society for general microbiology, imperial college," 1967.

[95] J. H. Vincent, *Aerosol sampling: science, standards, instrumentation and applications*. John Wiley & Sons, 2007.

[96] A. R. McFarland, C. A. Ortiz, M. E. Moore, R. E. DeOtte Jr, and S. Somasundaram, "A shrouded aerosol sampling probe," *Environmental science & technology*, vol. 23, no. 12, pp. 1487–1492, 1989.

[97] S. Chandra and A. R. McFarland, "Shrouded probe performance: Variable flow operation and effect of free stream turbulence," *Aerosol Science and Technology*, vol. 26, no. 2, pp. 111–126, 1997.

[98] C. H. Twohy, "Model calculations and wind tunnel testing of an isokinetic shroud for high-speed sampling," *Aerosol Science and Technology*, vol. 29, no. 4, pp. 261–280, 1998.

[99] N.-G. Heo, S.-H. Woo, J.-H. Lim, S.-J. Yook, and K.-H. Ahn, "Investigation of a double shrouded probe for particle sampling in high velocity airflows," *Advanced Powder Technology*, vol. 29, no. 5, pp. 1085–1091, 2018.

[100] N.-G. Heo, J.-H. Lim, J.-W. Lee, J.-S. Lee, S.-J. Yook, and K.-H. Ahn, "Development of a sampling probe for representative sampling of pm at freestream velocities in the range from 0 to 300 km h1," *Journal of Atmospheric and Oceanic Technology*, vol. 35, no. 4, pp. 727–738, 2018.

[101] C. Briones, Bichal, "Aspiration efficiencies of a soot-particulate sampling probe with dilution under gas turbine conditions," *AIAA*, 2008.

3. Analysis of C-spec particle breakage in a turbine engine particle ingestion test cell

The contents of this chapter have been accepted to be published in the 2023 proceedings of the American Society of Mechanical Engineers Turbomachinery Technical Conference and Exposition (Vlach, T, **Olshefski, K**, Bunin, D, Ehlers, A, Caddick, M, Lowe, T, & Ng W. "Analysis of C-Spec Particle Breakage in a Turbine Engine Particle Ingestion Test Cell." Proceedings of the ASME Turbo Expo 2023: Turbomachinery Technical Conference and Exposition. Boston, Massachusetts, USA. June 26–30, 2023.)

The author's Original/Preprint version of the accepted manuscript has been included. This manuscript is forthcoming and will be published as open access in August 2023. As second author, the dissertation author contributed significantly to the realization of the manuscript. Particularly, the author was instrumental in the design and implementation of the test cell being described herein. The scope of contribution encompassed various aspects of the project, such as conceptualizing the design, providing detailed component specifications, overseeing the manufacturing and assembly processes, and establishing the layout of the facility. The dissertation author was also responsible for developing the test stand power absorption system, fuel system, and oil recirculation system. The detailed schemes for particle capturing and visualization, which are described in sections 3.4.2 and 3.4.3, have been elaborated upon in Chapters 5 and 4. These chapters provide a comprehensive analysis of the schemes and their associated methodologies, presenting new insights and perspectives to the research community. The described schemes represent primary contributions to the dissertation, reflecting the author's expertise and original contributions in the field. In addition to these tasks, the present author made significant contributions to the manuscript, writing and editing substantial portions of it. The meticulous attention to detail and comprehensive approach ensured that the project was completed successfully and met all necessary requirements.

Abstract

A turboshaft engine test rig based on a Rolls-Royce M250-C20B engine has been developed at Virginia Tech's Advanced Propulsion and Power Laboratory in cooperation with its government and industry partners. The engine has been instrumented to allow measurement of the effects that dust particles have on the engine (power degradation) as well as the effects that the engine has on the particles (e.g., breakage). The work in this paper presents the first set of data collected from the engine tests and focuses on changes in the shape and size of C-Spec (quartz) dust after passage through the first five stages of the compressor and through the entire engine. Dust samples have been analyzed to determine particle size and shape distributions at the locations of interest and these have been compared with undigested material. These preliminary analyses suggest that average particle volume decreased to $\sim$5% of the original size during transit through five stages of the axial compressor. No subsequent change in size and shape occurred, despite these particles then passing through one additional axial stage, the centrifugal stage, and four stages of the turbine section. Moreover, the apparent sphericity of the particles increased slightly in the axial compressor, hinting at the reduction of their erosion potential. The data presented here will assist communities interested in turbine engine environmental damage in understanding the deterioration processes and their prevention. Ultimately, the research will allow for pinpointing such degradation effects to a single compressor stage, resulting in a greater ability to predict engine damage and prevent subsequent loss of human life.

3.1 Introduction

Particulate ingestion in jet engines presents a serious hazard to the operation of civilian and military aircraft. Although the mechanisms of damage in the civilian and military worlds differ, the ultimate result in both cases ranges anywhere from the high maintenance cost of damaged engine parts and reduced combat readiness to the possibility of serious injuries or the loss of human life. While civilian aircraft fleets are generally prone to ingestion of high-atmospheric particles, such as volcanic ash [1, 2], military aircraft are usually damaged by dust and sand particles when flying near the ground [3]. It is obvious that helicopters and vertical take-off and landing aircraft operating in desert environments are at the greatest risk. One way to reduce the possibility of engine damage from particle ingestion is to minimize the ingestion of such particles by employing engine air particle separators. Such devices have been used on military helicopters since their wide-ranging deployment in the Vietnam War and were thoroughly tested during the Gulf War, which marked the first large-scale combat operations in sandy environments. Although proven effective when installed in helicopters [4], air particle separators struggle to protect modern vertical take-off and landing aircraft, such as the M-22 Osprey. Multiple M-22 aircraft have been involved in severe accidents that have resulted in more than 50 deaths [5]. Although not all crashes occurred as a result of particle-induced engine damage, the US military recognizes its danger and is developing suitable particle separators, all of which have been found to be ineffective, as described in the Department of Defense Inspector General report *Evaluation of the V-22 Engine Air Particle Separator* [6]. An example of an M-22 Osprey aircraft operating in a harsh desert environment is shown in Fig. 3.1.

Figure 3.1: A USMC V-22 Osprey in a Sand Cloud [7]

In response to concerns about particulate ingestion, the Office of Naval Research continuously sponsors research activities with the objective of fully documenting the cases of particle-engine interaction. The Virginia Tech particle ingestion test cell, which was funded by the Office of Naval Research and built in partnership with Rolls-Royce North America, incorporates a Rolls-Royce M250-C20B turboshaft engine. The engine will be used to study the effect of particle ingestion on compressor characteristics and whole engine performance, and to study behavior such as particle breakage in the compressor. The sand loading campaign will be carried out in incremental steps that will allow for a precise measurement of engine deterioration. The overall engine performance will be evaluated using engine performance parameters including pressures, temperatures, and torque, while 3D scanning of the compressor will be utilized to localize and quantify the damage to the individual compressor stages.

Providing the information collected during the engine test campaign to those communities focused on quantifying and modeling particle-ingestion-induced engine damage will permit the comparison of computation results with real-world test data. Although big-picture predictive engine damage models can be obtained by collecting data from large fleets, computational fluid dynamics models that would allow for precise identification of particle-laden flows in jet engine components currently lack data that could be used for their validation. Therefore, the experiments that will be performed in the Virginia Tech particle ingestion test cell will provide researchers with fully documented particle-laden flows that can be used to fine-tune and validate their work and improve the accuracy of models used for particle-laden flow modeling.

This work is intended to introduce the sand ingestion test cell, its capabilities, and its first results to a professional audience. The first section of this paper describes the test cell itself and provides a brief overview of the technical background. The second section shows examples of the test cell's capabilities, ranging from compressor tip clearance measurement to whole engine performance measurement. In the third section, preliminary data collected during the shakedown test campaign are presented and discussed.

3.2 History of Full-scale Engine Particle Ingestion Testing

The occurrences of gas turbine engine flameouts and failures have led to an increase in studies of debris ingestion on full-scale engines, such as accelerated erosion and deposition testing. Because erosion and deposition mechanisms are common with debris ingestion, full-scale testing can be used to improve the resilience of propulsion engines. The earliest full-scale engine studies known to the authors were conducted in 1987 using a TF33 turbofan and J75 turbojet engine. The engines were tested in dust-laden operating conditions to evaluate engine performance [8–10].

In 1998, Motoren-und Turbinen-Union München GmbH (MTU) investigated the effects of a particulate filtration system on an MTR390 turboshaft engine to quantify performance degradation and related component erosion [11]. Two test cases were designed to provide the manufacturer with confirmation that their engine met specifications related to operation in sandy environments.

In 2018, various full-engine tests investigating the interaction between 11 different turbine blade coatings and Air Force Research Laboratory-developed "average sand" found there is a severe lack of understanding of the underlying physio-chemistry involved with particle coating interactions [12]. This testing was a collaborative study between the U.S. Army Research Laboratory, Naval Air Systems Command (NAVAIR), NASA Glenn Research Center, and U.S. Army Aviation and Missile Research Development and Engineering Center (AMRDEC). The study found the presence of calcium-magnesium-alumino-silicate (CMAS) infiltration and adherence on both the surface and subsurface (inside the cooling channels) of the airfoil.

In addition to the above publications in the open literature, there were other proprietary engine tests with particle ingestion that were conducted by various engine manufacturers but not published due to their sensitive nature. With the lack of data provided in the open literature, the project, and its activities provide a great opportunity to enhance the understanding of full-scale particle-engine interaction.

3.3 Test Cell Introduction

The test cell is located at Virginia Tech's Advanced Propulsion and Power Laboratory, Blacksburg, Virginia, and is a culmination of research focused on sand ingestion conducted over the course of several years. In this section, the test cell and its subsystems are introduced. The overall design of the test cell is focused on the ability to ingest sand particles into the engine and evaluate their effects on its performance and the effect the particle-engine hardware interaction has on the particles themselves. This will allow for the generation of data useful for evaluating mathematical models of particle interaction inside an actual turbine engine. The engine and the test cell can also serve as a test bed for the evaluation of various instrumentation related to sand ingestion research ranging from conventional probes to state-of-the-art laser-based instrumentation.

3.3.1 Rolls-Royce M250-C20B

The heart of the sand ingestion test cell is a Rolls-Royce M250-C20B turboshaft engine. The Rolls-Royce M250-C20B is a member of originally Allison Engine Company's, now Roll-Royce's, family of small turboshaft engines. The maximum power output of the engine is $420\,\mathrm{SHP}$. The engine core consists of a two-stage high-pressure turbine stage driving a six-stage axial compressor followed by a single-stage centrifugal compressor providing a pressure ratio of 7.1. The power output is through a two-stage low-pressure turbine driving a Kahn water brake dynamometer. The engine relies on a hydro-mechanical control unit that interfaces with an in-house developed engine and facility control system. The engine installation in the test cell without a sand delivery apparatus at the engine inlet is shown in Fig. 3.2.

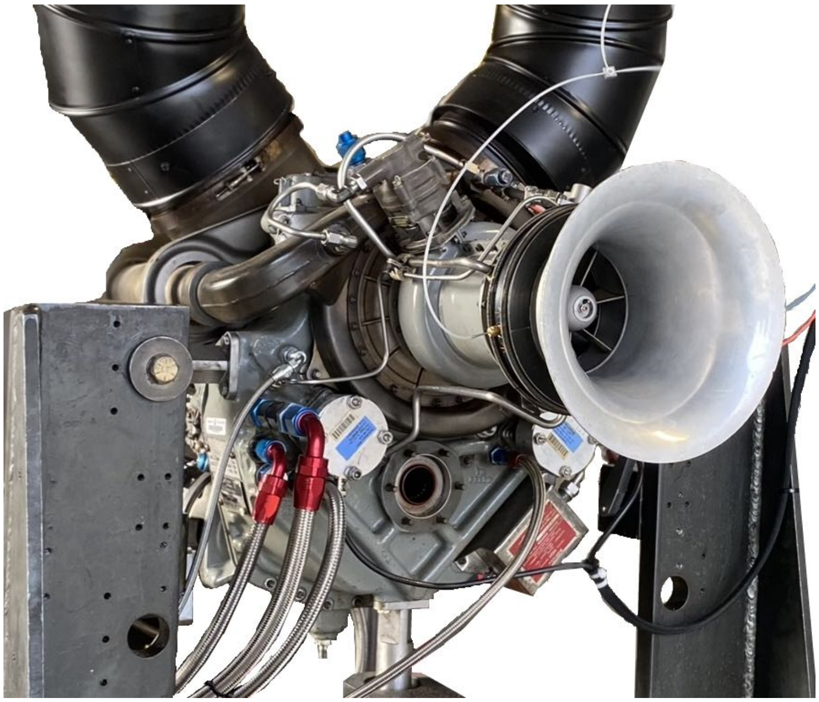

Figure 3.2: Rolls-Royce M250-C20B installed in the Test Cell, without sand delivery system

3.3.2 Facility and Engine Control System

The control system that ensures a reliable and safe operation of the engine and the test cell was designed and built in-house and is powered by two National Instruments compactRIO industrial real-time controllers. The controllers are capable of control loop execution and data acquisition with the rate exceeding $1\,\mathrm{kHz}$. This ensures that the system can monitor and adequately react to all engine conditions, including engine overspeed events that can have catastrophic consequences if not detected and reacted to in their early stages.

The operation of the engine requires two operators, one is responsible for controlling the engine and the dynamometer itself, and the second operator is responsible for the data acquisition. This ensures that both operators can focus on their individual objectives – the safe operation of the engine and the collection of the test data, respectively. The information and control elements are shown to the operators on high-resolution displays, a central emergency push-button console is located between the operators, and a throttle quadrant with control elements for the engine throttle, power output shaft speed governor, and dynamometer load is available to the engine operator.

The control system is programmed with automated sequences, such as start-up and flight idle cross-over maneuvers, that greatly reduce the workload and potential human error of the operators.

Moreover, specific mission profiles can be programmed within the control system and executed without the need for the operator's input.

3.3.3 Dynamometer & Engine Subsystems

The test cell is equipped with all the subsystems vital to the operation of the engine. This includes the water system, oil system, ignition system, and dynamometer. All the subsystems have been designed with scalability in mind and therefore are capable of accommodating various types of engines should the need to arise in the future of the test cell.

The water system consists of a cold-water tank, water pumps, control valves, an intermediate water tank, and an oil-water heat exchanger. The purpose of the water system is to provide a steady water supply to the dynamometer and oil cooling. Without the addition of a cooling tower, the water system provides cool water to the system for several hours of engine runtime at maximum power conditions.

The oil system of the engine utilizes a dry sump system, therefore an external portion of the oil system had to be developed consisting of an oil tank, heat exchanger, and oil pressure instrumentation including a torquemeter pressure transducer.

The ignition system consists of a pair of batteries providing power to the starter and the ignition exciter. The system is controlled via the facility control system and therefore is automated within the engine control sequences. Ample battery capacity is available to allow for a sufficient number of engine starts and dry-motoring periods of a typical test campaign, including reserve for emergency engine motoring.

The power output of the engine is converted into heat in a high-speed Kahn water brake dynamometer. The dynamometer is controlled either in manual mode via a control console or automatically by the engine control system. Just like the other facility systems, the dynamometer has been designed with scalability in mind and supports engines with power outputs of up to $1000\,\mathrm{SHP}$.

3.3.4 Instrumentation

The engine and the test cell are instrumented to allow for full performance evaluation of the engine corresponding to the standard measurement practices of engine manufacturers and the needs of the specific particle ingestion research objectives.

The standard engine instrumentation used for engine performance evaluation consists of the

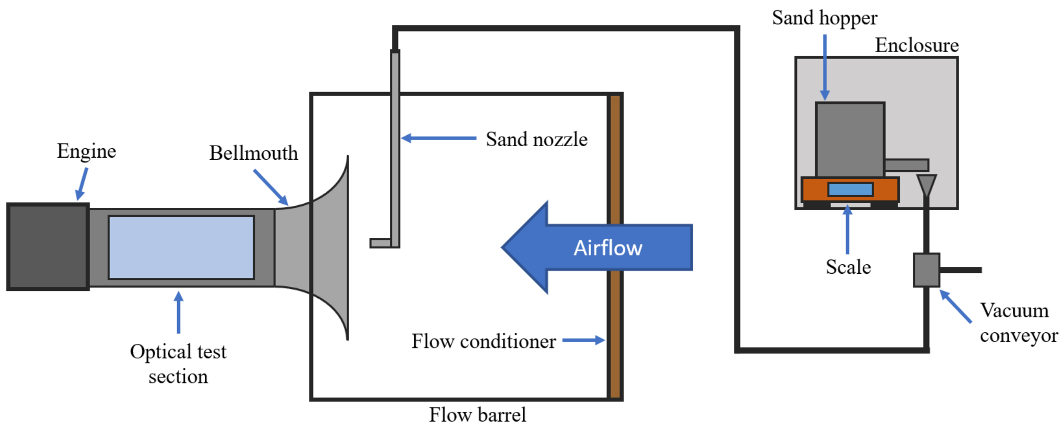

Figure 3.3: Sand Delivery System

following: inlet total temperature and pressure combined with bellmouth static pressure (mass flow measurement), engine core speed (N_1), output shaft speed (N_2), torque, insterstage turbine temperature, and fuel mass flow rate. Moreover, static pressure taps are located at each of the compressor's stages allowing for detailed performance mapping of the compressor. In addition to the engine instrumentation, the test cell contains instrumentation to ensure the safe operation of the subsystem such as oil pressures and temperatures, dynamometer water temperatures, and such.

In addition to conventional instrumentation, the test cell has been designed to allow for the use and validation of unconventional instrumentation. This includes access ports on the engine allowing for sampling particles from the engine's primary flow path or optical access for laser-based instrumentation inside both the engine and the inlet system.

3.3.5 Sand Delivery System

A sand delivery system capable of delivering sand loading to the engine with high levels of steadiness and uniformity is a crucial part of the research. The sand delivery system designed at Virginia Tech and utilized in the particle ingestion research consists of four main elements – a sand hopper mounted to a scale inside an enclosure, tubing with a vacuum conveyor, a delivery nozzle, and a flow barrel with a flow conditioner. The overall schematic of the system is shown in Fig. 3.3.

Sand particles begin their journey to the engine in a hopper that utilizes a helical element to deliver a calibrated amount of material to the delivery system in a given duration. The rate of particle delivery can be adjusted using a controller located in the control room. While the delivery rate has been calibrated prior to the test campaign, the sand hopper is mounted to a precise scale that can be read remotely and provide information about both the rate and amount of particles entering the delivery system. To ensure that the particles entering the system reach the delivery nozzle, a vacuum conveyor is utilized in the particle delivery system close to the sand hopper.

The sand particles are injected into the airflow upstream of the bellmouth by using a delivery nozzle located inside the flow conditioning barrel. In the current setup of the test cell, a single nozzle located at the centerline is used to deliver the particles into the engine. Downstream of the calibrated bellmouth, an optical test section is mounted that serves as an extension of the engine inlet to allow for optical (laser and camera) access to the particle-laden flow entering the engine.

The sand delivery system is compatible with various particle types and sizes such as C-Spec (quartz) and Arizona or ISO Test Dusts based on the current research needs. For certain test dust types, the sand delivery enclosure can be purged with dry air to prevent particle clumping and ensure reliable delivery.

3.4 Research Capabilities

As has been discussed in the previous sections, the design of the entire test cell was made with various particle ingestion research capabilities in mind. In the following subsections, some specific capabilities of the test cell that will improve the understanding of particulate ingestion engine damage are presented.

3.4.1 Compressor Damage Evaluation

The Rolls-Royce M250-C20B engine offers easy access to the six stages of its axial compressor. This makes it an ideal engine for research focused on particle-engine hardware interaction. The compressor casing can be opened within a few hours by using tools commonly found in mechanical shops. If done properly, accessing the axial compressor does not take a toll on the engine's safe operation upon reassembly. The Virginia Tech test cell is capable of performing the following on the axial compressor hardware:

Tip Clearance Measurement

Due to the ease of access to the rotor stages, a tip clearance measurement can be performed after every sand-loading campaign to assess the damage done to the compressor case coating. This allows for linking the decrease in the performance of the engine to the effects of increased

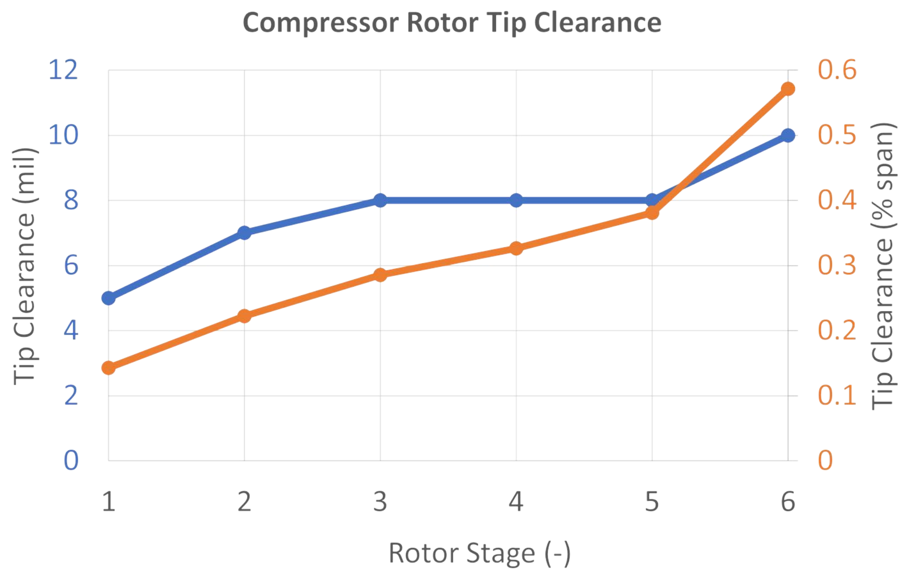

Figure 3.4: Example Tip Clearance Measurement

tip clearance due to the excessive abrasion of the compressor case coating. An example of a tip clearance measurement taken inside the engine is shown in Fig. 3.4.

Compressor 3D Scan

Together with its industry partners, the research performed at Virginia Tech is capable of producing highly detailed 3D scans of the compressor geometry. The damage to the compressor hardware is captured with µm accuracy, providing a detailed insight into the damage mechanisms. The scanned geometries can also be used in numerical models to accurately model/validate the particle-solid interaction. The compressor must be disassembled in order to perform a 3D scan, so this is ideally performed only at targeted intervals.

Image-Based Damage Assessment

To avoid the need for compressor disassembly, an image-based compressor damage assessment can be performed at any stage of sand loading campaigns. The test cell is equipped with a high-resolution macro camera capable of documenting the damage of the first axial stage and with a borescope extension of all the axial compressor stages. The images can be processed in specialized software to obtain the evolution of the particle-induced damage. An example is shown in Fig. 3.5 documenting the damage to the first axial rotor stage leading edge.

3.4.2 In-Situ Particle Sampling

In order to assess the change in dust particle properties such as size and shape, a particle sampling instrument has been developed which allows for particle collection from the primary flow path [13]. Ongoing investigations are focused on sampling particles from the following locations: upstream of the engine inlet (Fig. 7.1), downstream of the first axial stage rotor, and in the centrifugal compressor discharge tubes. The instrumentation consists of a sample probe, a collection apparatus, and a vacuum system aiding the particle collection in low-pressure areas of the engine. The collected samples can then be analyzed using a variety of microscopy techniques. This will eventually provide valuable information on the behavior of particles when impacting high-speed machinery and serves as a dataset for the validation and tuning of numerical particle impact models.

Initial development of the sampling probe described above has focused specifically on the sampling of ultra-Stokesian particles. That is, particles whose momentum is sufficiently large to ensure that their trajectory is not altered by the presence of the sampling probe within the flow. For the material of interest, C-Spec quartz (MIL-E-5007C), this includes all but an insignificant

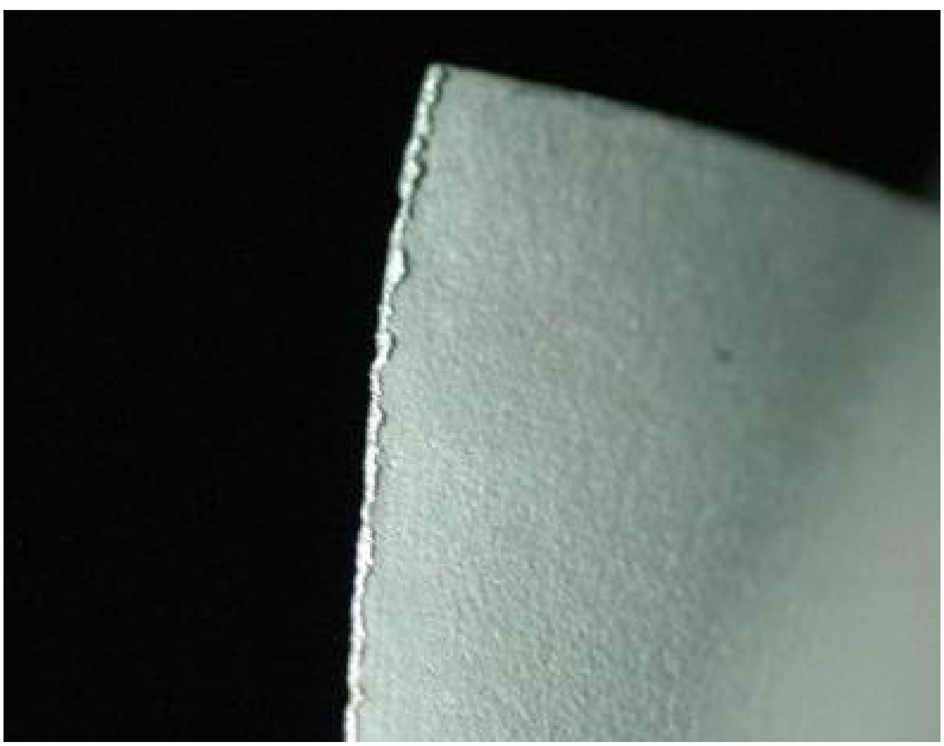

Figure 3.5: Detail of First Axial Stage Leading Edge Erosion

quantity of the overall sample. Therefore, sampling bias has not been considered a major source of uncertainty in current work. However, depending on the size distribution of particles to be sampled in the future, this may require further consideration. Future investigations will work to minimize this bias and extend the application to other materials, such as ISO 12103-4 A4, Arizona Road Dust.

The sampled particles can be analyzed directly in a particle analyzer, or 'offline' using electron beam or X-Ray methods utilizing infrastructure in Virginia Tech's Department of Geosciences. An example using electron beam microscopy is given below. If detailed particle shape is needed, 3D scans of individual particles are relatively straightforward to obtain.

3.4.3 Instrumentation Development Capabilities

The test cell is an invaluable resource for researchers who are establishing novel instrumentation and measurement capabilities. It offers a cost-efficient opportunity to install this equipment on the engine, inlet, or exhaust during the development stage and test through equipment maturity. Therefore, the test cell is not only capable of particle ingestion research, but is a powerful platform for testing turbine engine instrumentation without the need to invest in the runtime of large turbine engines.

Figure 3.6: Particle Sampling Probe Upstream of the Engine Inlet

One example of an ongoing project which has utilized this testing platform is the Virginia Tech Particle Visualization by Illuminated Scattering (ParVIS) technique. This method uses only a simple light source and imaging camera to provide users with a qualitative snapshot of inlet particle distribution as well as particle mass flow and number density estimates at operationally relevant conditions. The method functions by first projecting a one-inch-wide laser sheet from top (twelve o'clock) to bottom (six o'clock) at the inlet plane of a gas turbine engine. Next, images are continuously captured and saved for analysis. Image post-processing relates the scattering intensity of solid particles to the mass flow through the engine. For these tests, sand was delivered at a maximum rate of approximately $1.5\,\mathrm{g\,min^{-1}}$. Parameters are reported on a time-averaged basis as well as a time-resolved basis to the frame rate at which successive images are captured. Therefore, this technique allows investigators to gain a broad perspective of particle behavior at the engine inlet while also allowing users to resolve particle flow unsteadiness. Figure 6.4 shows ParVIS output quantities whereby accumulated particles have been imaged over a one-minute period. Figure 6.4-A shows the grayscale composite image of all pixels passing through the laser sheet over the one-minute timeframe. In Fig. 6.4-B, a Gaussian smoothing filter was applied for ease of interpretation, and volumetric flow information from the M250-C20B engine was utilized to estimate local particle concentration throughout the region of interest. Initial results show accurate estimations of injected particle mass flow, with a sand mass flow root-mean-square error of $0.20\,\mathrm{g\,min^{-1}}$ as compared to the monitored mass flow value using a precision scale. Additional details are reported in [14]. This technique highlights the utility of the test cell for engine instrumentation development and leads the effort in the advancement of diagnostic tools for engines operating under harsh conditions.

3.5 Shakedown Test Campaign Results

The test cell was subjected to multiple phases of the shakedown test campaign since April 2022 to validate and ensure the safe operation of the engine and all its subsystems. In the following sections, the conditions of the test campaign will be discussed and the results of the analysis of sand particles collected at various engine stations will be presented.

3.5.1 Test Conditions

For the shakedown test campaign with the sand delivery system, the engine was run at ground idle conditions in order to preserve its life. A total of $75\,\mathrm{minutes}$ of run time with sand ingestion

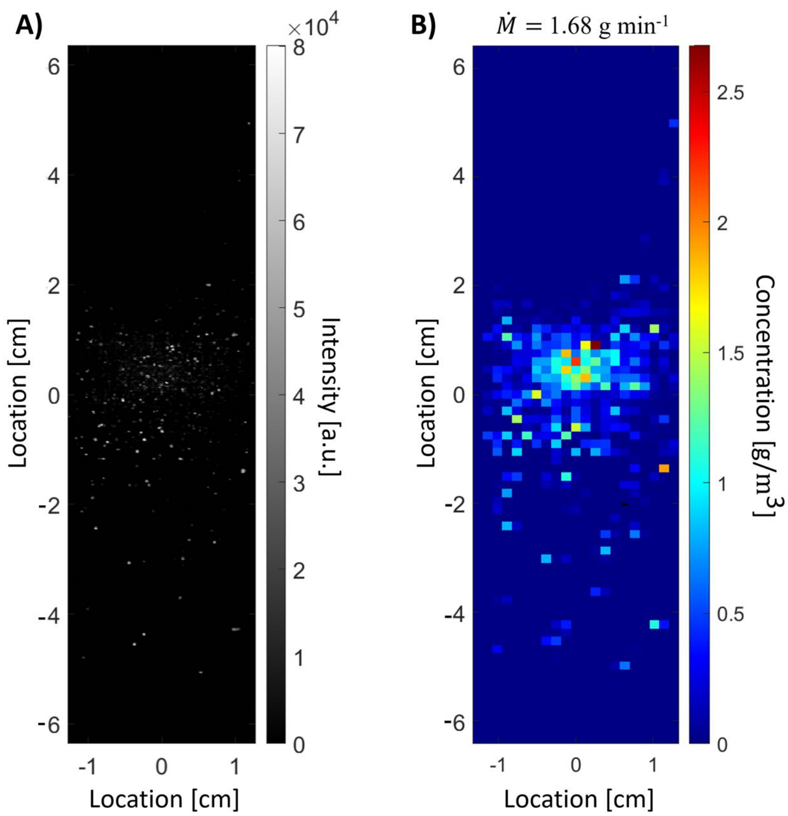

Figure 3.7: ParVis: Instantaneous Particle Capture (A), Particle Concentration Quantities Calculated Using Engine Flow Rate (B)

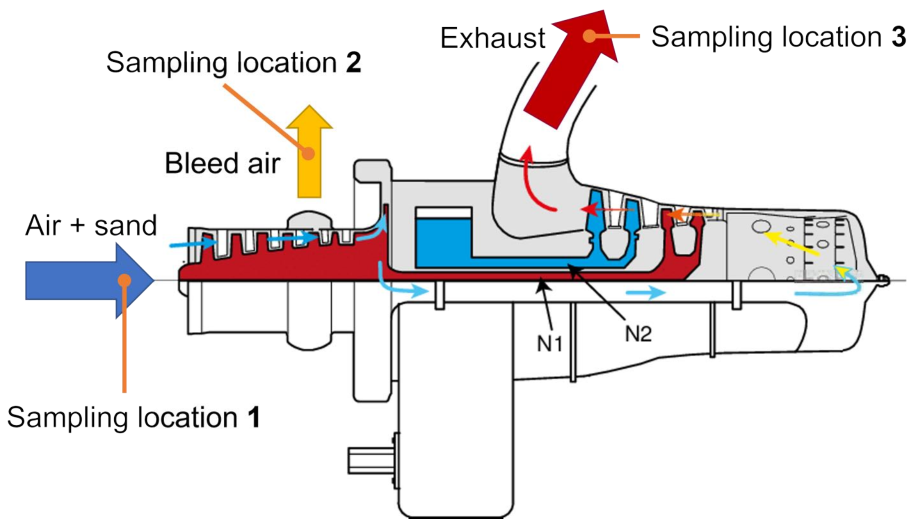

Figure 3.8: Particle sampling locations

was accumulated. The sand used for this test campaign was crushed quartz, commonly referred to as C-Spec (MIL-E-5007C). Its concentration in the air entering the engine was $22\,\mathrm{mg\,m^{-3}}$ and $45\,\mathrm{mg\,m^{-3}}$, with a total of $100\,\mathrm{g}$ of C-Spec ingested.

3.5.2 Particle Collection

In order to determine whether and how the test engine damaged input C-Spec particles, samples of dust processed by the engine were taken from two localities, comparing them to an aliquot of uningested dust (Fig. 3.8). This 'initial C-Spec' (Fig. 3.8-**1**) sample was taken from the same batch used for the ground-idle test run. Horizontal surfaces on and around the test stand were cleaned before the test, with any particle buildup detected after the test assumed to represent material processed by the engine at that time. Several surfaces near and underneath the exhaust duct (Fig. 3.8-**3**) were sampled, where substantial material had been deposited. A second set of samples (Fig. 3.8-**2**) was taken from surfaces near the compressor bleed, which vents gas following the fifth compressor stage. In each case, samples were carefully collected by brushing dust onto clean paper sheets and then pouring this into $5\,\mathrm{ml}$ vials.

Representative samples were chosen for detailed analysis and are hereafter referred to as 'C-Spec' (for the uningested dust), 'CBS (the compressor bleed sample), and 'ES' (the exhaust sample). Optically, these three groups were different, with C-Spec exhibiting a characteristic white color (consistent with its quartz-dominated composition) and the exhaust sample containing darker gray particles (presumably a soot coating). The compressor bleed sample was pale but notably

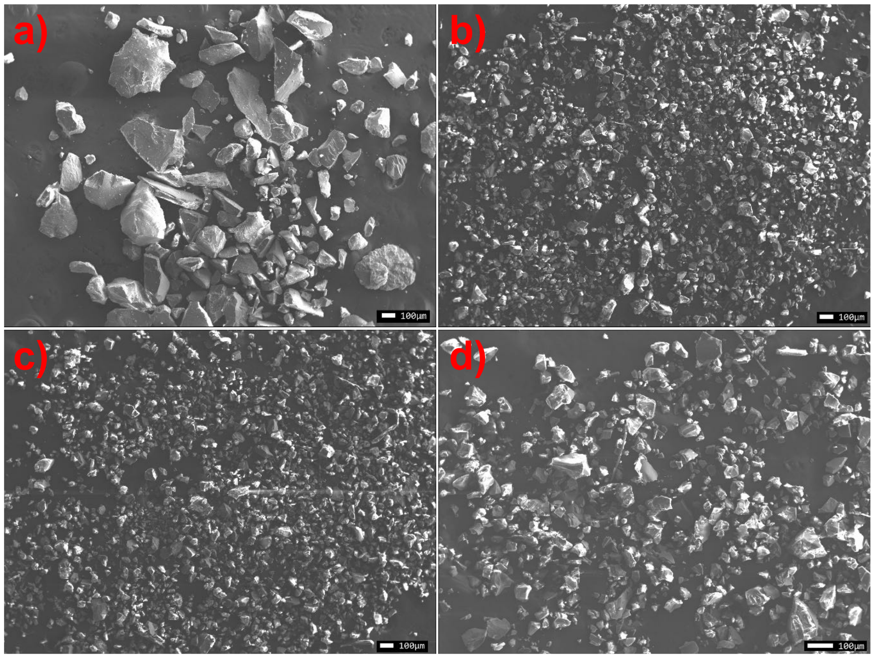

Figure 3.9: Electron microprobe images of: a) C-Spec particles prior to engine testing; b) compressor bleed dust sample; c) exhaust sample; d) compressor bleed dust sample at a higher resolution. Note that images a-c are at the same scale.

darker than the input C-Spec, likely caused by discoloration from the compressor coating material.

3.5.3 Particle Analysis

Preliminary sample analysis involved polarizing light microscopy and photography, with all optical properties (including birefringence) suggesting that particles from all samples still constitute relatively pure, unreacted quartz. There was no indication of amorphous glass, confirming expectations that no melting occurred due to the low combustion temperatures of the M250-C20B engine. Further analysis used a field emission electron microprobe to obtain high-resolution images of each sample (e.g., Fig. 3.9) and to capture energy-dispersive-spectra for select points. These spectra revealed only silicon and oxygen for most of the analyzed material, again confirming a lack of reaction and minimal contamination. Optical and electron beam images of the samples were subsequently processed using the National Institutes of Health's ImageJ software to obtain size and shape properties. Following image calibration, particles were manually measured and outlined to reduce potential uncertainties introduced by automated particle detection algorithms.

The apparent lengths (in 2D) of 173 particles from C-Spec, 500 from the CBS, and 500 par-

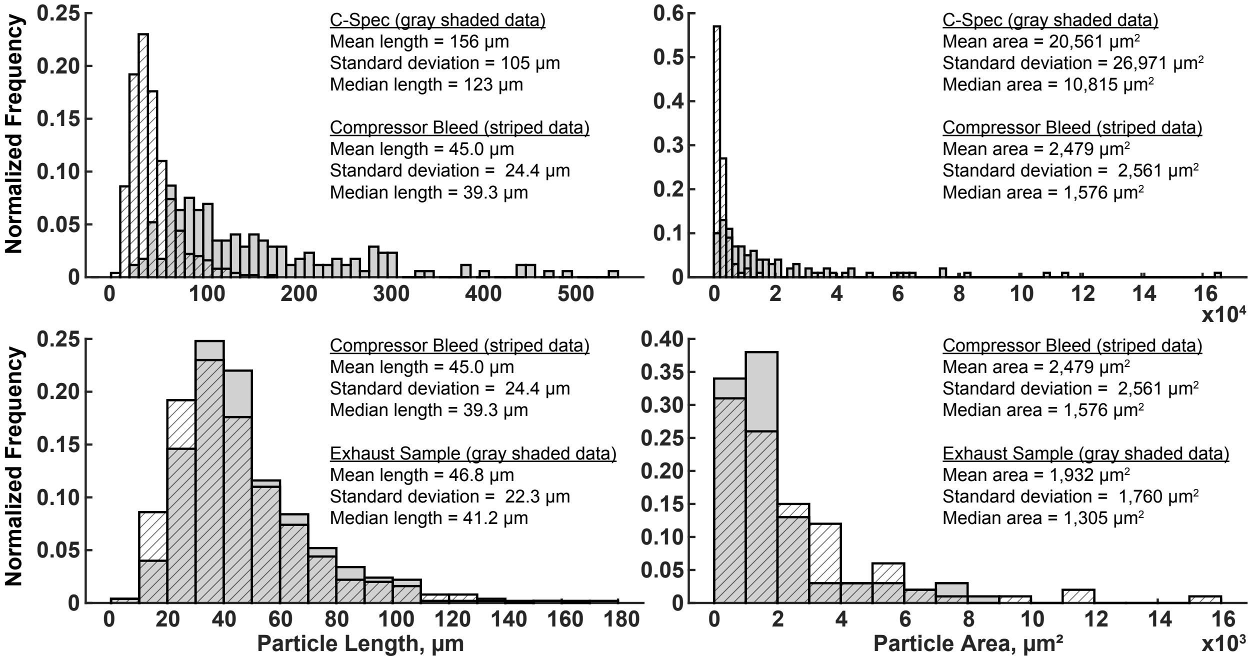

Figure 3.10: Particle lengths (left panels) and areas (right) in C-Spec (top panels, gray shaded), CBS (top and bottom, striped) and ES (bottom panels, gray shaded).

ticles from the ES were analyzed. Results show that the CBS particles are substantially smaller than C-Spec, reducing from a mean grain size of 156 to $45\,\mu\text{m}$. The ES, however, is effectively identical to the CBS, with a mean grain size of $46\,\mu\text{m}$. The distribution of grain sizes is also similar between the CBS and ES, differing dramatically from C-Spec (Fig. 3.10). Analyzed particles in the unaltered C-Spec range from 23 to $547\,\mu\text{m}$, with a standard deviation about the mean of $105\,\mu\text{m}$. In contrast, the range of particle lengths in the CBS is 8.6–$174\,\mu\text{m}$, with a standard deviation of $24\,\mu\text{m}$. These values are similar in the ES (7.1–$161\,\mu\text{m}$ range, with a standard deviation of $22\,\mu\text{m}$). Taken together, these data (Fig. 3.10) show that the processed dusts are approximately three times smaller than C-Spec and have narrower particle size distributions.

Additional shape characteristics were defined for 100 particles each from C-Spec, the CBS, and the ES. Circularity, aspect ratio, and area were analyzed. Here, circularity is defined as $4\pi A/p^2$, where A is particle area, and p is particle perimeter.

As anticipated from the length measurements, the areas of CBS and ES particles were similar, with each approximately one order of magnitude smaller than C-Spec particles (Fig. 3.10). This grain size reduction coincides with a minor decrease in the aspect ratio of the CBS and ES particles relative to C-Spec (Fig. 3.11). Here, aspect ratio is defined as the length of the major axis of the

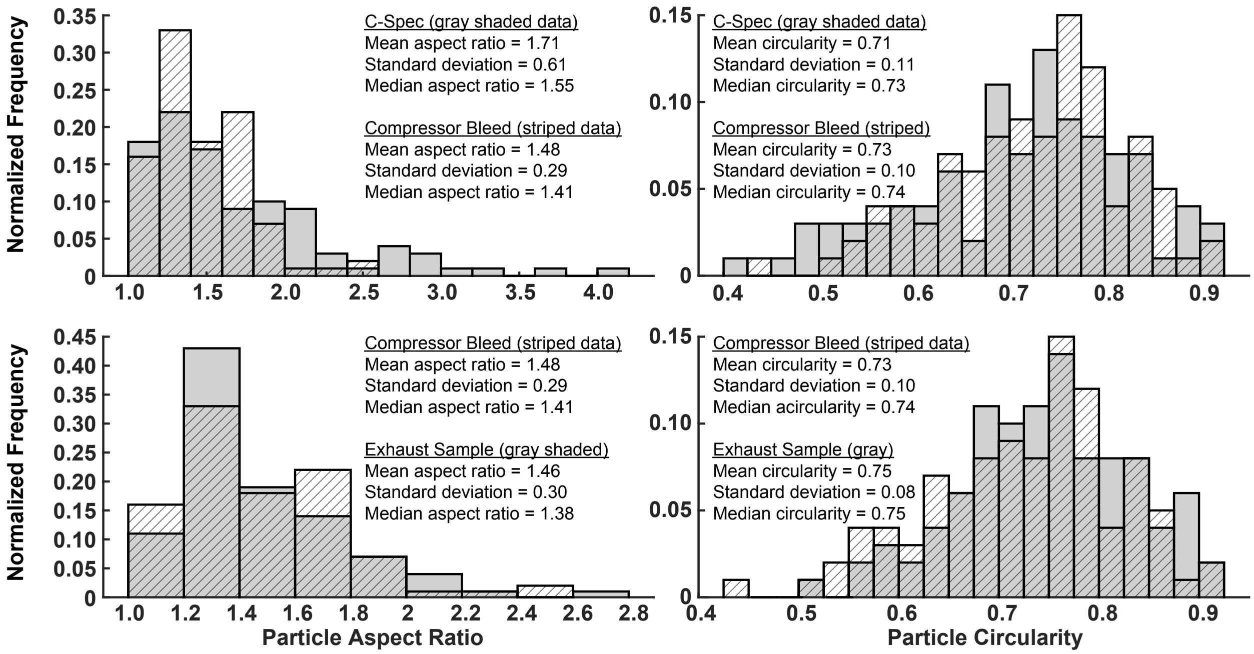

Figure 3.11: Particle aspect ratios (left panels) and circularities (right) in C-Spec (top panels, gray shaded), CBS (top and bottom, striped) and ES (bottom panels, gray shaded).

particle divided by the length of the minor axis, where both axes were automatically detected by ImageJ following manual tracing of the particle outline. The mean aspect ratio of C-Spec was 1.71, with the aspect ratios of CBS and ES particles averaging 1.48 and 1.46, respectively. C-Spec contained a subset of elongate particles with aspect ratios of 2.5–4.5 that are absent from the engine-processed samples.

Despite these clear trends in the reduction of particle lengths, areas, and aspect ratios from C-Spec to CBS and ES, there is a weaker difference in the circularity of particles between these samples. This metric, which compares the perimeter of a grain to that of a circle of equivalent area, tends to 1 for circular grains and averaged 0.71 for C-Spec, 0.73 for CBS particles, and 0.75 for ES particles (Fig. 3.11).

Taken as a whole, these data suggest significant particle breakage in the compressor stack at ground idle, resulting in a reduction in the size of C-Spec quartz grains to approximately one-third of their original length and one-tenth of their original area. We assume that these trends scale well in the third dimension, in which case the average particle volume after five compressor stages will be approximately $4\,\%$ that of input C-Spec particles. This breakage tends to reduce average particle aspect ratio and slightly increase circularity, with potentially important consequences for reduced erosive potential of these daughter particles. The similarity of sizes and shapes of particles recovered from next to the compressor bleed and beneath the exhaust implies that little additional breakage occurs after the compressor. Furthermore, it suggests that sampling is not significantly biased in either case. Future testing involving instrumentation capable of sampling particles from the primary flow path of the engine will allow for pinpointing and isolating the breakage effects to individual compressor stages.

3.6 Conclusions

The Virginia Tech particle ingestion test cell provides a unique capability to perform particle ingestion research on a turbine engine. Not only can the equipment be used to study the effects that the particles have on the engine hardware, but the test cell is also capable of accommodating various instrumentation for validation purposes. In the first stage of shakedown testing, the test cell showed that it is capable of safe and reliable operation including the particle delivery system. Therefore, the doors are open for future particle ingestion research activities.

Analysis of samples collected during the shakedown tests from the undigested C-Spec sand, the engine's bleed valve, and the exhaust system showed that no significant change in particle size occurs between the centrifugal stage of the compressor and the exhaust, with a mean particle size of approximately $45\,\mu\mathrm{m}$ retained after the compressor. This is approximately one third the average particle length of the input C-Spec, which scales to an average particle volume after the compressor approximately $4\,\%$ that of particles in the input dust. The particles appear to not break further as they pass through the centrifugal stage and four rotors of the turbine stage, though their color does change at this point (presumably due to buildup of soot). It might, thererfore, but possible to assume that $\sim 45\,\mu\mathrm{m}$ is a critical size for C-Spec particles in this engine, beyond which no additional breakage upon interaction with the engine hardware occurs. Future work will aim to confirm this. These findings are crucial for the validation of numerical models focusing on estimating erosion damage in turbomachinery. In the upcoming research activities, particle samples will be collected from the compressor stations in order to pinpoint the exact development of particle size within the engine. Moreover, data will be collected for additional input dust types, reflecting the needs of the industry.

Acknowledgments

The authors would like to acknowledge the Office of Naval Research for funding the project under grants N00014-20-1-2538 and N00014-21-1-2397, program manager Dr. Steven Martens. The authors would also like to acknowledge the Naval Air Systems Command (NAVAIR) and Rolls-Royce North America for providing valuable insight into the technical aspects of the project.

References

[1] J. Lekki, "The hazard of volcanic ash ingestion," 2017. [Online]. Available: https://ntrs.nasa.gov/api/citations/20180000365/downloads/20180000365.pdf

[2] C. B. Gabbard, R. E. LeLevier, and J. F. Parry, "Dust-cloud effects on aircraft engines–emerging issues and new damage mechanisms: A case study of a mt. st. helens experience and its implications for nuclear-weapon-lofted dust-cloud effects," 1982.

[3] G. C. Rapp and S. H. Rosenthal, "Problems and Solutions for Sand Environment Operation of Helicopter Gas Turbines," vol. ASME 1968 Gas Turbine Conference and Products Show, 03 1968.

[4] D. Barone, E. Loth, and P. Snyder, "Efficiency of an inertial particle separator," *Journal of Propulsion and Power*, vol. 31, no. 4, pp. 997–1002, 2015.

[5] R. Whittle, "Fatal crash prompts marines to change osprey flight rules," *Breaking Defense*, Jun 2015. [Online]. Available: https://breakingdefense.com/2015/07/fatal-crash-prompts-marines-to-change-osprey-flight-rules/

[6] "Evaluation of the v-22 engine air particle separator," *Department of Defense Office of Inspector General*, Nov 2019.

[7] J. Trevithick, "V-22 Ospreys Still At Risk From Sand And Dust As Navy Attempts Third Engine Filter Redesign," https://www.thedrive.com/the-war-zone/30976/v-22-ospreys-still-at-risk-from-sand-and-dust-as-navy-attempts-third-engine-filter-redesign, nov 12 2019, [Online; accessed 2022-10-23].

[8] P. F. Batcho, J. C. Moller, C. Padova, and M. G. Dunn, "Interpretation of Gas Turbine Response Due to Dust Ingestion," *Journal of Engineering for Gas Turbines and Power*, vol. 109, no. 3, pp. 344–352, 07 1987.

[9] M. G. Dunn, "Operation of Gas Turbine Engines in an Environment Contaminated With Volcanic Ash," *Journal of Turbomachinery*, vol. 134, no. 5, 05 2012.

[10] M. G. Dunn, C. Padova, J. E. Moller, and R. M. Adams, "Performance Deterioration of a Tur-

bofan and a Turbojet Engine Upon Exposure to a Dust Environment," *Journal of Engineering for Gas Turbines and Power*, vol. 109, no. 3, pp. 336–343, 07 1987.

[11] H. Abdullahi, B. Kurpjuhn, M. Resier, and A. Spirkl, "Sand ingestion test on the MTR390 turboshaft engine," *Proceedings of the European Rotocraft Forum*, 09 1998.

[12] M. Murugan, A. Ghoshal, M. Walock, A. Nieto, L. Bravo, B. Barnett, M. Pepi, J. Swab, R. T. Pegg, C. Rowe, D. Zhu, and K. Kerner, "Microstructure Based Material-Sand Particulate Interactions and Assessment of Coatings for High Temperature Turbine Blades," vol. Volume 2D: Turbomachinery, 06 2017.

[13] K. Olshefski, A. Collins, T. Coulon, T. Lowe, and W. Ng, "Development of an anisokinetic particle sampling probe for use in a gas turbine engine compressor," *Frontiers in Mechanical Engineering*, 2022.

[14] K. Olshefski, G. Byun, T. Lowe, and W. Ng, "A methodology for particle visualization at a gas turbine engine inlet," *Manuscript in preparation*, 2023.

4. An Illumination Scattering Technique for Measuring Particle Distribution at a Gas Turbine Engine Inlet

The contents of this chapter are in preparation to be published in *Measurement Science and Technology* (**Olshefski, K.**, Byun G., Vlach T., Lowe, T., Ng, W. (2023) *"An Illumination Scattering Technique for Measuring Particle Distribution at the Inlet Plane of a Gas Turbine Engine"*, Manuscript under review.)

The author's original version of the manuscript has been included. This manuscript is forthcoming and will be published in Fall 2023.

Abstract

The present study demonstrates the novel application of a method for assessing particle distribution at the inlet of a gas turbine engine which is undergoing solid particulate ingestion. Termed the Virginia Tech Particle Visualization by Illuminated Scattering (ParVIS) technique, this method uses only a simple light source and imaging camera to provide users with a qualitative snapshot of inlet particle distribution as well as particle mass flow and number density estimates. This is achieved through the implementation of an in-situ calibration constant which considers particle mass flow rate and integrated particle intensity over the captured region and assumes this relationship is proportional. For subsequent tests, image post-processing then relates the scattering intensity of solid particles to the mass flow through the engine using this calibration constant. For these tests, a Rolls-Royce M250 turboshaft engine was operated at a ground idle condition ($\dot{m}_{M250} = 0.744$ kg s^{-1}) and sand was delivered at a maximum average rate of approximately 1.5 g min^{-1}. Results are reported on a time-averaged basis as well as a time-resolved basis to the frame rate at which successive images are captured (0.25 s). Therefore, this technique allows investigators to gain a broad perspective of particle behavior at the engine inlet while also allowing users to resolve particle flow unsteadiness. Initial results show accurate estimations of injected particle mass flow, with a sand mass flow root-mean-square error of 0.16 g min^{-1} or 11% as compared to the monitored mass flow value using a precision scale. The minimal footprint of the technique along with the relatively precise estimation of parameters of interest make ParVIS an attractive measurement tool when more sophisticated techniques are not feasible or necessary.

4.1 Introduction

Solid particulate ingestion is an inevitability for aircraft operating in hazardous environments. The presence of these particles may be due to atmospheric dust, volcanic ash, or sand when operating in arid zones. Because particle ingestion has been linked to premature engine wear, this phenomenon is of particular interest to researchers and manufacturers alike. This phenomenon has historically had significant impact on equipment, logistics and, in extreme cases, resulted in loss of life. In December 1989, a KLM Dutch Airlines 747-400 operating near Anchorage, AK unintentionally flew through the ash cloud of a recent volcanic eruption of Mt. Redoubt which sent ash more than 30,000 feet into the atmosphere [1]. The aircraft was equipped with four General Electric CF6-80C2 engines and experienced a four-engine flame-out which caused the flight crew to make an emergency landing [2]. All four engines from the aircraft were replaced, costing the airline over 80 million dollars in replacements and repairs [3]. During periods of operation Iraqi Freedom, the United States Army had reduced availability of its CH-47 helicopters due to 75% to 95% premature engine failures which were directly linked to sand ingestion [4]. In 2010 after the eruption of the Eyjafjallajökul volcano, the subsequent ash cloud caused a total closure of European airspace. This resulted in the cancellation of thousands of flights and an estimated economic impact of nearly $2 billion [5]. In 2015, an MV-22 Osprey crashed during a training exercise in Hawaii, claiming the lives of two US Marines and injuring twenty other personnel [6]. The cause of the fatal crash was attributed to dust ingestion resulting in an engine failure.

There has been substantial effort aimed at understanding the effects of particle ingestion on aircraft engines [7–13]. Much of this work has focused on the impact of particle deposition on turbine sections, blockages of cooling vanes, and erosion characteristics due to particle interactions [14, 15]. Early work by Tabakoff and collaborators explored the effects of particle impacts on turbomachinery materials with respect to varying particle velocity [16–22], particle impact angle [16, 18], and particle mass [18, 22]. Dunn, Baron, and Miatech conducted early on-engine tests aimed at determining the performance degradation rate of gas turbine engines when operating in particle-laden environments [23]. Here, they concluded that engine deterioration is a function of particle concentration as well as other parameters. Additionally, they found that the damage to these engines is proportional to exposure time. Efforts by Clarkson have focused on developing an aggregate model for predicting operational safety limits based on exposure levels and duration. Here, the authors summarize several previous studies into a single chart that illustrates operating regions which may cause various levels of engine damage severity [24].

Despite these efforts, there is still a need for greater understanding of particle flow paths as they traverse an engine and for a more accurate depiction of particle behavior at the inlet plane. Papadopoulos et al. conducted preliminary level demonstrations of an in-situ particle detector which identifies plasma interaction and dissociation with particles to determine particle size and relative concentration [25]. Moon et al. have developed a scattering-extinction based technique which leverages a machine-learning library to assess particle size, shape, and concentration at a gas turbine inlet [26, 27]. Others have sought to develop airborne instrumentation which is capable of providing particle information about atmospheric aerosols and ice crystals [28–31]. Baumgardner et al. developed an on-wing instrument which combines five separate probes into one to assess atmospheric particle concentration and liquid water content [28]. Typically, these instruments sample particles in the sub-to-single-micron range and are point measurements instead of providing particle distribution over an area. Additionally, each of these methods listed are limited by their complexity and do not yield a comprehensive description of the inlet particle distribution.

There has been significant effort aimed at capturing particle characteristics using extinction and scattering based planar imaging techniques, particularly in the liquid sprays field [32–34]. The Structured Laser Illumination Planar Imaging (SLIPI) technique developed by Berrocal and Kristensson is an optical-imaging technique primarily used to visualize a liquid spray and has developed into a primary characterization method in the atomization and sprays field [35–37]. Gaigalas, Wang and Choquette used a commercial spectrometer and integrating sphere to assess the scattering and absorption cross section of microspheres suspended in water [38]. The authors were able to fit the data with Lorenz-Mie scattering cross section and a correction factor to find the relative reduction in scattering cross section by absorption. Evanoff and Chumanov showed that a method, termed standard subtraction, can be appropriate for determining the concentration of silver nanoparticles suspended in water independent of size or shape [39]. Lastly, Yu et al. developed a dust concentration measurement method based on laser scattering and showed that mass concentration has a linear relationship to scattered light intensity [40].

Providing a means for determining particle ingestion quantities and particle distribution at the gas turbine inlet can be particularly valuable to researchers and engine manufacturers alike. To this end, we present an application of a novel particle visualization technique which is under development and has been tested at the inlet of a Rolls-Royce M250-C20B engine at the Virginia Tech Particle Ingestion Engine Test Stand to provide users with a comprehensive description of inlet particle distribution, particle mass flow, and particle number density estimates at ground idle conditions. The work contained herein is presented as follows: Section 6.2 presents an overview of model theory and method limitations. Section 4.3 provides details of the experiment conducted. Section 4.4 gives an assessment of model uncertainty. Section 5.4 discusses experimental results and provides discussion on the findings. Finally, Section 5.3.3 provides conclusions which may be drawn from the previously discussed results.

4.2 Particle Visualization by Illuminated Particle Scattering (ParVIS) - Instrument Principles

Execution of the technique begins by first projecting a laser sheet into an area of interest. Next, an imaging camera is positioned such that the viewing plane is parallel to the laser sheet. As particles are seeded into the flow, which is normal to the viewing plane, images are captured on a continuous basis and saved for analysis. Post-processing of the captured images provides quantities of interest.

4.2.1 Model Theory

The basis of this technique relies on the development of a relation between the pixel count given by the imaging system and the scattered light by the presence of particles in the laser sheet. It is given by Yeaton et. al. in [41] that the total number of scattered photons, N_p, over a given time may be written as

$$N_p = \frac{P_0 n L_x \lambda \Omega \Delta t \epsilon}{hc} \left(\frac{d\sigma}{d\Omega} \right) \sin^2(\beta) \tag{4.1}$$

where P_0 is the laser power, L_x is the length of the measurement volume, λ is the laser light wavelength, Ω is the light collection solid angle, Δt is the time of data acquisition, ϵ is the efficiency of the detection system, h is Planck's constant, c is the speed of light, $d\sigma/d\Omega$ is the particle scattering cross-section, and β is the angle between the laser plane and the imaging device. This relation provides that the number of detected photons per unit time is solely a function of particle number density, n, as

$$\dot{N}_p = \frac{N_p}{\Delta t} = \Gamma n \tag{4.2}$$

where Γ is expressed in equation (4.1) as a collection of constant values which are dependent on the experimental setup and need to be calibrated for by measurement [41]. With this relation, we establish that the count in a given pixel is estimated as

$$S_{i,j} = \dot{N}_p \cdot QE \cdot AD \tag{4.3}$$

where QE is the quantum efficiency and AD is the gain sensor conversion of the imaging device, respectively. Integrating this expression over the entire field of view directly converts the total number of scattered photons in an image to the pixel count used to estimate particle mass flow.

4.2.2 Establishing a Calibration Constant

With the previous establishment of a link between observed pixel count and particle scattered light intensity, images may be processed to estimate particle mass flow as well as local and total particle concentration throughout the captured domain. This is achieved by first estimating a calibration constant, C, by providing a known quantity of total particle mass flow for one data series and determining the integral pixel intensity in the domain for that data. For these studies, the known quantity was calculated as the change in mass of a sand feeding system over the time period of data collection for one data series using a high precision scale. Further detail of this system is provided in section 4.3.2. We assume a direct relationship between captured pixel intensity and mass loading as

$$\frac{\dot{m}_{ij}}{\dot{M}} = \frac{S_{i,j}}{\int S_{i,j} dA} \tag{4.4}$$

where $\dot{m}_{i,j}$ is the particle mass flux through a pixel, $\dot{M}$ is the total mass flow through the region for the data series, $\int S_{i,j} dA$ is the integral quantity of pixel intensity over the computational domain, and i, j are the pixel indices. The total mass flow rate is calculated as

$$\dot{M} = \int \dot{m}_{ij} dA \tag{4.5}$$

over the region of interest. The calibration constant is then calculated as

$$C = \frac{\dot{M}}{\int S_{i,j} dA} \tag{4.6}$$

so that the per pixel particle mass flux is determined as

$$\dot{m}_{ij} = C S_{i,j}. \tag{4.7}$$

For all additional collected data, the calibration constant is used to determine quantities of interest. For this study, a time period of one minute was chosen to represent a data series. During a sand loading campaign, several data series are collected. The particle mass flow value calculated for a sand loading campaign, $\dot{M}$, is estimated as the average mass flow over the included data series.

4.2.3 Particle Number Density Estimate

In calculating particle number density (concentration, kg m^{-3}) values, we assume a constant bulk flow velocity consistent with the inlet mass flow condition. The particle volume fraction Φ is defined as

$$\Phi = \frac{\forall_p}{\forall_g} \tag{4.8}$$

where $\forall_p \& \forall_g$ are the volume of particles and gas in the the region respectively [42]. It follows then, that particle concentration (σ_p, kg m^{-3}) is found as

$$\sigma_p = \Phi \rho_p \tag{4.9}$$

where ρ_p is the material density of the particle. In the prior section we showed a method for calculating the particle mass flow rate, $\dot{M}$, which may be equivalently represented as

$$\dot{M} = \dot{\forall}_p \rho_p \tag{4.10}$$

where $\dot{\forall}_p$ is the volumetric flow rate of particles. We can estimate total particle concentration as

$$\sigma_p = \Phi \rho_p = \frac{\dot{\forall}_p}{\dot{\forall}_g} \rho_p = \frac{\dot{M}}{\dot{\forall}_{air}} \tag{4.11}$$

where $\dot{\forall}_{air}$ is the volumetric flow rate of air through the engine inlet. It is important to note that both the estimated mass flow rate, $\dot{M}$ and the integrated intensity values, $\int S_{i,j} dA$ assume that all particles have been captured within the images. For this study, previous investigations determined that a one inch (2.54 cm) diameter region would be sufficient to capture greater than 95% of particles under similar flow conditions with this sand delivery nozzle configuration. Therefore, the authors assume any particles which have not been captured by imaging constitute a statistically insignificant portion of the overall mass flow and the reported values of the technique are comprehensive.

4.2.4 Method Considerations

For each sand loading campaign, both sand-free images and images including sand are captured. All images are captured as 16-bit, monochromatic, grayscale images. It was determined that over the field of view, the scattering angle varies by $\pm 2°$. For these tests, the particles tested have a highly nonuniform shape and size distribution. The particles of interest range from approximately 75 μm to 1200 μm as described in section 4.3.1. The appropriate particle scattering regime is determined using the non-dimensional size parameter, x, as

$$x = \frac{\pi D}{\lambda} \tag{4.12}$$

where λ is the incident wavelength and D is taken as the particles diameter [43]. Geometric optics is sufficient in capturing the scattering intensity when the particle size is much larger than the wavelength ($x \geq 10$) which is the case for the current study [44]. Using this approximation, the variation of pixel intensity with scattering angle is considered in Figure 4.1 for a range of particle aspect ratios. In this figure the scattering profile considered is of a poly-dispersed particle with a spherical volume equivalent size of 155 μm in diameter at an incident wavelength of 514.5

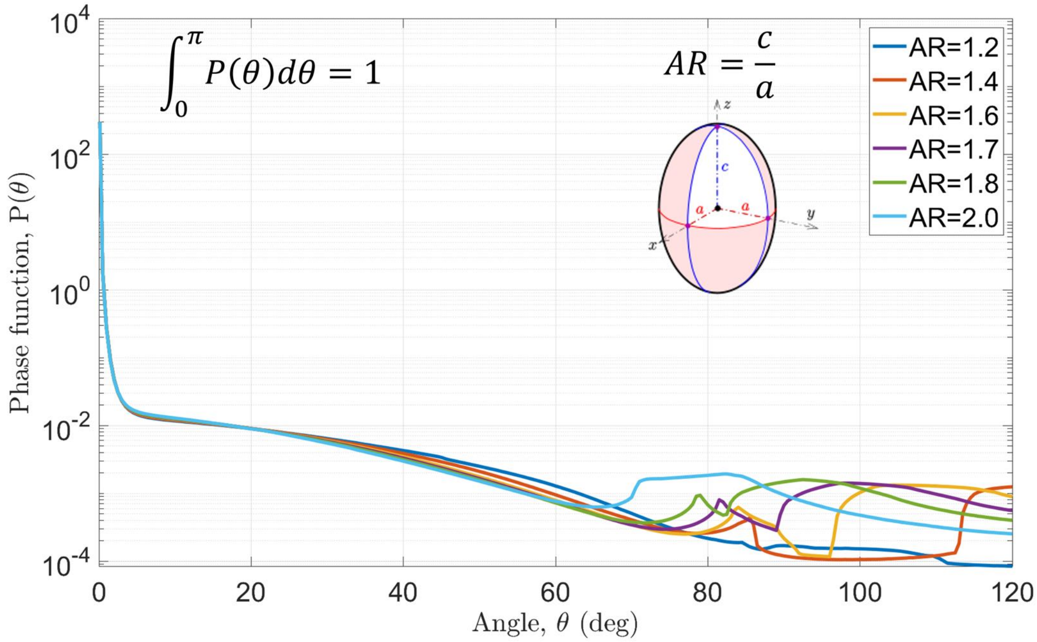

Figure 4.1: Variation of scattering intensity is considered for a particle with equivalent spherical volume of 155 μm in diameter with varying aspect ratios at a wavelength of 514.5 nm. For the studies described here, it is shown that scattering intensity may vary with aspect ratio over the relevant range ($1.0 \leq AR \leq 4.25$).

nm which is representative of the experimentally ingested particles. Within the relevant field of view ($88^\circ \leq \theta \leq 92^\circ$) it is evident that scattering intensity may vary with particle aspect ratio. Consideration for these effects is discussed further in Section 4.5.2.

As outlined in Section 4.2.2, the calibration of the data processing scheme necessitates an initial known mass flow rate to establish the calibration constant (C) utilized to compute parameters of interest. Furthermore, as established in Section 4.2.1, the intensity of an image, $\int S_{i,j}dA$, is directly proportional to the number of detected photons by the imaging system, N_p, which is highly dependent on the specific experimental setup under consideration. The precise estimation of these parameters is crucial to realizing an accurate calibration constant, C. Therefore, alterations to the light source power, test material, or camera position will affect the overall pixel intensity in the field and, consequently, the computed parameters of interest. To mitigate this risk, it is recommended that a new calibration constant be established whenever modifications are made to the testing configuration. Moreover, a sensitivity analysis should be conducted in future studies to determine the degree of sensitivity of this parameter and to identify which experimental quantities contribute the most uncertainty to the term. Finally, care should be taken to ensure individual image pixels are not overly saturated, particularly for the calibration case. Oversaturation makes the true value of the pixel intensity indiscernible. This will result in an inaccurate calibration constant estimate and an overestimation of total particle mass flow.

Additional consideration is given to the efficacy of the presented method under a wide range of relevant flow scenarios. While the present investigation considers particle densities which are moderately sparse, in the extreme case, such as a "brown-out" condition, whereby the laser sheet is unable to fully penetrate the domain on a time resolved basis, measurement uncertainty may reach excessive levels and the method would in fact be ineffective. Engineering judgement should be used to assess hardware configuration effectiveness. Furthermore, for cases where particle densities reach excessively high levels it may be necessary to mitigate for multiple light scattering effects by data post-processing with methods such as the previously described SLIPI technique. In the context of the present study, investigations of dilute suspensions revealed no evidence of secondary scattering. Preliminary benchtop experiments indicated that this phenomenon need not be taken into account when imaging concentrations of C-Spec below $2\,\mathrm{g\,m^{-3}}$. Nonetheless, given the possibility of this effect becoming relevant at higher concentrations, future research should aim to consider and bracket this uncertainty.

As a final note, it should be recognized that the methodology outlined in this study relies on the assumption that the primary flow direction is orthogonal to the imaging plane. This guarantees that the scattered light from a given particle is captured only once. If, for instance, the flow exhibited pronounced anisotropy or a recirculation region were present, this assumption may no longer be valid. This would result in inaccurate estimates of the mass flow and concentration values. Nevertheless, given that the present investigation focuses on the inlet of a gas turbine engine, it is reasonable to assume that the flow is predominantly unidirectional.

4.3 Validation Experiment

4.3.1 Test Particles

The ingestion material of interest for these tests is MIL E-5007C, commonly known as C-Spec, which is a commercially available mixture of crushed quartz. This material is known for having a wide distribution of particle sizes which is representative of dusts encountered by operational aircraft. Particle sizes of C-Spec range from roughly 50-1300 μm. The particle size distribution from the manufacturer provides that only 3% of particles are smaller than 75 μm and 50% of

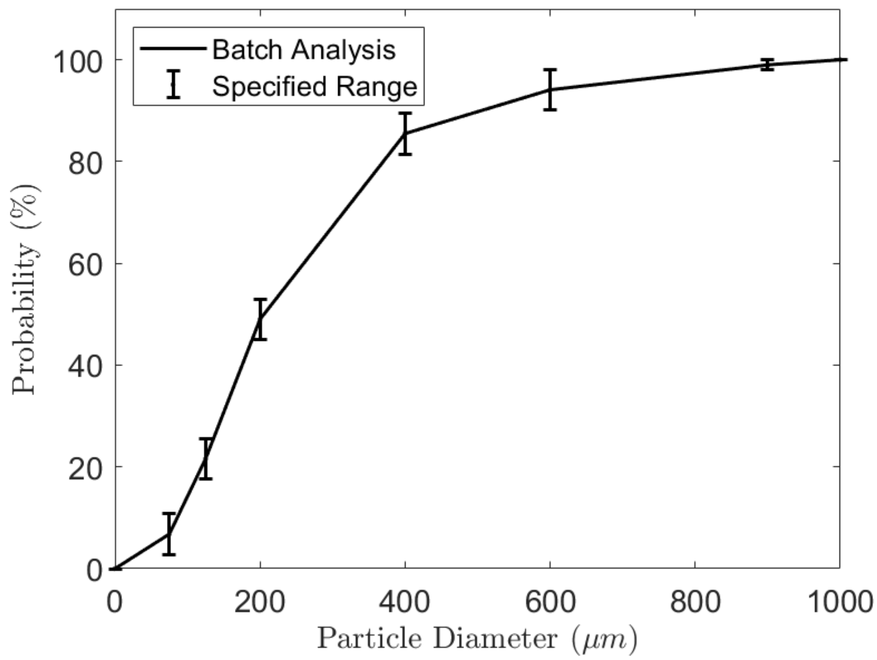

Figure 4.2: Cumulative size distribution plot of MIL E-5007C, more commonly referred to as C-Spec. The manufacturer estimates that C-Spec particle sizes from roughly 50-1300 μm with 97% of particles larger than 75 μm and 50% of particles being larger than 200 μm on a mass basis. C-Spec is composed primarily of quartz therefore, a particle density of 2650 kg m^{-3} is assumed.

particles are larger than 200 μm on a mass basis. These estimates are confirmed in the cumulative size distribution plot shown in Figure 4.2 which is taken from Collins, 2021 [45]. Additionally, the material is comprised of a range of particle shapes. Figure 4.3, taken from Vlach et. al (2023), shows that the composition of C-Spec varies in aspect ratio (AR) from approximately $(1.0 \leq AR \leq 4.25)$ [46]. Because the mixture is almost exclusively quartz, a particle density of 2650 kg m^{-3} is assumed.

4.3.2 Test Facilities

All tests discussed herein were conducted at the Virginia Tech Particle Ingestion Engine Stand using a Rolls-Royce model M250-C20B engine operating at ground idle condition. This condition corresponded to an engine mass flow rate of 0.744 kg s^{-1} and a bulk flow velocity of 64 m s^{-1} as measured by the test cell data acquisition system. Sand was introduced into the inlet flow at two conditions, a full loading condition and a half-loading condition. The full loading condition resulted in a particle concentration of 45 mg m^{-3} and the half-loading condition produced a particle

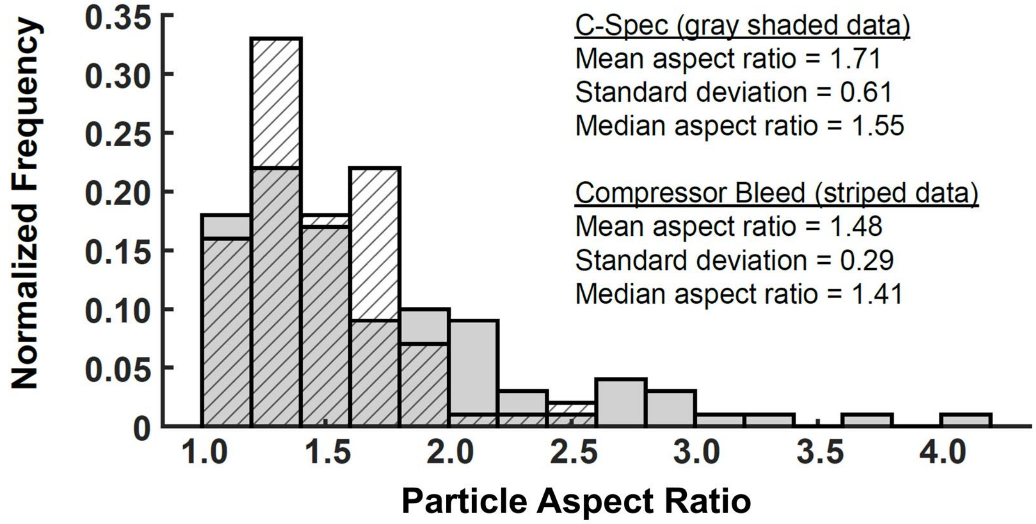

Figure 4.3: Particle aspect ratio plot of C-Spec test dust. This plot from [46] shows a distribution of particle aspect ratios which range from $1.0 \leq \text{AR} \leq 4.25$.

concentration of 22.5 mg m^{-3}. These values were chosen based on evidence provided by Clarkson that exposure at these levels may result in significant engine deterioration and erosive damage [24]. Four tests were conducted, two at each loading condition, at five-minute intervals of sand exposure. A table of the testing conditions can be seen in Table 6.1.

Engine Test Stand

Researchers at Virginia Tech are interested in performing on-engine sand exposure tests to learn more about how ingestion events lead to engine performance deterioration. Consequently, the Virginia Tech Particle Ingestion Engine Test Stand has been established as pictured in Figure 4.4. This facility is a fully functioning engine test facility located at the Advanced Propulsion and Power Laboratory (APPL) at Virginia Tech. The facility is currently configured for a Rolls-Royce model M250-C20B turboshaft engine which produces approximately 450 horsepower when operating at full capacity. The facility also includes an adjacent user control room which provides noise insulation as well as protection for personnel in case of emergency, an engine stand, auxiliary oil and fuel systems, an extensive suite of data acquisition and instrumentation for remote engine control and performance evaluation, and a water brake dynamometer system for power absorption. The facility is capable of continuous engine operation at a ground idle setting and up to one hour at full power for the model M250-C20B.

Engine Condition	$\dot{m}_{M250}$(kg s^{-1})	Run	Duration (min)	σ_p(mg m^{-3})	Test Condition
Ground Idle	0.744	1	5:00	0	Calibration
			5:01	45	Sand Loading - High
		2	5:00	0	Calibration
			5:10	22.5	Sand Loading - Low
		3	5:00	0	Calibration
			4:21	45	Sand Loading - High
		4	5:00	0	Calibration
			4:18	22.5	Sand Loading - Low

Table 4.1: Engine test conditions given the engine throttle condition, engine air mass flow rate ($\dot{m}_{M250}$), the run number, the duration of the run, the calibrated particle mass concentration (σ_p), and the condition being tested. Calibration cycles were periods used for instrument adjustment and no sand was ingested during this time.

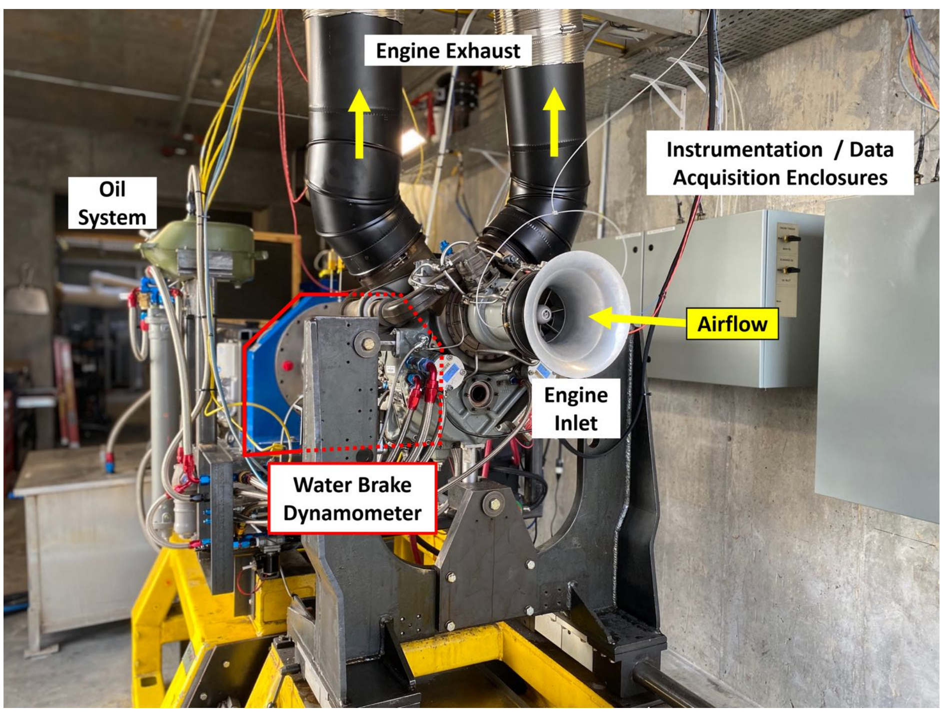

Figure 4.4: Virginia Tech Particle Ingestion Engine Test Stand with a Rolls-Royce M250-C20B engine installed. Also pictured are auxiliary systems such as the water brake dynamometer which is used for power absorption, the engine oil system for adequate lubrication, and the instrumentation and data acquisition enclosures. These enclosures contain temperature and pressure monitoring equipment as well as engine controls hardware.

Particle Seeding

Particle seeding was achieved using an AccuRate particle feeder to provide a constant flow of C-Spec particles into the engine inlet. The feeder sat atop an Adam Equipment LTB 6002e scale and the weight of the particle feeder was continuously monitored throughout testing. This allowed for a precise measurement of total sand mass flow during each run. The feeder and scale were securely mounted to a platform above the engine inlet flow barrel. The particle feeder has a hopper that was filled with the sand sample, and a rotating helix which carried the sand to an exit nozzle. Depending on the setting, the feeder is capable of providing sand at a feed rate from 0.2 g min^{-1} up to 2 g min^{-1}. From the exit nozzle, sand was routed into tubing and through an Exair Line Vac pneumatic particle conveyor. This particle conveyor works by:

1. Facility compressed air is directed into an annular plenum chamber.
2. The flow is directed through nozzles into the throat of the conveyor.
3. The resulting jet creates a low pressure region near the conveyor intake.
4. The vacuum draws particles through the conveyor and into the delivery nozzle.

The Line Vac creates a vacuum of -29.9 kPa with a supply pressure of 552 kPa. Previous investigations determined this pressure was adequate to supply particles to the engine inlet without backflow. Particles entered the inlet flow through a delivery nozzle which was positioned at centerline. The particle feeder, conveyor, and delivery nozzle are all used in conjunction to supply a consistent particle laden flow to the engine inlet.

4.3.3 Execution - Image Capture

A diagram of the experimental setup is shown in Figure 6.1. A Coherent Genesis CW laser with up to 1W output at 514.5 nm wavelength was directed to a Thorlabs Scanning Galvanometer Mirror which induced a laser sheet at an assigned scanning frequency. The laser sheet is then truncated to a 2.54 cm (1 in.) strip by passing through an optical window affixed to the inlet test section. The laser sheet is projected orthogonal to the direction of flow from the twelve o'clock position to the six o'clock position. A FLIR Blackfly S BFS-U3-31S4 camera fitted with an Edmund Optics 35 mm lens and 514.5 nm filter continuously capture images at an exposure time of 0.25 seconds. This camera is placed 152.4 cm (60 in.) directly upstream of the laser sheet at an angle of two degrees relative to the laser plane as seen in Figure 6.1. This slight angle facilitates an unobstructed view of the inlet centerline, the primary region of interest, as shown in Figure 4.6. Here, a particle

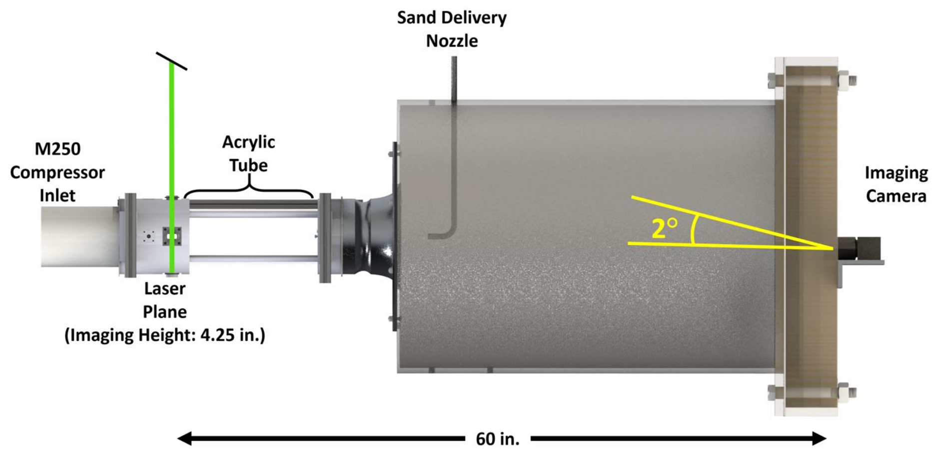

Figure 4.5: Experimental setup of the ParVIS technique. A one-inch-wide laser plane is projected from 12 o'clock to 6 o'clock directly upstream of the inlet of the M250 engine. An imaging camera is positioned sixty inches upstream of the laser sheet and is oriented to view the entire strip at an angle of 2°. This slight angle allows the camera to image the center region of the laser strip where the majority of particles are present. Otherwise, the sand delivery nozzle may obstruct this viewing angle.

sampling probe, used for a parallel study, is positioned such that the probe opening is concentric with the cylindrical test section. We can see that the center, the region of primary interest, is in clear view. A series of clean background images are then taken during engine operation prior to sand exposure. Once sand delivery begins, images are taken continuously until loading stops.

A background image is constructed from the mean values of a series of 240 continuous sand-free images. This composite image is then used for background subtraction. Individual sand loading images are background subtracted to expose only sand particles passing through the laser sheet. An auto-thresholding scheme using Otsu's method is then applied to each background subtracted image to ensure complete isolation of sand particles [47]. The background subtracted images are summed together to create a single composite image which represents one minute's worth of sand loading imagery. For the experiments conducted, a series of 240 sand loading images make up one composite image (one minute's worth of data). The resulting composite image constitutes a single data series. Multiple data series images are gathered over the duration of one sand loading campaign. Four exposure campaigns occurred during the experiment analysed; two at the full loading condition (45 mg m^{-3}) and two at the half loading condition (22.5 mg m^{-3}).

For all results discussed, images were captured using the one-inch-wide laser strip described above and depicted in Figure 4.6. However, full utility of the ParVIS technique can be realized

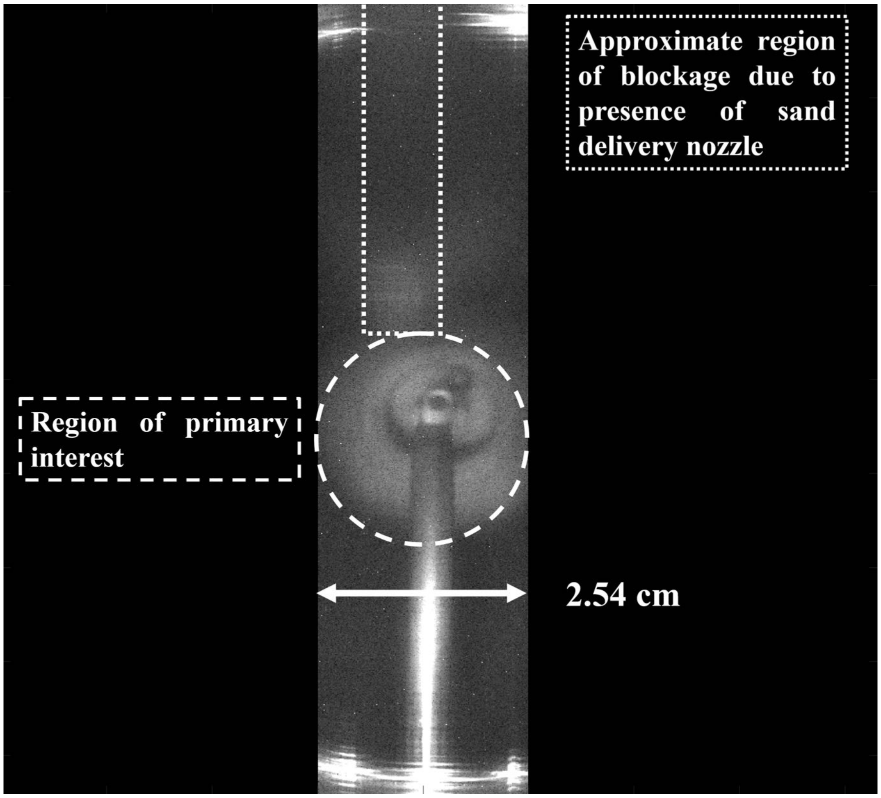

Figure 4.6: Image of background captured by Blackfly camera. The probe pictured, used in a parallel study, is positioned such that the opening is directly on the inlet centerline. We can see slight blockage in the upper-left quadrant due to the presence of the sand delivery nozzle. However, the region of primary interest, a one-inch diameter region about the center point, is unobstructed. This image has been contrast-enhanced to allow for structure identification.

by imaging a total cross section of the inlet plane. Further discussion on this will be presented in Section 5.3.3 below.

4.4 Measurement Uncertainty

An uncertainty analysis was performed to determine the precision of reported results. Overall uncertainty was calculated using a root-sum-square of individual uncertainty contributions as

$$\delta R = \left\{ \left(\frac{\partial R}{\partial x_1} \delta x_1 \right)^2 + \left(\frac{\partial R}{\partial x_2} \delta x_2 \right)^2 + \cdots \left(\frac{\partial R}{\partial x_N} \delta x_N \right)^2 \right\}^{1/2} \tag{4.13}$$

where $\partial R/\partial x_i$ is the absolute uncertainty and ∂x_i are the individual contributions [48]. This method is a well-established mathematical principle used to estimate the uncertainty in a calculated quantity that depends on several measured quantities, each with their own uncertainties. By taking into account multiple sources of uncertainty, this approach provides a weighted estimate that is particularly useful in identifying the measured quantities which have the greatest contribution to the overall inaccuracy in the calculated quantity, thus facilitating the identification of primary sources of error and informing experimental design improvements. Applying equation (4.6) to equation (4.13), the overall uncertainty of the calibration constant, C, is found to be

$$\delta \mathrm{C} = \left\{ \left(\frac{\partial \mathrm{C}}{\partial \dot{\mathrm{M}}} \delta \dot{\mathrm{M}} \right)^2 + \left(\frac{\partial \mathrm{C}}{\partial \mathrm{S}} \delta \mathrm{S} \right)^2 + \left(\frac{\partial \mathrm{C}}{\partial \mathrm{A}} \delta \mathrm{A} \right)^2 \right\}^{1/2} \tag{4.14}$$

where it was determined that the contributing sources of error included $\dot{M}$, the mass flow rate of sand from the sand delivery system, S, the total intensity in the image, and A which is the area of a pixel. For all data, engineering judgement was used to identify the primary sources of uncertainty. A calibration study was conducted to determine the variation in the feed rate of sand exiting the sand delivery system. This investigation determined that the uncertainty associated with the sand delivery was ±0.10 g min^{-1}. The uncertainty of the calculated intensity was assumed to be a function of the noise specification of the camera used. Using the camera specifications provided by the manufacturer, the uncertainty of the measured intensity is estimated to $\pm 2\%$ at the full capacity of photons [49]. Although a calibration plate was used to assess pixel size, it was assumed that a user may misjudge this value by as much as ±2 pixels. With these considerations, a total uncertainty estimate of the calibration constant was found to be $\delta C = \pm 6$ % with the majority of this value coming from the uncertainty associated with the sand delivery system. This value represents the 95% confidence interval.

4.5 Results and Discussion

As previously stated, four exposure campaigns occurred during the experiment analysed; two at the full loading condition (45mg m^{-3}) and two at the half loading condition (22.5 mg m^{-3}). The results of these experimental runs are presented below. We provide discussion of both qualitative and quantitative findings. From these results, an extensive understanding about inlet particle distribution can be established. As mentioned in Section 4.3, the full utility of this technique is realized by imaging a full cross section of the inlet. A full cross section analysis was attempted for this set of experiments but the subsequent images were unusable due to excessive glare and reflection on the acrylic tube of the test section affecting the particle mass flow estimates. Extensive effort was made to reduce these inconsistencies with little success. This will however be the focus of future studies. The researchers concluded that the primary cause of the problematic glare was due to structural interference of a parallel experiment being conducted. Therefore, the authors are confident the issue can be resolved for future investigations.

4.5.1 Qualitative Observation

Examining the composite grayscale image in Figure 4.7, we can gain a broad perspective of particle behavior over a one-minute time span for the high sand loading case (Figure 4.7A) as well as the low particle loading case (Figure 4.7B). First, it is clear that the overall distribution of particles is highly non-uniform and is primarily clustered about the centerline region for both cases. As expected, there is also a higher density of particles present in the high loading case. Lastly, it is evident that there is a higher presence of particles in the bottom half of the domain than in the top half. This trend was also observed in all other data series. We confirm this observation by looking at how the mean grayscale intensity values vary over the vertical direction as seen in Figure 4.8. For this analysis, data is only taken from the right half of the domain to avoid biasing the findings due to the presence of the sand delivery nozzle in the upper-left quadrant as shown in Figure 4.6. In Figure 4.8, we consistently observe spikes in intensity throughout the lower half of the region. Conservatively assuming particles exit the sand delivery nozzle at $10\,\mathrm{m\,s^{-1}}$, a particle will traverse the length of the test section from the nozzle exit to the laser sheet, a distance of approximately 0.6 m, in approximately 0.06 seconds. Using this time (t) as a constraint, a kinematic analysis can estimate the maximum vertical drop of a given particle (dy) as

$$dy = \frac{1}{2}gt^2 \tag{4.15}$$

where g is the gravitational constant. Equation (4.15) provides that particles should fall no more than 1.8 cm along the traversed length. Therefore, the presence of particles seen in the lowest regions of Figure 4.8 cannot be due to the influence of gravity alone. Instead, these are likely large C-Spec particles which when exiting the sand delivery nozzle, have dropped to the bottom of the test section instead of being taken by the bulk flow. They are then likely drawn to the inlet by the bulk flow and bounce along the bottom of the test section before reaching the laser sheet and

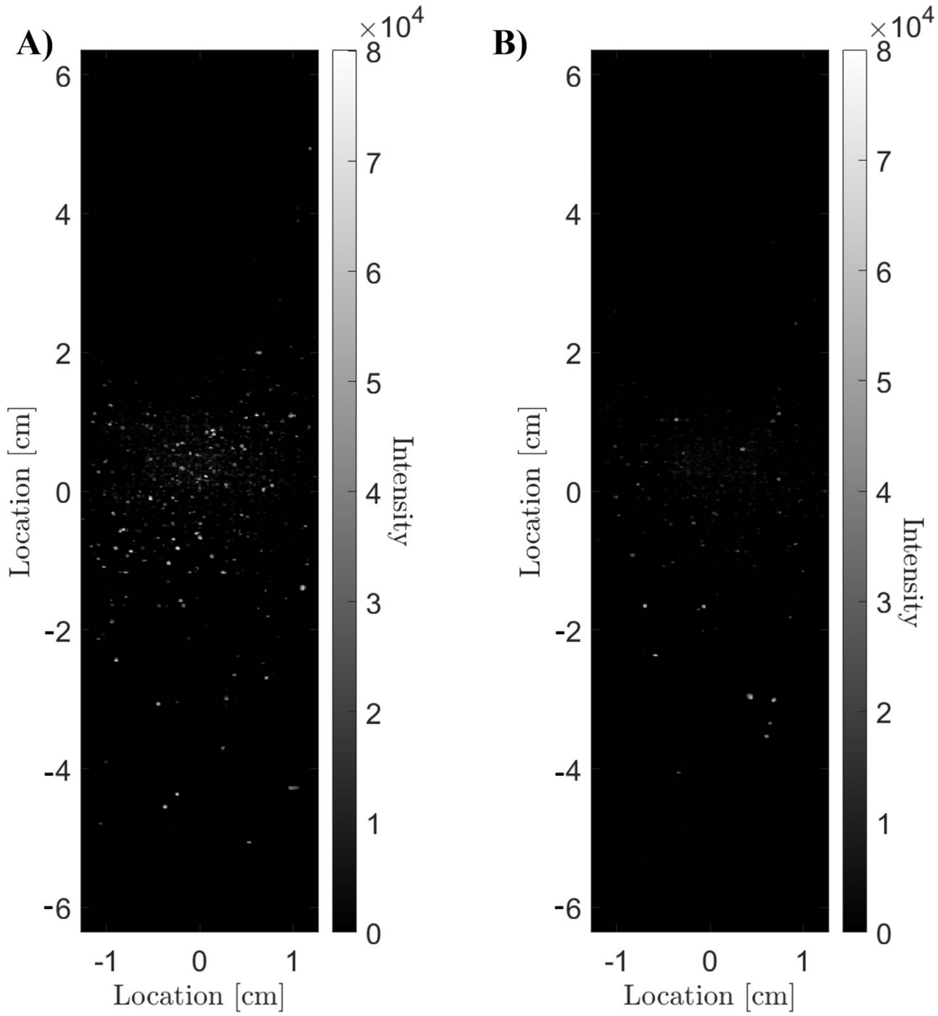

Figure 4.7: Composite images taken compiled over a period of one minute for a high particle loading case (A) and a low particle loading case (B). We observe nonuniform distribution in both images as well as the presence of some particles in the lower half of the domain.

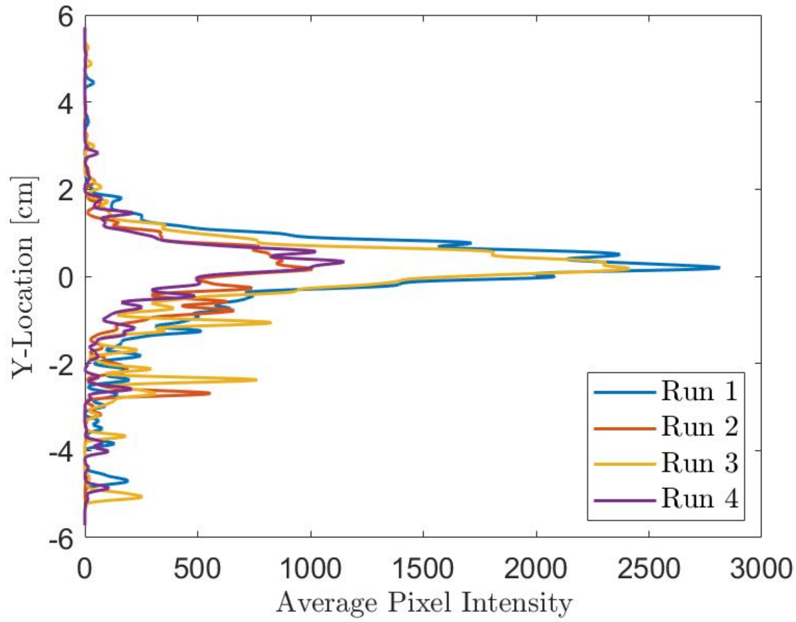

Figure 4.8: Plot of varying average grayscale intensity values with vertical location. Here we confirm a higher presence of particles in the lower half of the domain than in the upper half. Kinematic analysis indicates that the presence of particles in this region is not due to the effects of gravity alone.

being imaged. While not a significant portion of the overall mass ingested by the engine, this is an important and interesting finding as it may provide critical information about particle flow paths to researchers.

4.5.2 Mass Flow Estimation

Using the data gathered over each of the data series, an average mass flow estimate for each experimental loading campaign is calculated. The accuracy of the ParVIS technique is tested by comparing the mass flow value found by the model, to that of the known value from the scale measurement as well as the value obtained by the Virginia Tech scattering-extinction particle sensor as shown in Figure 4.9 [27]. Data is reported with error bars representing a root-mean-square deviation (RMSD) of calculated mass flow rate. We see that all three values are in good agreement, with the values obtained by the ParVIS method falling within a maximum root-square-mean error of 0.16 g min^{-1} or 11% of the monitored value using the precision scale. Having the ability to accurately estimate the total amount of particles passing through the inlet plane is a highly desirable capability for researchers as well as manufacturers who are invested in reducing engine damage as

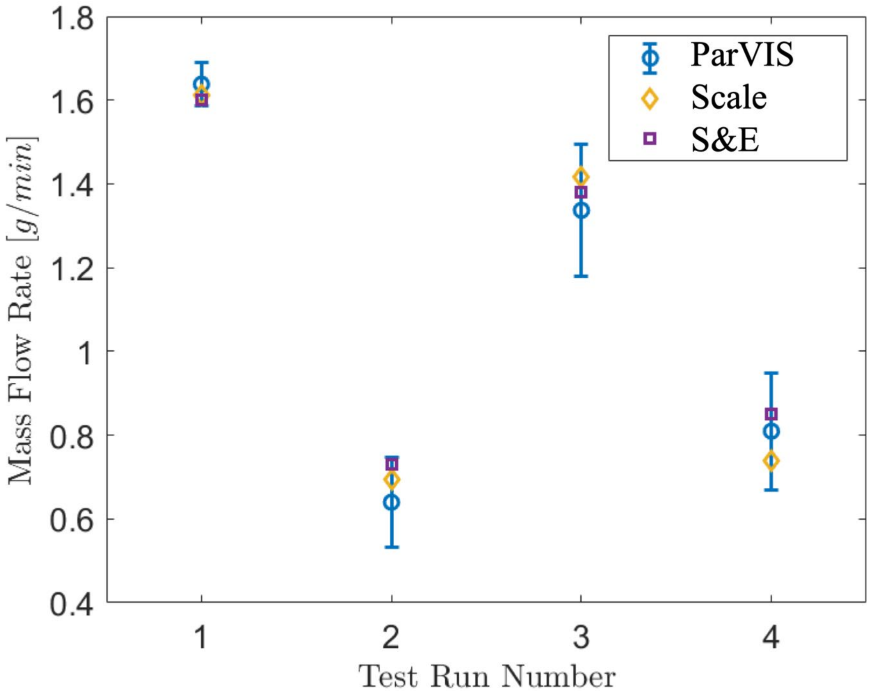

Figure 4.9: Mass flow estimates for the ParVIS technique (blue), the Virginia Tech Scattering-Extinction technique (purple), and the value obtained with the precision scale (yellow). The error bars associated with the ParVIS method are representative of the root-mean-square deviation (RMSD) of the measurement. All values are in agreement within the error bounds of the ParVIS method.

a result of particulate ingestion.

As previously mentioned in Section 4.2.4, the influence of the variation in scattering angle due to the particle aspect ratio distribution of C-Spec may contribute to the uncertainty of the calibration constant, C. Recent work by Vlach et al. has shown that the representative range of C-Spec particle aspect ratio varies from $1.0 \leq AR \leq 4.25$ [46]. The influence of this increased uncertainty can be seen in the error shown in Figure 4.9 where it is noticeable that the error exceeds the 6% uncertainty estimate of the previous analysis. This suggests that this error may be reduced by the study of test dusts with a more narrow size and shape distribution. Strategies for the mitigation of this error will be the focus of future investigations.

4.5.3 Particle Concentration

Although, total mass ingested by the engine is useful for understanding life wear trends, it is typical to gauge damage trends in terms of ingested particle concentration as seen in Clarkson, 2017 [50]. Using engine volumetric flow parameters, a local particle concentration map can be formed as seen in Figure 4.10. Here, a pixel-binning scheme is applied to the data from Figure 4.7 and pixel count values are spatially averaged over the region. The width selected for this technique ensures that the region of averaging is larger than the maximum particle size being investigated. This filter allows for easier interpretation of the data and for users to quickly identify areas of greatest particle aggregation. Figure 4.10 again highlights the non-uniform particle distribution within the domain and we can more clearly see the local zones of greatest particle density. Figure 4.10A is taken from a single data series from Run 1, a run with high sand loading and Figure 4.10B is compiled from a single data series from Run 2, a run with low sand loading. While the regions of greatest concentration are similar for both data sets, the concentration magnitude of the data set with the highest sand loading (Figure 4.10A) is more than twice that of Figure 4.10B, as expected.

Coupling system knowledge with observations from the local particle density map presented in Figure 4.10, researchers can draw powerful conclusions about particle paths and particle-hardware interactions. For example, knowing the majority of particles ingested are concentrated approximately at the centerline, we can expect significant particle interaction with the inlet guide vane hub of the M250. Consequently, this will result in high rates of erosion on the hub and will also cause particles to bounce radially outward after colliding with the structure. Had this experiment been conducted using a turbofan engine instead, researchers may then conclude that the bulk of particles entered the core flow region as opposed to the bypass region. This can then inform researchers about areas of greatest interest for implementing or developing wear resisting strategies. Having a more complete depiction of the distribution of particles entering an engine is the first step to understanding how to mitigate against wear due to solid particulate ingestion.

4.5.4 Time Resolved Data

While increasing the understanding of broad particle flow behavior is the primary goal of the ParVIS technique, there are also practical reasons for observing the data on a time resolved basis. In Figure 4.11, the previously determined calibration constant is used to calculate the mass flow rate for each frame in a loading campaign for two different loading levels. These data series comprise

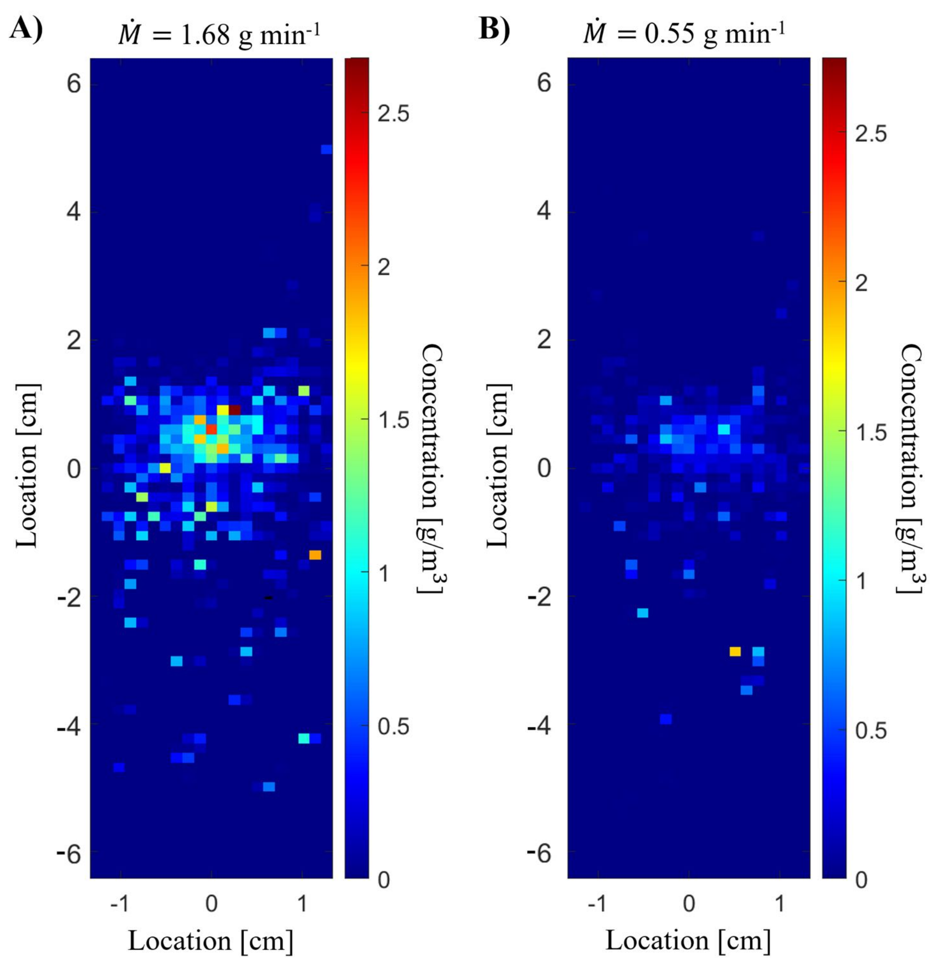

Figure 4.10: The data from two, one-minute composite images are examined. The data in (A) are taken from run 1, a high loading dataset and the data in (B) are taken from run 2, a low loading dataset. We notice that while the two images are not drastically different structurally, the magnitude of the local concentrations correspond to the respective particle mass flow rates.

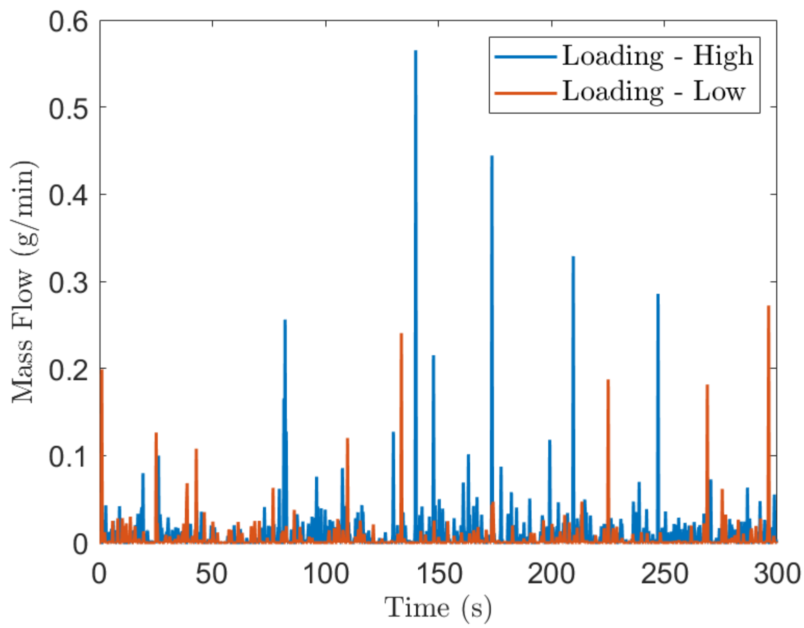

Figure 4.11: Observing time resolved data shows that the particle delivery system introduces sand to the engine at an unsteady rate. For this experiment, this unsteadiness is due to the rotation rate of a helix which draws sand from the hopper into the flow.

a five-minute snapshot of the particles ingested during testing and are made of 1200 subsequent images taken at a 0.25 second interval. As expected, the overall magnitude of mass flow is greater for the high particle loading case. The most notable discovery however, is that the sand delivery is not steady. Instead, we see the loading is cyclic. This unsteadiness is due to the design of the delivery system used for this test. As discussed in section 4.3.2, the sand delivery system used for these tests utilizes a rotating helix to deliver sand from the hopper unit to the bulk flow. The helix rotates at a predetermined rate which varies with input from the user based on the desired test condition. Therefore, the cyclic delivery of sand particles in the frames is directly proportional to the frequency with which the helix rotates. Additionally, the magnitude of the delivery is also highly variable with large portions of the overall mass flow occurring in short bursts. These spikes in mass flow may come from an abnormally high percentage of large particles in the flow due to a heterogeneous distribution of particles within the hopper. In future tests, the ability to directly interpret time resolved data may allow for shorter duration testing and lead to life extension of test engines.

4.6 Conclusions

In this work, a framework is presented for characterising the particle distribution at the inlet of a gas turbine engine under particle ingestion conditions. The method's ability to accurately estimate the mass flow and number density of particles ingested was demonstrated on a test engine inlet at two different mass loading conditions. A known quantity of particle mass flow is supplied as an input to the method for an initial testing configuration. This known quantity is then used to calculate a calibration constant for subsequent data sets where total mass flow rate of particulates is varied. The estimated quantities match the expected values within reasonable uncertainty over a range of operating conditions.

The only hardware required by this technique are a light source and imaging camera. Because of this relative simplicity, the technique is adaptable to any engine inlet geometry, and is less susceptible to measurement error due to engine vibrations and harsh conditions as compared to similar instruments. Additionally, the method is not only limited to an inlet section and may be deployed in any engine region where access can be gained. The authors expect this may be of particular interest to researchers and engine manufacturers alike. The primary findings from these investigations are as follows:

1. The developed technique has demonstrated effective particle mass flow and number density estimates at a range of mass loading conditions.
2. Qualitative analysis concluded that a small percentage of particles have a tendency to bounce along the bottom of the test section. This may provide researchers with more accurate initial conditions for simulations and can provide critical information about particle flow paths.
3. Time resolved data may inform particle flow unsteadiness.
4. Time averaged data provides a broad perspective of particle distribution over the entire region of interest.
5. The minimal footprint of the technique along with the relatively precise estimation of parameters of interest make ParVIS an attractive measurement tool when more sophisticated techniques are not feasible or necessary.

As previously discussed in section 4.3.3, the unrestricted realizability of this method lies in its deployment to a total cross section. This was attempted for the presented experiment but the data obtained with these images were not of archival quality. For this reason, the focus of future investigations will be to demonstrate this capability on an operating engine. Additionally, as mentioned in Section 4.5.2 future work will focus on the characterization and mitigation of scattering intensity error related to particle size and aspect ratio distributions. Lastly, the presented data were gathered at the inlet of a gas turbine engine using a coarse test dust, MIL E-5007C (C-Spec). Future investigations will validate the methodology using additional materials of interest to include ISO Arizona Road Dust and AFRL test dust.

Acknowledgements

The authors would like to thank Britt Antous for her contribution to image collection and test setup. Additional thanks is given to Mr. John Gillespie for his intellectual insight throughout the development of the data processing scheme.

Funding

This work was supported by the United States Office of Naval Research under award numbers N00014-20-1-2538 and N00014-21-1-2397.

References

[1] C. A. Neal, T. J. Casadevall, T. P. Miller, J. W. Hendley II, and P. H. Stauffer, "Volcanic ash-danger to aircraft in the north pacific," US Geological Survey,, Tech. Rep., 1997.

[2] R. C. Daw, "Aviation accident final report," Washington D.C., Tech. Rep., 1992.

[3] E. Miller, "Volcanic ash warning for pilots," in *34th Aerospace Sciences Meeting and Exhibit*, 1996, p. 140.

[4] K. Brun, M. Nored, and R. Kurz, "Particle transport analysis of sand ingestion in gas turbine engines," vol. 134, no. 1, 2012, Journal Article.

[5] W. Chen and L. Zhao, "Review–volcanic ash and its influence on aircraft engine components," vol. 99. Elsevier, 2015, pp. 795–803.

[6] R. Whittle, "Fatal crash prompts marines to change osprey flight rules," *Breaking Defense, available at http://breakingdefense. com/2015/07/fatal-crash-prompts-marines-to-change-osprey-flight-rules/(accessed 15 August 2016, 16 July 2015*, 2015.

[7] K. Olshefski, A. Collins, T. Coulon, T. Lowe, and W. Ng, "Development of an anisokinetic particle sampling probe for use in a gas turbine engine compressor." Frontiers, 2022.

[8] J. Potter and R. P. Tatam, "Optical condensation measurement in gas turbine engine inlets," in *Optical Technology in Fluid, Thermal, and Combustion Flow III*, vol. 3172. SPIE, 1997, pp. 422–433.

[9] R. Litchford, F. Sun, J. Few, and J. Lewis, "Optical measurement of gas turbine engine soot particle effluents," 1998.

[10] M. G. Dunn, "Operation of gas turbine engines in an environment contaminated with volcanic ash," *Journal of Turbomachinery*, vol. 134, no. 5, 2012.

[11] W. Tabakoff, "Study of single-stage axial flow compressor performance deterioration," *Wear*, vol. 119, no. 1, pp. 51–61, 1987.

[12] G. Warwick, "Nasa's ash trials: Engine survives, provides insight," 2015.

[13] J. Bird and W. Grabe, *Humidity effects on gas turbine performance*. American Society of Mechanical Engineers, 1991, vol. 78996.

[14] J. Kim, M. Dunn, A. Baran, D. Wade, and E. Tremba, "Deposition of volcanic materials in the hot sections of two gas turbine engines," 1993.

[15] A. Hamed, W. Tabakoff, and R. Wenglarz, "Erosion and deposition in turbomachinery," vol. 22, no. 2, 2006, pp. 350–360.

[16] G. Grant and W. Tabakoff, "Erosion prediction in turbomachinery resulting from environmental solid particles," *Journal of Aircraft*, vol. 12, no. 5, pp. 471–478, 1975.

[17] W. Tabakoff and A. Hamed, "Aerodynamic effects on erosion in turbomachinery," Cincinnati Univ Ohio, Tech. Rep., 1977.

[18] W. Tabakoff and B. Vittal, "High temperature erosion study of inco 600 metal," *Wear*, vol. 86, no. 1, pp. 89–99, 1983.

[19] W. Tabakoff, "Turbomachinery performance deterioration exposed to solid particulates environment," 1984.

[20] ——, "High temperature erosion resistance of coatings for use in gas turbine engines," *Surface and coatings technology*, vol. 52, no. 1, pp. 65–79, 1992.

[21] W. Tabakoff and V. Shanov, "Erosion rate testing at high temperature for turbomachinery use," *Surface and Coatings Technology*, vol. 76, pp. 75–80, 1995.

[22] W. Tabakoff, "Erosion resistance of superalloys and different coatings exposed to particulate flows at high temperature," *Surface and Coatings technology*, vol. 120, pp. 542–547, 1999.

[23] M. G. Dunn, A. J. Baran, and J. Miatech, "Operation of gas turbine engines in volcanic ash clouds," 1996.

[24] R. J. Clarkson, E. J. E. Majewicz, and P. Mack, "A re-evaluation of the 2010 quantitative understanding of the effects volcanic ash has on gas turbine engines," vol. 230, no. 12, 2016,

Journal Article, pp. 2274–2291.

[25] G. Papadopoulos, D. Bivolaru, and J. Lin, "Real time gas turbine engine particulate ingestion sensor for particle size and composition," in *Turbo Expo: Power for Land, Sea, and Air*, vol. 51128. American Society of Mechanical Engineers, 2018, p. V006T05A029.

[26] C. Y. Moon, A. Panda, G. Byun, C. F. Smith, and K. T. Lowe, "Non-intrusive optical measurements of gas turbine engine inlet condensation using machine learning," vol. 32, no. 4. IOP Publishing, 2021, p. 044001.

[27] C. Y. Moon, C. Edwards, G. Byun, and K. T. Lowe, "Particle characterization using optical measurements and neural networks," vol. 34, no. 3. IOP Publishing, nov 2022, p. 035202. [Online]. Available: https://dx.doi.org/10.1088/1361-6501/aca423

[28] D. Baumgardner, H. Jonsson, W. Dawson, D. O'Connor, and R. Newton, "The cloud, aerosol and precipitation spectrometer: a new instrument for cloud investigations," vol. 59. Elsevier, 2001, pp. 251–264.

[29] W. E. Steiner, S. J. Klopsch, W. A. English, B. H. Clowers, and H. H. Hill, "Detection of a chemical warfare agent simulant in various aerosol matrixes by ion mobility time-of-flight mass spectrometry," vol. 77, no. 15. ACS Publications, 2005, pp. 4792–4799.

[30] K. D. Froyd, D. M. Murphy, C. A. Brock, P. Campuzano-Jost, J. E. Dibb, J.-L. Jimenez, A. Kupc, A. M. Middlebrook, G. P. Schill, K. L. Thornhill *et al.*, "A new method to quantify mineral dust and other aerosol species from aircraft platforms using single-particle mass spectrometry," vol. 12, no. 11. Copernicus Publications Göttingen, Germany, 2019, pp. 6209–6239.

[31] P. H. McMurry, "A review of atmospheric aerosol measurements," vol. 34, no. 12-14. Elsevier, 2000, pp. 1959–1999.

[32] S. Sankar, K. Maher, D. Robart, and W. Bachalo, "Rapid characterization of fuel atomizers using an optical patternator," 1999.

[33] A. P. Kulkarni, V. D. Chaudhari, S. R. Bhadange, and D. Deshmukh, "Planar drop-sizing and liquid volume fraction measurements of airblast spray in cross-flow using slipi-based techniques," *International Journal of Heat and Fluid Flow*, vol. 80, p. 108501, 2019.

[34] R. K. Hanson, "Combustion diagnostics: planar imaging techniques," in *Symposium (International) on Combustion*, vol. 21, no. 1. Elsevier, 1988, pp. 1677–1691.

[35] E. Berrocal, E. Kristensson, M. Richter, M. Linne, and M. Aldén, "Application of structured illumination for multiple scattering suppression in planar laser imaging of dense sprays," *Optics express*, vol. 16, no. 22, pp. 17 870–17 881, 2008.

[36] E. Kristensson, E. Berrocal, M. Richter, S.-G. Pettersson, and M. Aldén, "High-speed struc-

tured planar laser illumination for contrast improvement of two-phase flow images," *Optics letters*, vol. 33, no. 23, pp. 2752–2754, 2008.

[37] E. Kristensson and G. Kristensson, "Physical explanation of the slipi technique by the large scatterer approximation of the rte," *Journal of Quantitative Spectroscopy and Radiative Transfer*, vol. 189, pp. 112–125, 2017.

[38] A. Gaigalas, L. Wang, and S. Choquette, "Measurement of scattering and absorption cross sections of microspheres for wavelengths between 240 nm and 800 nm," *Journal of Research of the National Institute of Standards and Technology*, vol. 118, p. 1, 2013.

[39] D. D. Evanoff and G. Chumanov, "Size-controlled synthesis of nanoparticles. 2. measurement of extinction, scattering, and absorption cross sections," *The Journal of Physical Chemistry B*, vol. 108, no. 37, pp. 13 957–13 962, 2004.

[40] X. Yu, Y. Shi, T. Wang, and X. Sun, "Dust-concentration measurement based on mie scattering of a laser beam," *PLoS One*, vol. 12, no. 8, p. e0181575, 2017.

[41] I. Yeaton, P. Maisto, and K. Lowe, "Time resolved filtered rayleigh scattering for temperature and density measurements," in *28th Aerodynamic Measurement Technology, Ground Testing, and Flight Testing Conference including the Aerospace T&E Days Forum*, 2012, p. 3200.

[42] A. Y. Varaksin, *Turbulent particle-laden gas flows*. Springer, 2007.

[43] C. Y. Moon, A. Gargiulo, G. Byun, and K. T. Lowe, "Non-spherical particle size estimation using supervised machine learning," *Applied Optics*, vol. 59, no. 10, pp. 3237–3245, 2020.

[44] A. Macke, M. I. Mishchenko, K. Muinonen, and B. E. Carlson, "Scattering of light by large nonspherical particles: ray-tracing approximation versus t-matrix method," *Optics Letters*, vol. 20, no. 19, pp. 1934–1936, 1995.

[45] A. S. Collins, "Development of a novel probe for engine ingestion sampling in parallel with initial developments of a high-speed particle-laden jet," Ph.D. dissertation, Virginia Tech, 2021.

[46] T. Vlach, K. Olshefski, D. Bunin, A. Ehlers, M. Caddick, T. Lowe, and W. Ng, "Analysis of c-spec particle breakage in a turbine engine particle ingestion test cell," in *Proceedings of the ASME Turbo Expo 2023: Turbomachinery Technical Conference and Exposition*, 2023.

[47] N. Otsu, "A threshold selection method from gray-level histograms," vol. 9, no. 1. IEEE, 1979, pp. 62–66.

[48] R. Moffat, "Contributions to the theory of single-sample uncertainty analysis," 1982.

[49] "Emva 1288 imaging performance," http://softwareservices.flir.com/BFS-U3-31 S4-BD2/latest/EMVA/EMVA.html, accessed: 2023-01-30.

[50] R. Clarkson, "Volcanic ash and aviation–rolls-royce position, may 2017 [www. wmo. int],"

2017.

5. Development of an Anisokinetic Particle Sampling Probe for Use in a Gas Turbine Engine Compressor

The contents of this chapter have been published in *Frontiers in Mechanical Engineering* (**Olshefski, K.**, Collins, A., Coulon, T., Lowe, T., Ng, W. (2022) "Development of an Anisokinetic Particle Sampling Probe for Use in a Gas Turbine Engine Compressor", *Front. Mech. Eng.* 8:951986. doi:10.3389/fmech.2022.951986)

Abstract

Sand and dust particle ingestion is an inevitability for aircraft operating in arid environments. For conventional takeoff and landing aircraft, significant dust can be ingested into the gas turbine powerplant. Helicopters and vertical takeoff and landing (VTOL) aircraft are at especially high risk due to their tendency to blow significant debris into the air during takeoff and landing operations. The present study highlights the development of an anisokinetic particle sampling probe for use in aircraft engines to obtain real-time measurement of ingested particles often present in these harsh environments. Offtake of particles during engine operation in dusty conditions will provide researchers with an improved understanding of particle breakage tendency and component erosion susceptibility. Three foundational studies were conducted to establish a baseline understanding of probe performance: an aerodynamic study, a particle tracking study, and a particle sampling study. These studies were performed using the Free Jet rig at the Advanced Propulsion and Power Laboratory at Virginia Tech. Particles as large as 1.3 mm were sampled at Mach numbers where $M = (0.25, 0.70)$ and yaw angles ranging from 0° to 45° relative to freestream, conditions not previously investigated. Results indicate that the probe operates sub-isokinetically throughout the full range of test conditions and that probe aerodynamic capture efficiency is inversely proportional to both Mach number and yaw angle. However, this efficiency limitation does not notably influence the sampling probe's ability to capture the test dust of interest. While the presence of the probe in the flow does result in an airflow velocity reduction of up to 55%, due to their relatively large Stokes numbers the particles of interest only experience a decrease of roughly 5%. These results indicate that this probe is capable of providing researchers with valuable particle size and shape information through effective particle sampling at particle sizes ($100\mu m \leq d_p \leq 1300\mu m$) and speeds ($M \geq 0.25$) not previously investigated.

5.1 Introduction

Solid particulate ingestion while operating in harsh environments has been shown to hinder the performance of gas turbine engines. The source of these particulates can vary from ash to sand to dust. In severe cases, ingestion of particles can be the main cause of temporary engine flameout and possible permanent engine failure. A flameout is an instance where the flame in the combustion chamber of a jet engine has been extinguished, resulting in a total loss of power [1, 2]. For conventional takeoff and landing aircraft, significant dust can be ingested into the gas turbine powerplant. As a key historical example, a Lockheed L-100 aircraft encountered two engine failures and two temporary engine flameouts while flying over Mount St. Helens after a volcanic eruption [3]. All four engines showed signs of melted dust in the turbine section and severe abrasion in the compressor section. In December 1989, the volcanic eruption of Mt. Redoubt sent ash clouds more than 30,000 feet into the atmosphere [4]. Operating in nearby Anchorage, a KLM Royal Dutch Airlines Boeing 747-400 equipped with four General Electric CF6-80C2 engines inadvertently entered the ash cloud and experienced a four engine flameout causing the flight crew to make an emergency landing [5]. All four engines from the aircraft were replaced, costing the airline over 80 million dollars in replacements and repairs [6]. Helicopters and vertical takeoff and landing (VTOL) aircraft are at especially high-risk due to their tendency to blow significant debris into the air during takeoff and landing operations. This is a continuing concern for US Naval operations. In 2015, an MV-22 Osprey crashed during a training exercise in Hawaii, claiming the lives of two US Marines and injuring twenty other personnel [7]. The cause of the fatal crash was attributed to dust ingestion resulting in an engine failure.

There currently exists a limited understanding of how ingested particles traverse engines after entering the inlet section. Researchers are interested in investigating the behavior of sand particles as they traverse an aircraft engine compressor. To this end, a particle sampling probe is under continued development and initial analysis has been conducted using a high-speed free jet laden with particles. In subsequent studies, this probe will be installed in the compressor section of an engine operating in a particle-laden environment. This environment governs design considerations for the sampling probe. The anisokinetic particle sampling probe designed for this study is capable of effectively capturing highly poly-dispersed test dust MIL E-5007C at speeds where $M = (0.25, 0.70)$ and at yaw angles $\theta \leq 45°$. Additionally, efforts have been made to determine the time-averaged particle concentration from these samples. The work contained herein is presented as follows: Section 5.2 outlines the materials and facilities used during the investigation, Section 5.3 details the three experimental campaigns and, Section 5.4 presents the results of these experiments and discusses their implications. Finally, Section 5.5 provides conclusions which can be drawn from these findings.

5.2 Methods

5.2.1 Probe Design and Construction

The design of this probe is constrained by factors of the environment where the probe will be operating. Of primary concern is the confined space of the compressor where the probe will be installed. Researchers at Virginia Tech have recently commissioned an engine test stand facility which is specifically designed to study sand ingestion. The test stand operates a Rolls-Royce M250-C20B turboshaft engine. The particle sampling probe will be installed within a stator row of the engine's six-stage axial compressor. This region limits the size of the sampling probe. Prior particle sampling probe configurations would not be suitable for this geometry as typical geometries may be as large as six inches in the streamwise length [8–10]. Material selection is also an important consideration for this work. While a material such as steel or titanium may have strength characteristics for withstanding the forces of high-speed flow, a probe dislodging event would have disastrous consequences. For this reason, the probe was constructed from polycarbonate tubing, bent at $90°$, and fitted with a steel collar for additional support. Figure 7.1A shows the developed probe next to an early prototype. The internal diameter of the probe is 2 mm, the external diameter of the probe is 4 mm, and the axial length of the probe is approximately 20 mm as shown by Figure 7.1B. Lastly, it is well known that a sharp edge is preferred for particle sampling probes [11–13]. To achieve this and increase the capture area, the sampling probe is given an internal chamfer rather than a more traditional external chamfer. This increases the effective capture area of the probe while maintaining a sharp tip. During the development process, researchers modified the probe design from an internal chamfer angle (ψ) of 45° to 30° to reduce the likelihood of particle ejection from the probe after impact. Therefore, additional aerodynamic studies were conducted to compare the performance of each configuration.

5.2.2 Particles

Characterization

For particles suspended in flow, a primary metric of characterization is the particle Stokes number where

$$St = \frac{\tau_p}{\tau_f} \tag{5.1}$$

and τ_p is the momentum response time of a particle and the characteristic time scale of the carrier phase is τ_f. The particle response time is defined as

$$\tau_p = \frac{\rho_p d_p^2}{18\mu_f C} \tag{5.2}$$

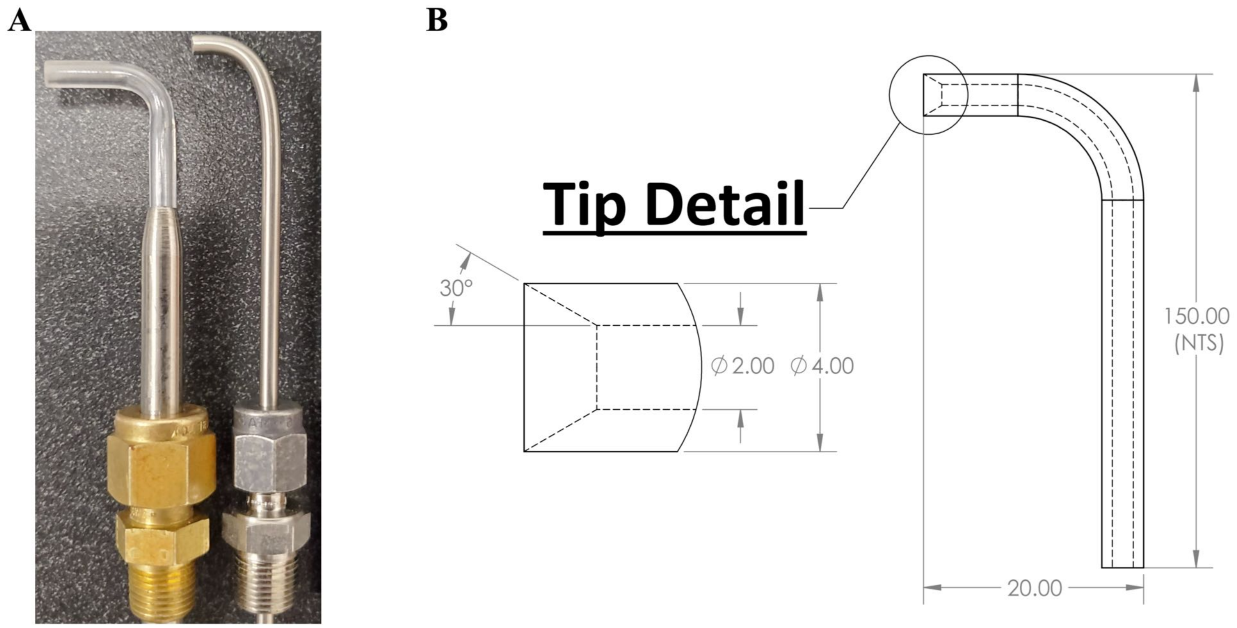

Figure 5.1: Sampling probe (left) placed next to early steel prototype (A) and probe dimensions in mm (B).

where ρ_p is the particle density, d_p is the particle diameter, μ_f is the dynamic viscosity of the fluid, and C is the non-Stokesian correction factor

$$C = \begin{cases} 1 + Re_p^{2/3}/6 & \text{at} \quad Re_p \leq 10^3 \\ 0.11 Re_\mathrm{p}/6 & \text{at} \quad Re_p > 10^3 \end{cases} . \tag{5.3}$$

The particle Reynolds number, Re_p is

$$Re_p = \frac{\rho_p |u - v| d_p}{\mu_f}, \tag{5.4}$$

and $|u - v|$ is the relative velocity of the particle with respect to the fluid [14]. We define the characteristic timescale of the flow as

$$\tau_f = \frac{D_s}{U_B} \tag{5.5}$$

where U_B is the bulk velocity of the jet, and D_s is the probe outer diameter. This definition of Stokes number assumes the particle is spherical but is the standard definition used in relevant literature [14, 15].

Glass Microspheres

During these studies two ranges of glass microspheres were used to assess the baseline performance of the sampling probe. These particles were selected with two purposes: providing an experimental control by limiting particle size to a small range of diameters, and ensuring consistent particle behavior through uniform shape distribution. Glass microspheres were chosen for their regular shape and tight size distribution at nominal diameters of 3-6 μm and 65-75 μm. We will refer to the 3-6 μm spheres as small spheres and the 65-75 μm as large spheres moving forward. By collecting samples of the glass microspheres, researchers are able to study fundamental probe behavior and eliminate uncertainties that would otherwise arise from highly poly-dispersed size and shape characteristics of typical test dusts. The batches of small and large spheres are characterized by the particle size distribution (PSD) graphs in Figures 5.2A and 5.2B. The microscopic images of microspheres in Figures 5.3A and 5.3B display the uniformity of the samples. This uniformity is contrasted in Figure 5.3C which shows the diversity of shapes and sizes seen in the test dust (C-Spec) sample. Researchers found that the particles are prone to clumping due to ambient moisture absorption. Therefore, samples were dried in an oven 24 hours before being used in jet studies. Using the above analysis, the small glass spheres are found to have a Stokes number of $St = 3.5$ at $M = 0.25$ and $St = 9.75$ for $M = 0.70$. The large glass spheres were found to have $St = 842$ where $M = 0.25$ and $St = 2357$ for $M = 0.70$. This analysis assumes no slip exists between the particles and the flow. In reality, some slip will occur and will result in a reduced Stokes number. This estimate is therefore taken as a limiting case.

Particle Analysis

Particle size and shape measurements are conducted using a Microtrac CAMSIZER X2. The CAMSIZER X2 is rated to measure particles ranging in size from 0.8 μm to 8 mm. The system utilizes dual cameras to illuminate a particle flow path. Then, an LED stroboscopic light source and two high-resolution cameras capture photos which are then evaluated in real-time to provide particle information. The key feature of this particular model, which makes it ideal for the current research, is its use of Dynamic Image Analysis (DIA). With this feature the unit employs two cameras of different magnifications to make measurements of a wide range of particle sizes without compromising accuracy. From the Microtrac and included software, researchers can determine the various particle shape coefficients and particle size distribution of a given sample.

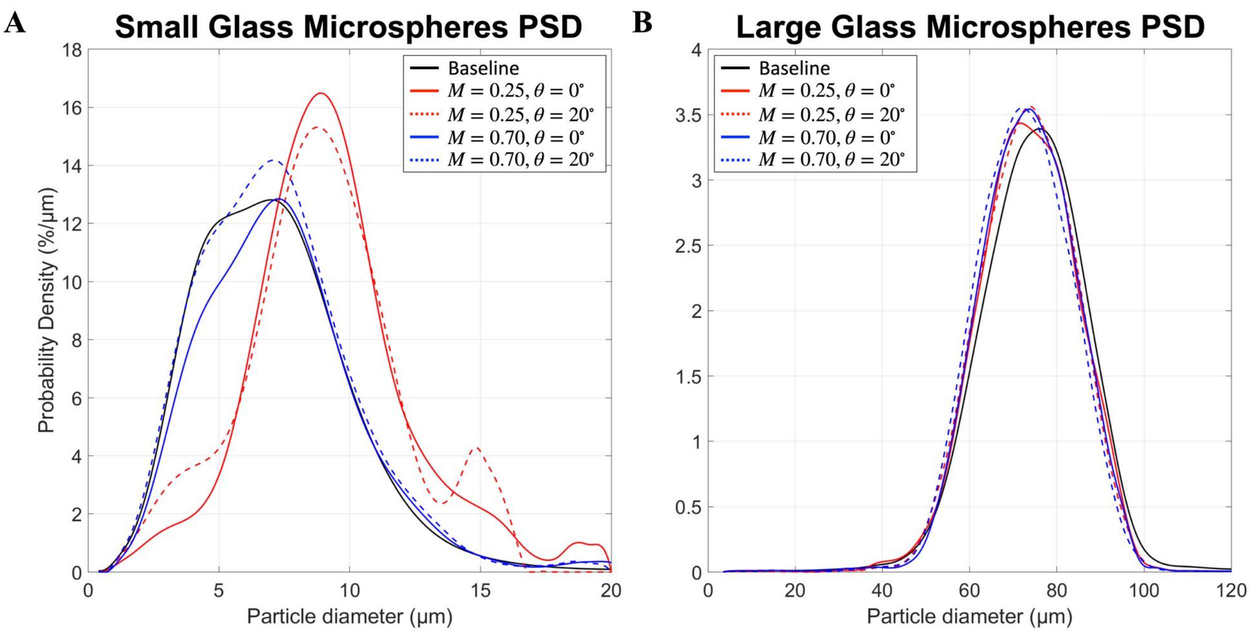

Figure 5.2: Glass microsphere particle size distributions (PSD) for small microspheres (A) and large microspheres (B).

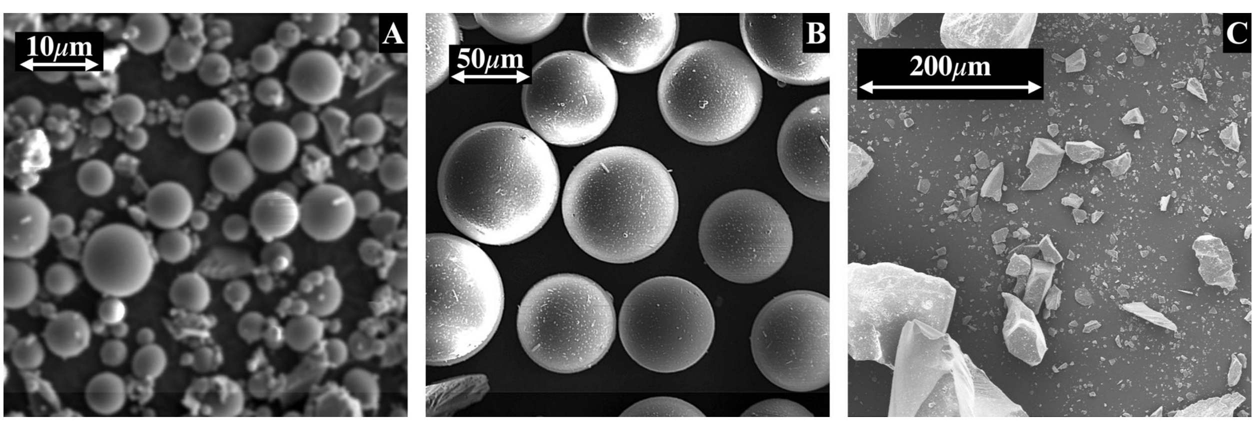

Figure 5.3: Detailed imagery of small glass spheres (A), large glass spheres (B), and C-Spec sand (C).

C-Spec Sand

The medium of interest for engine tests is test dust MIL E-5007C, commonly referred to as C-Spec, which is a commercially available crushed quartz mixture. The material is chosen for its wide particle size distribution which is representative of dusts encountered by aircraft. Particle sizes of C-Spec range from 50-1300 μm. Particle size distribution is provided by the manufacturer on a mass basis with 50% of particles larger than 200 μm and 3% of particles smaller than 75 μm. Therefore, conducting a Stokes analysis using equation 7.1 provides that particles which are smaller than 2.5μm can be expected to fall within the Stokesian regime at velocities corresponding to $M = 0.25$ and particles which are 1.5μm or smaller will remain Stokesian at $M = 0.70$. This accounts for less than 1% of particles of interest. Instead, average size particles (250μm) will experience Stokes numbers ranging from $850 \leq St \leq 1170$ where $0.25 \leq M \leq 0.70$, which is considerably higher than ranges explored by previous studies and indicates that particle inertia is significant relative to the forces acting on them by the surrounding fluid.

Constituent Testing

Material analysis conducted by the Virginia Tech Petrology Lab utilized X-ray diffraction to determine the relative constituents of each particle variety. They found that the C-Spec sample is over 99% quartz and less than 1% microcline. Being almost entirely quartz, the density of C-Spec is assumed to be 2650 kg/m^3. The glass microspheres are composed completely of soda-lime-silica, with a density of 2500 kg/m^3. While the particles in this research are largely silica-based, this is not a requirement for the sampling probe as it is also capable of sampling a wide range of particle types. For example, AFRL-03, which has large quantities of non-silica constituents such as gypsum and dolomite, should be sampled with similar performance [16].

5.2.3 Facilities

Virginia Tech Free Jet Rig

The data obtained for all investigations was collected using the Free Jet rig at the Advanced Propulsion and Power Laboratory (APPL) at Virginia Tech seen in Figure 5.4A. The jet uses facility compressed air supply to accelerate flow through various nozzle configurations to reach desired flow conditions. Flow enters the assembly through impinging jets and passes through a mixing section with a diameter of 200 mm before being reduced down to 100 mm. The flow progresses through several screens and honeycomb structures which condition the flow. For these studies, test particles were then seeded into the flow in a plenum section and accelerated out of a 50.8 mm diameter converging nozzle as shown in Figure 5.5. The rig is controlled using a National Instruments cDAQ-9184 chassis and Scanivalve Corp. ZOC17IP/8x-APC pressure transducer which provides pressure measurements for flow condition calculations. As seen in Figure 5.4B, the particle sampling probe is placed directly downstream of the Free Jet nozzle exit at the jet centerline. Additional information about the Virginia Tech Free Jet can be found in [17, 18].

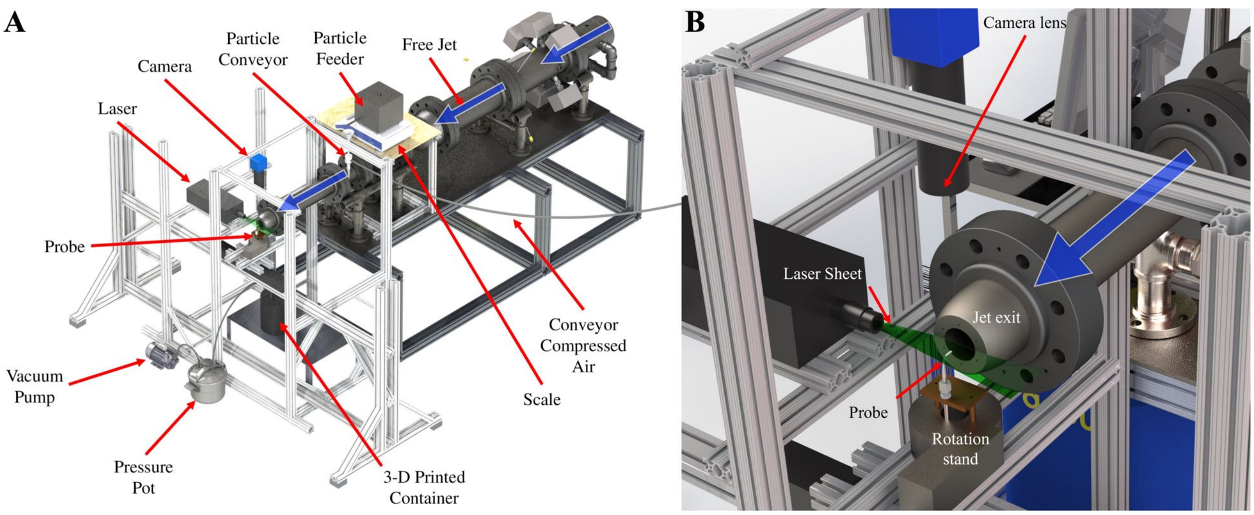

Figure 5.4: Virginia Tech Free Jet rig (A) and detailed perspective of probe experiment setup (B).

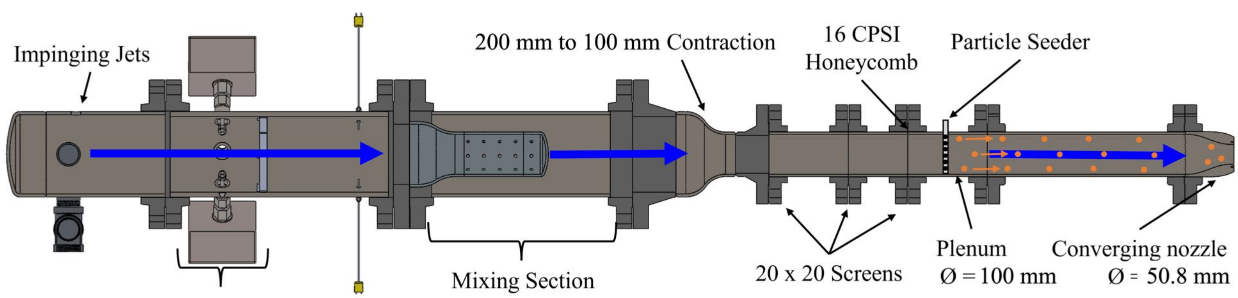

Figure 5.5: Detailed section view of the Virginia Tech Free Jet.

Rotating Mount

For these studies, the probe was positioned using a Velmex rotation stage which ensured the consistent axial location of the probe face and rotated the probe to a desired yaw angle. The stand was used to rotate the probe at various yaw angles with respect to the flow streamwise direction and was modified so that the probe would rotate about the probe tip, so the location of the probe inlet would not change with respect to the jet. The modification on the rotation stage also allows the probe to be moved up and down by loosening a compression fitting to accomodate sampling at various radial locations. We define the non-dimensional radial location as the ratio of position (r) and jet outer radius (r_0) where

$$R = \frac{r}{r_0}. \tag{5.6}$$

For tests where suction pressure was applied to the probe, a vacuum pump and intermediate plenum were positioned downstream of a particle sampling container as described in Section 5.2.3.

Particle Seeding

Two different seeding apparatuses were used, one for seeding Di-Ethyl-Hexyl-Sebacate (DEHS) oil particles used for flow field measurements with particle image velocimetry (PIV), and another for seeding C-Spec particles and glass spheres for the particle tracking velocimetry (PTV) study and concentration sampling experiment. These DEHS particles are commonly used in PIV studies as they aerosolize to diameters less than 1 μm, which is ideally suited for this application [19].

For the PTV and concentration sampling experiment, an AccuRate particle feeder was used to provide a constant flow of particles into the jet. The particle feeder sits atop a Fristaden Lab scale, and the weight of the feeder is recorded before and after each run to calculate the mass of sand which was introduced to the jet during the run. This was done to ensure a consistent feed rate throughout all tests. The feeder and scale are secured to a platform above the jet plenum. The feeder has a hopper that is filled with particles, and a rotating helix transports the sand from the bottom of the hopper through a nozzle where particles exit. At its maximum setting, the particle feeder can introduce C-Spec particles at approximately 10 g/min. Upon exiting the sand feeder nozzle, the particles fall into a small funnel which leads into an Exair Line Vac pneumatic particle conveyor. The Line Vac works as follows:

1. Facility compressed air is driven through an inlet section into an annular plenum chamber.
2. The flow is directed into the throat through focused nozzles.
3. The resulting jet creates a vacuum near the intake of the conveyor section.
4. The vacuum draws in particles which are then carried through the seeder and into the jet.

The Line Vac creates a vacuum of -29.9 kPa given a supply pressure of 552 kPa. This vacuum pressure was found to be sufficient to force particles into the jet without backflow. Particles enter the jet through the seeder, which is inserted into an orifice in the side of the free jet plenum. The seeder is a tube with seventeen 2.5 mm holes along one side to accomodate particle dispersion. The tube is oriented with the holes facing upstream to maximize mixing of the particles with the airflow. The particle feeder, conveyor, and seeder are all used in conjunction with the free jet to supply a particle laden jet flow to the sampling probe.

Sample Containment

Researchers required that particle samples be contained and stored for further analysis without any particle loss, whether to the suction source or from bouncing out of the sampling container. To this end, a sample containment system was developed and is shown in Figure 5.6. Anti-static tubing was connected to the bottom of the sampling probe, leading to a collection jar. To create a negative pressure environment, the jar was placed inside of a 3-D printed black cylindrical container. The lid of this container has two holes, one through which the tubing could connect from the probe to the jar, and another with tubing leading to a suction source. The suction source consisted of a vacuum pump and plenum (pressure pot), with the vacuum pressure in the plenum reaching about -50 kPa. To prevent particles from escaping the jar, the jar's lid was kept on, but two holes were created in the jar lid, one for the particle tubing, and the other for air to escape to the suction source, with the second hole of the jar lid being covered with a 20μm paper filter to prevent particles from escaping. The 3-D printed container made it easy to see if particles had escaped the jar, being easily visible if strewn about the black container.

5.3 Experimental Procedures

5.3.1 Probe Aerodynamic Studies

The primary metric used to evaluate the aerodynamic performance of the probe is the aspiration efficiency (A_e) described as

$$A_e = \frac{A_0}{A_s} \tag{5.7}$$

where A_s is the frontal projected area of the probe and A_0 is the area of the undisturbed streamtube. This ratio provides insight into the probe's ability to sample small particles with $St < 1$. The probe operating under the sub-isokinetic regime results in $A_e < 1$. Here, streamlines will diverge near the probe inlet, causing Stokesian particles to be undersampled. Conversely, the probe operating under super-isokinetic conditions results in $A_e > 1$, which means the streamlines will converge near the probe inlet, causing smaller particles to be oversampled. The aerodynamic characteristics of the

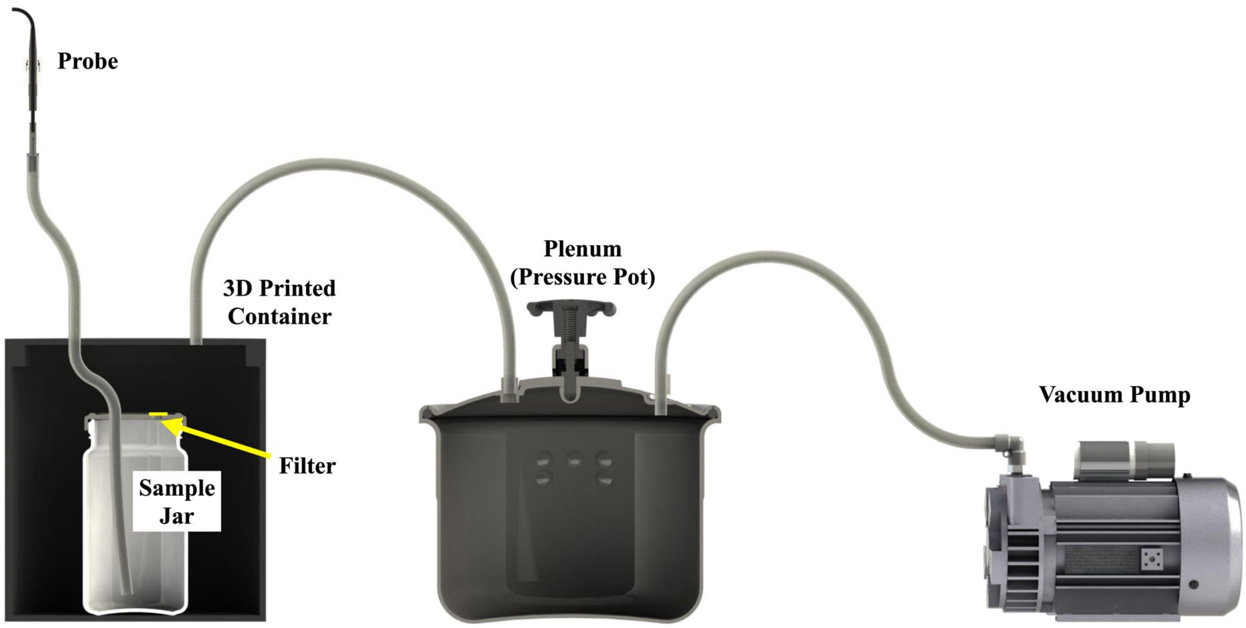

Figure 5.6: Particle containment system.

sampling probe were assessed through planar, two-component PIV measurements conducted in the previously described Free Jet rig. The jet was brought to the desired flow rate and atomized DEHS oil particles were seeded into the jet using a Laskin nozzle. This nozzle uses shear forces to atomize the DEHS oil into droplets with a nominal diameter of less than a micron [20]. The shearing process in the Laskin nozzle plenum was controlled using compressed nitrogen at 415 kPa for Mach 0.25 flows and 485 kPa for Mach 0.70 flows. Next, an EverGreen[2] dual, pulsed, frequency-doubled Nd:YAG laser with up to 200 mJ output at 532 nm wavelength was formed into a sheet intersecting the sampling probe as shown in Figure 5.4B and pulsed at a predetermined interval. A LaVision Imager sCMOS CLHS camera, positioned above the probe and facing downward, then took an image for each pulse, and created image pairs of subsequent images. These image pairs were then analyzed using LaVision DaVis 8.4 software. After initial processing within DaVis, velocity field data was exported to MATLAB where the non-physical data was removed and the time-averaged velocity field was constructed with the remaining data. This time-averaged data was then used by a separate MATLAB script to compute velocity streamlines as seen in Figures 5.7- 5.9, which were in turn used to calculate the stream tube from the far-field to the probe face. This streamtube can then be used to calculate probe aspiration efficiency. There were two general conditions present in these experiments: 1) unaltered probe exit and 2) probe exit under an induced suction of -50 kPa. The objective of these studies was to quantify the aerodynamics near the probe tip. The suction case

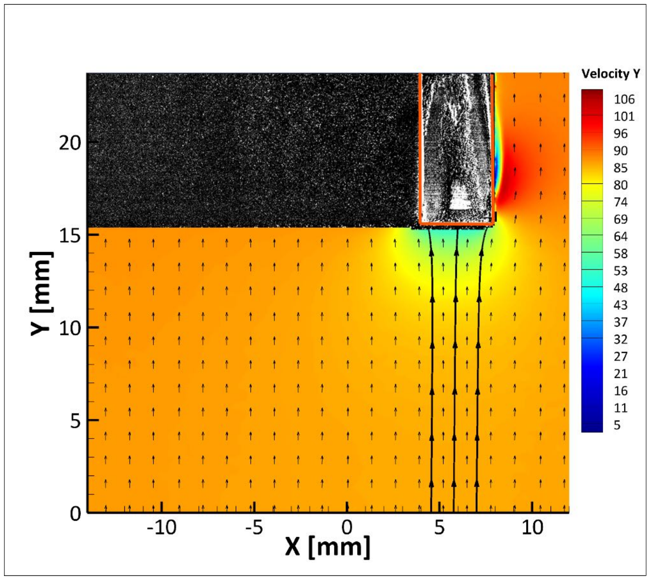

Figure 5.7: Axial velocity contours (m/s) with vector field and streamtube overlaid on image of probe to show approximate location for the $M = 0.25$,$\theta = 0°$ test case. Sampling probe boundaries are highlighted in red.

however, provided additional insight by determining whether the sampling efficiency increased by introducing a vacuum at the probe face. Baseline aerodynamic performance was established by evaluating the streamtube area at the probe face and upstream in undisturbed flow, and thus the probe aerodynamic efficiency. Data was acquired at Mach numbers of $M = (0.25, 0.70)$, and at probe yaw angles of $\theta = (0°, 20°, 45°)$. These Mach numbers correspond to nominal jet bulk velocities of $U_B = 85$ m/s and 240 m/s, respectively. For each case of Mach number and yaw angle, 1000 image pairs were taken. A third study was conducted using the same methodology with the finalized probe geometry and sampling apparatus. Here, the probe was aspirated with the same vacuum pressure and results were compared to the previous cases.

PIV Data Processing

The image pairs taken during the PIV experiment were processed in the PIV software, LaVision DaVis 8.4, which calculates a velocity vector field for each image pair by observing the mean displacement of DEHS particles over all locations in the frame and using a specified time separation, dt. The velocity vectors were not calculated in the area on the opposite side of the probe from the laser due to the laser's inability to fully penetrate through the polycarbonate probe. The vector fields calculated for all image pairs were then averaged, yielding one vector field of averaged velocities. Next, to remove non-physical velocities, which were likely a result of the DaVis software,

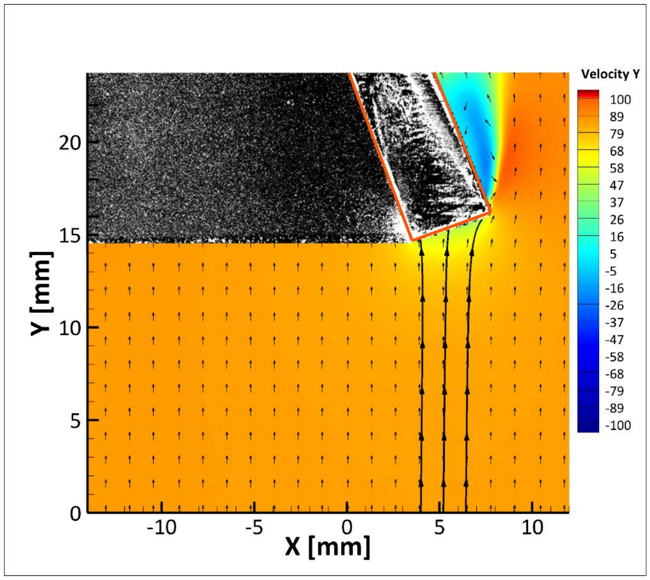

Figure 5.8: Axial velocity contours (m/s) with vector field and streamtube overlaid on image of probe to show approximate location for the $M = 0.25$,$\theta = 20°$ test case. Sampling probe boundaries are highlighted in red.

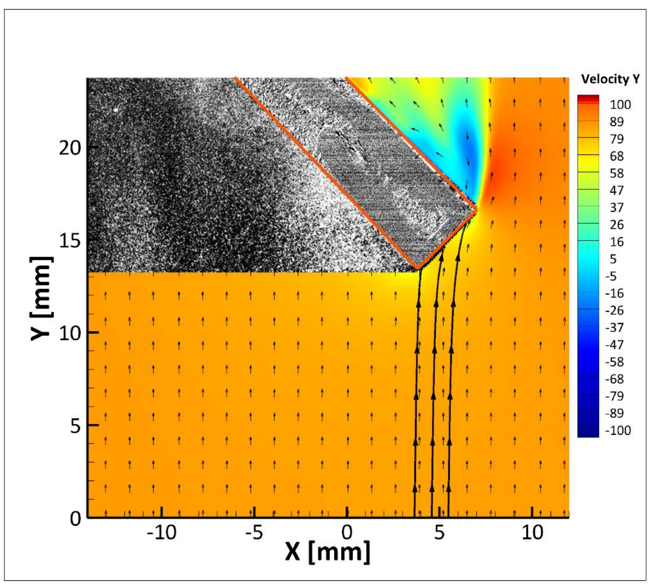

Figure 5.9: Axial velocity contours (m/s) with vector field and streamtube overlaid on image of probe to show approximate location for the $M = 0.25$,$\theta = 45°$ test case. Sampling probe boundaries are highlighted in red.

MATLAB code was used to select locations in the average velocity field, plot all instantaneous data used to calculate the average data at those locations on a streamwise versus spanwise coordinate plot, and remove outlier data. The resulting average velocity data was then imported into separate MATLAB code, which plotted streamlines using the velocity vector field. These streamlines then were used to calculate the area ratio of the probe.

5.3.2 Particle Tracking Study

The setup for the particle tracking study which investigated the effects of the sampling probe on particle trajectories was nearly identical to the probe aerodynamic study. However, for the particle tracking study, the jet was seeded with C-Spec sand in place of the DEHS. The laser and camera were then used to take 1000 image pairs for later processing. Particle velocity data was determined using PTVlab, a MATLAB add-on software [21]. A total of 50 composite image pairs was created using the original 1000 image pairs. The PTVlab software then processed each composite image pair and calculated individual particle velocity data. The final result was a list of particle position, velocity vector magnitude, and particle velocity angle relative to freestream. This study was conducted at Mach number M =0.70 and yaw angle θ =0°.

5.3.3 Particle Concentration Studies

Three particle concentration studies were conducted. The first two studies aimed at investigating particle sampling bias using the well-defined glass microspheres. Here, the glass bead particles were seeded into the free jet and captured by the sampling probe. Both the small glass spheres and the large glass spheres were tested separately to determine whether either distribution would be over- or under-sampled by the sampling probe. The experiment again followed the previously described testing conditions. The particles were sent directly to the Microtrac analyzer to minimize potential for losses resulting from post-test analysis methods. The analyzer provided size distributions for the particles sampled by the probe. By comparing the previously established size distribution to the sampled distribution, conclusions about the probe's ability to sample the various particle types were drawn.

The third study assessed the concentration of C-Spec as sampled by the sampling probe. This was conducted at two jet locations, at jet centerline ($R = 0$), and halfway between centerline and the bottom of the jet ($R = 0.5$). Before each run, a new jar with its own unmodified lid was weighed using an Adam Equipment LTB 2602E scale, and the weight was recorded. The lid was removed, the jar was placed in the 3-D printed container, and the custom filtered jar lid screwed on. With the 3-D printed container closed and the jar secure, the suction source was activated, and the free jet was run to the desired Mach number. Then, C-Spec was seeded to the free jet, and a timer was started. Particles were captured by the probe for a period of fifteen minutes. For the case where $M = 0.70, \theta = 0°$, 1000 image pairs were taken using the laser and camera for later PTV processing. At the end of the time period, the particle feeder was stopped, the free jet was turned off, and suction was deactivated. To ensure there were no residual particles in the probe or line leading to the jar, compressed air was blown into the probe inlet, pushing any remaining particles into the jar. The 3-D printed container was then opened and the custom filtered lid removed from the jar. The jar's original unmodified lid was screwed back on, and the jar was weighed. The difference in weight was the weight of particles collected by the probe. This process was repeated for all cases of Mach number, yaw angle, and probe location. To supplement the concentration sampling study, another series of runs was completed to measure the air volumetric flowrate through the probe. A Kelly Pneumatics digital flowmeter was used to measure the volumetric flowrate for all cases of Mach number and yaw angle. This volumetric flowrate would later be used to calculate particle concentration.

Particle concentration was calculated as

$$C_m = \frac{\dot{m}}{\dot{V}} \tag{5.8}$$

where $\dot{m}$ is rate of mass captured over time by the probe, $\dot{V}$ is the air volumetric flowrate in the probe, and C_m is the measured concentration. For this study, $\dot{m}$ was calculated using

$$\dot{m} = \frac{m}{\Delta t} \tag{5.9}$$

where m is the total mass accumulated by the probe, and Δt is the time elapsed. For these studies, Δt remained a constant fifteen minutes. Volumetric flowrate was measured using the previously described flowmeter in a separate experiment and corrected for the conditions at the time of the concentration study. This corrected flowrate ($\dot{V}$) was determined as

$$\dot{V} = \dot{V}_m \sqrt{\frac{P_a T_m}{P_m T_a}} \tag{5.10}$$

where P_m, T_m, and $\dot{V}_m$ are the ambient pressure and temperature and, measured volumetric flowrate found during the separate flowmeter test, respectively. The ambient pressure and temperature conditions during particle sampling are P_a and T_a, respectively.

The researchers chose to calculate an idealized concentration assuming isokinetic conditions. In this hypothetical scenario, an ideal probe volumetric flowrate is found by assuming the velocity of the air entering the probe is the same as the velocity of the air exiting the free jet. This ideal flowrate ($\dot{V}_i$) was calculated as

$$\dot{V}_i = U_B A_s \tag{5.11}$$

where U_B is taken as the jet exit velocity and A_s is the probe frontal area. The probe frontal area is based on an inlet diameter of 4 mm. Although the probe inner diameter is 2 mm, the 30° internal chamfer creates an effective capture diameter equal to the probe outer diameter, and it is assumed that all C-Spec particles entering the chamfered area are captured. Additionally, frontal area was taken to be the projected inlet area for cases of non-zero yaw angle. The idealized concentration value is then calculated as

$$C_i = C_m \frac{\dot{V}}{\dot{V}_i} \tag{5.12}$$

and is the primary metric used to assess the accuracy of the concentration measured by the sampling probe. In theory, this idealized concentration should exactly match the true particle concentration of the flow. However, additional investigation may be required to assess the uncertainty associated with assuming the capture diameter is equal to the frontal area as there is potential for particle rebound after interacting with the probe chamfer.

5.3.4 Measurement Uncertainty

An uncertainty analysis was performed to assess the precision of the reported results. Overall uncertainty was calculated using a root-sum-square of individual uncertainty contributions as

$$\delta R = \left\{ \left(\frac{\partial R}{\partial x_1} \delta x_1 \right)^2 + \left(\frac{\partial R}{\partial x_2} \delta x_2 \right)^2 + \ldots \left(\frac{\partial R}{\partial x_N} \delta x_N \right)^2 \right\}^{1/2} \tag{5.13}$$

where δR is the absolute uncertainty and $(\partial R / \partial x_i)\, \delta x_i$ are the individual contributions [22]. For all data, engineering judgement was used to account for major sources of uncertainty. Additional sources of ambiguity were determined to be either negligible or outside of the scope of the current investigation.

Aerodynamic Analysis

The primary metric used to assess probe aerodynamic capture efficiency was the aspiration ratio (A_e) found in equation 7.6. To determine the areas used to calculate this ratio, the upstream streamtube diameter was manually selected using the streamline plotting program. The chosen diameter is directly related to the aspriation ratio as

$$A_e = \frac{A_0}{A_s} = \frac{d_0^2}{4r_s^2 cos\theta} \tag{5.14}$$

where the projected area at the probe face, A_s, assumes a major radius equal to the probe outer radius (r_s) and a minor radius which is the projection of r_s onto a plane at angle θ. The diameter, d_0, is the diameter which is manually selected and it is assumed that the area calculated with this measurement is circular. This selection relied on visual inspection and should therefore be considered a primary source of uncertainty. As such, the uncertainty of the upstream diameter was chosen to be ± 0.1 mm. For any streamtube diameter value selected in this range, the plotted streamlines would still have aligned reasonably well with the probe inlet. With these assumptions a maximum uncertainty value was found to be $\delta A_e = \pm 0.017$. While additional uncertainty may be present in the LaVision DaVis 8.4 software, providing an estimate of this uncertainty as it relates to streamtube diameter was deemed to be beyond the scope of this work.

Particle Tracking

The primary source of uncertainty associated with the particle tracking study was found to be converting pixel displacement to velocity. Conversion is calculated as

$$|\vec{v}| = \phi |\vec{p}| \tag{5.15}$$

where $|\vec{v}|$ is velocity magnitude, $|\vec{p}|$ is the pixel displacement magnitude, and ϕ is the calibration factor. The calibration factor was determined by manually drawing a straight line with a known representative physical distance on an image and counting the equivalent pixel length of the line. The reference distance used was that of the probe diameter, known to be 4 mm. However, manually drawing this line left the opportunity for ambiguity in the calibration. Had the line been a few pixels longer or shorter, the probe dimension would still have been adequately represented. Because of this, the calibration uncertainty was assumed to be ± 0.05 m/s per pixel. Calibration could have reasonably fallen within this range depending on the manner in which the line was drawn. Again, it is reasonable to assume additional uncertainty would be present from the PTVlab software but, estimating this falls outside of this study.

Particle Sampling

For the particle sampling and concentration study, primary sources of uncertainty included the instrument uncertainty of the scale used for measuring the mass accumulated by the probe (m) and the instrument uncertainty of the flowmeter used to determine the volumetric flow rate inside the sampling probe ($\dot{V}_m$). Manufacturers of both instruments provide measurement uncertainty estimates. The uncertainty of the scale was assumed to be ± 0.02 g and the uncertainty of the flowmeter was taken to be $\pm 8.87 \times 10^{-6}$ m^3/s [23, 24]. With these assumptions a maximum uncertainty of measured concentration was found to be $\delta C_m = \pm 2.3 \times 10^{-4}$ kg/m^3. Other possible sources of uncertainty, such as those associated with particle residue inside of the sampling probe were more difficult to quantify and were not included in this analysis.

5.4 Results and Discussion

The results of the previously described experiments are discussed below. The aerodynamic study explored the influence of placing the particle sampling probe within the flow downstream of the jet exit. Similarly, the particle tracking study looked at the change in the behavior of the particles as they approached and entered the sampling probe. Lastly, the particle sampling studies analyzed particle sampling bias, the effectiveness of the sampling container assembly, and estimated particle concentration from the flow. From these results, an extensive understanding of probe performance was established.

5.4.1 Probe Aerodynamic Analysis

Table 5.1 provides the resulting aspiration ratios from the PIV studies. Here we see that the ratio in every case was less than unity, indicating sub-isokinetic sampling across all flow scenarios. This is due to the higher pressure at the probe tip than in the freestream as confirmed in Figures 5.7-5.9. Sub-isokinetic conditions indicate that the probe can be expected to undersample only the smallest of C-Spec particles which are fractions of a micron in diameter and have $St < 1$. From these results it is evident that the addition of aspiration suction increases probe efficiency. This increase is most notable in the lower Mach number cases where an efficiency of more than 75% is observed. In the higher Mach number case, however, this efficiency increase is limited to a maximum of 12.5%. Comparing the study of the 30° chamfered probe to that of the 45°, a decrease in area ratio is observed. This can most likely be explained by the addition of the particle collection apparatus, which may cause the probe tip to feel less suction from the vacuum pump and pressure plenum, causing the static pressure at the probe tip to be higher than in the previous study. The area ratio decreases as the yaw angle increases, indicating that the probe is sensitive to changes in flow angle. For the finalized probe geometry, increasing the yaw angle from $\theta = 0°$ to $\theta = 20°$ results in a 17% reduction in aspirational efficiency. Further increasing yaw angle from $\theta = 20°$ to $\theta = 45°$ results in a 29% reduction at $M = 0.25$ and a 45% reduction at $M = 0.70$. This is in part due to the decrease in probe inlet projected area with increasing yaw angle. This implies that abrupt changes in flow direction near the probe tip will cause further undersampling of small C-Spec particles. However, as previously stated, C-Spec particles experiencing Stokesian behavior are expected to be a negligibly small proportion of all particles encountering the sampling probe. Probe aerodynamic efficiency decreases as the Mach number increases across all studies.

ψ	Aspiration	M	θ	A_e
45°	Atmospheric	0.25	0°	0.38
			20°	0.37
		0.70	0°	0.48
			20°	0.47
45°	Suction	0.25	0°	0.67
			20°	0.66
		0.70	0°	0.54
			20°	0.52
30°		0.25	0°	0.49
			20°	0.42
			45°	0.30
		0.70	0°	0.42
			20°	0.36
			45°	0.20

Table 5.1: Aerodynamic study aspiration ratio results

5.4.2 Particle Tracking Study

The list of particle locations and velocity vector information was split into two data sets for analysis: all particles in frame, and particles only within the probe capture area. Figures 5.10A and 5.10B show all the velocity vectors in each data set. The purpose of the first data set was to characterize the overall movement of the C-Spec particles, whereas the purpose of the second data set was to characterize the behavior of C-Spec particles approaching the probe inlet. First, the

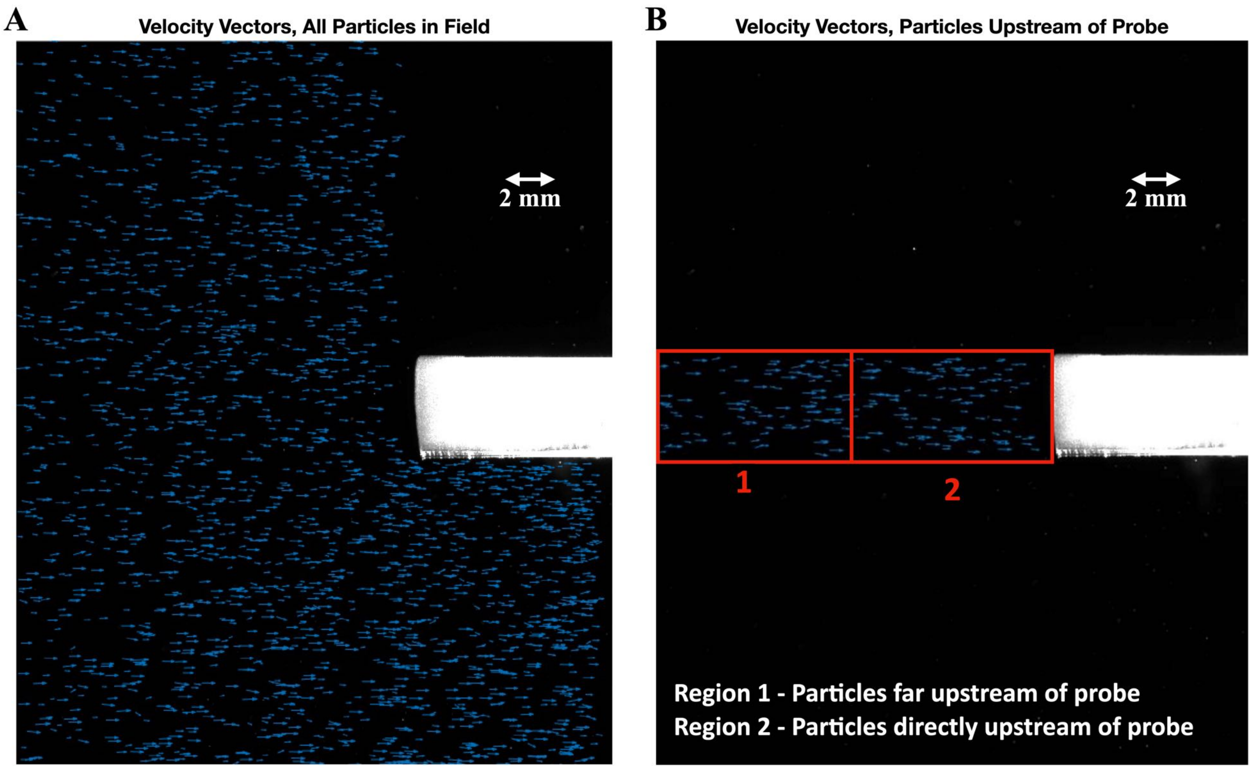

Figure 5.10: Particle velocity vectors for full field (A) and for regions far upstream (1) and directly upstream (2) of sampling probe (B)

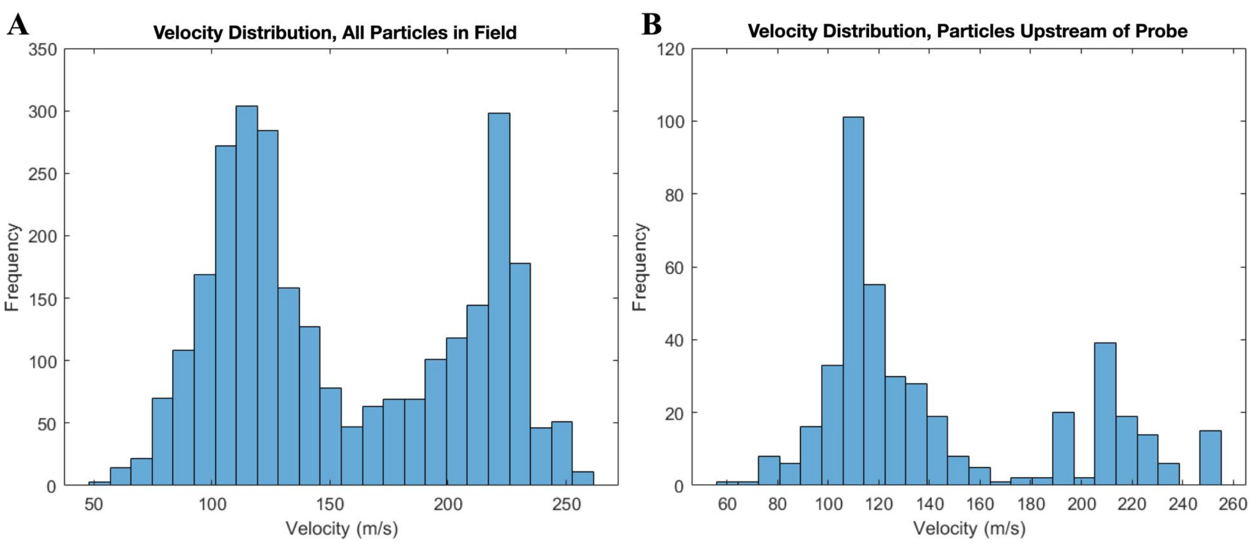

Figure 5.11: Particle velocity distribution profiles from PTV results for full field (A) and for regions far upstream (1) and directly upstream (2) of sampling probe (B)

distribution of the velocity magnitudes was analyzed for both data sets as seen in Figure 5.11A and Figure 5.11B. For both data sets, the velocity distribution was found to be bimodal, with peaks around 120 m/s and 220 m/s. The bimodal nature of the distribution can be explained by a slightly bimodal diameter distribution discovered during the initial particle size investigation. For the data set of all particles in the window, a mean velocity of 155.0 m/s was calculated with a minimum value of 54.1 m/s and a maximum value of 261.6 m/s found. For the data set constrained to particles in the probe path, a mean velocity of 143.8 m/s was found with a minimum value of 58.8 m/s and a maximum value of 253.1 m/s calculated.

Both velocity distributions appear to be biased towards slower velocities, with the first apex of the bimodal curve being larger than the second. At first glance, this is counterintuitive when compared to the bimodal diameter distributions, which is biased towards small particles. However, this discrepancy is likely caused by the higher detectability of larger particles by the laser and camera as well as the relative ease with which the PTV software can calculate velocities for these particles.

Next, the distribution of the velocity vector directions for both data sets was analyzed. The vector direction was taken as the angle relative to the streamwise direction. In both cases, the mean angle relative to the streamwise direction is less than 2°. This means, on average, the C-Spec particles are coming straight out of the free jet with no directional bias. However, the distribution ranges from -30° to 30°. By observation, the distribution is random and not dependent on location. One explanation for this randomness of directions is particles bouncing off the inner wall of the free jet plenum or nozzle, a phenomenon that will certainly occur when the probe is placed in an engine.

Finally, the data confined to the probe flow path was analyzed to determine whether the particle velocities were influenced by the aerodynamic changes that occur near the probe tip. To do this, the data was broken into two regions of equal area, one containing particles far from the probe and the other containing particles close to the probe. Figure 5.11B shows how the data was divided. The average velocity was found for each region and compared. The average velocity in region 1 and region 2 was found to be 149.5 m/s and 141.6 m/s, respectively. That is a decrease of only 5.3% from the average velocities reported previously. For comparison, based on PIV results, the airflow experiences a 55% decrease in velocity from the freestream to the probe inlet. This is sufficient to conclude that the velocities for the overwhelming majority of C-Spec particles are not heavily affected by aerodynamic changes induced by the probe. This conclusion also agrees with the Stokes number analysis.

5.4.3 Particle Sampling Studies

As described in Section 5.2.2 a particle bias analysis was conducted by using the sampling probe to capture glass microspheres and deliver them directly to the CAMSIZER particle analyzer. The captured distributions compared to baseline are shown in Figure 5.2. The result reconfirms those predicted by the aerodynamic study where we learned that the probe operates sub-isokinetically, and a Stokes number analysis suggests that particles with diameters less than 10μm may be affected by the streamlines near the probe face. The large spheres sampled match the distribution of the baseline very well. With these findings, the authors conclude that the material of interest (C-Spec) should remain unaffected by the diverging streamlines at the sampling probe face as nearly all particles are larger than 10μm.

Sending the particles directly to the machine for analysis contains the sample in the analyzer and makes subsequent inquiry impossible. Therefore, to assess the sampling characteristics of C-Spec and the local particle concentration of the flow, the particle sampling apparatus was developed. Then, a concentration study was conducted where the sampling probe captured C-Spec particles as described in Section 5.3.3. Two types of concentration were calculated for each test case, one calculated using the volumetric flowrate measured from the probe by the digital flowmeter, referred to as measured concentration (C_m). A separate concentration was calculated using an ideal volumetric flowrate assuming the probe operated isokinetically, referred to as ideal concentration (C_i). Ideal concentration was chosen as the primary metric to compare the different test cases because it more accurately represents the true concentration in the airflow. The sub-isokinetic conditions experienced by the probe causing the measured volumetric flowrate to be much lower than it would be in isokinetic conditions. This also makes the measured concentration higher than the true concentration. Another consideration is that the majority of C-Spec particles have $St > 1$ and will not be affected by changes in airflow near the probe tip.

The results given in Table 5.2 show the effect of changing individual variables: Mach number, yaw angle, and probe radial location. For each variable examined, all results are compared with the baseline case of $M = 0.70$, probe at yaw angle $\theta = 0^\circ$, and probe location at the center of the jet exit area ($R = 0$). The results show an inversely proportional relationship between calculated concentration and Mach number. This makes intuitive sense, as the higher velocity will cause the particles to be spaced further apart as they are seeded into the free jet. Interestingly, total weight accumulated was higher for Mach 0.70 than for Mach 0.25. The authors believe this is due to a difference in particle distribution about the free jet cross-sectional area at the different Mach numbers. This proportionality also holds for increasing yaw angle and is consistent with a projected area analysis. However, the decrease in concentration was steeper than the decrease in projected area. Particle bouncing is a likely culprit for this discrepancy, as it is easier for particles to bounce off of the inner wall and out of the probe at higher yaw angles. Lastly, to determine the bias of particles distributed throughout the free jet, a measurement was taken at a radial location directly between jet centerline and the lower outer radius ($R = 0.5$). Here, the concentration was found to be lower than at the centerline location. This is inconsistent with a qualitative jet exit spatial distribution analysis performed which concluded that the spatial distribution was biased towards the bottom due to the gravitational effect on large C-Spec particles (detailed results not shown here). Therefore, the authors concluded that additional research needs to be done on understanding and controlling the spatial distribution of the particles within the test rig.

Jet Radial Location (R)	M	θ	m [g]	C_m[kg/m^3]	C_i[kg/m^3]
0.0	0.25	0°	1.17	0.0038	0.0012
	0.70	0°	1.52	0.0036	0.0006
		20°	1.20	0.0028	0.0005
		45°	0.63	0.0016	0.0003
0.5		0°	0.84	0.0020	0.0003

Table 5.2: Concentration study results

5.5 Conclusions

An anisokinetic sampling probe is under continued development for use in an operational turboshaft engine compressor. Three preliminary studies were conducted to gain a baseline understanding of the sampling probe's performance. During these studies, the developed probe was placed directly downstream of a free jet. First, an aerodynamic analysis was conducted using particle image velocimetry techniques and probe isokinetic efficiency was determined at various Mach numbers ($M = 0.25, 0.70$), yaw angles relative to freestream ($\theta = 0°, 20°, 45°$), and ambient as well as aspirated suction conditions. Next, a particle dynamic analysis was conducted whereby the free jet was seeded with particulates (small and large glass microspheres) and probe sampling bias was determined for the range of particle sizes. Then, the jet was seeded with C-Spec sand particles and particle tracking velocimetry techniques investigated particle behavior due to the influence of the probe in the flow path. Lastly, sampling concentration was calculated using flow parameters and sampled particulate mass. The primary findings from these investigations are as follows:

1. The developed probe has demonstrated effective particle sampling at particle sizes (100 μm$\leq$

$d_p \leq 1300$ μm) and speeds (M $\geq$0.25) not previously investigated.

2. The sampling probe operates sub-isokinetically for all relevant flow scenarios as determined by the aerodynamic analysis.
3. Probe aerodynamic efficiency (A_e) is inversely proportional to freestream Mach number (M) and yaw angle (θ). However, this efficiency limitation does not notably influence the sampling probe's ability to capture the test dust of interest.
4. There appears to be no trajectory modification of C-Spec particles due to the presence of the sampling probe in the flow.
5. Although airflow velocity is markedly reduced near the probe tip, particle velocities remain constant through probe interaction.
6. Calculation of concentration remains inconclusive at this time and requires additional investigation.

Conflict of Interest Statement

The authors declare that the research was conducted in the absence of any commercial or financial relationships that could be construed as a potential conflict of interest.

Author Contributions

AC, and TC contributed to conception, design, and execution of the study. KO was responsible for formal analysis, validation, and preparation of the manuscript. KO, AC, and TC wrote sections of the manuscript. TL and WN supervised the project and contributed to manuscript review and editing. All authors contributed to manuscript revision, read, and approved the submitted version.

Funding

This work was supported by the United States Office of Naval Research under award numbers N00014-20-1-2538 and N00014-21-1-2397.

Acknowledgments

The authors would like to thank Alix Ehlers and Dr. Mark Caddick of the Virginia Tech Petrology Lab for their assistance in classifying the particulates used for this study. Additional thanks is given to Dr. Loren Crook and Mr. James Loebig of Rolls-Royce North American Technologies Inc. for their many insightful contributions to the program.

References

[1] J. Chambers, "The 1982 encounter of british airways 747 with the mt. galuggung eruption cloud," *AIAA paper*, no. 85-0097, 1985.

[2] E. E. Campbell, "Recommended flight-crew procedures if volcanic ash is encountered," in *Volcanic Ash and Aviation Safety: Proceedings on the First International Symposium of Volcanic Ash and Aviation Safety*, vol. 2047. US Geological Survey Bull, 1994, pp. 151–157.

[3] H. Mitchell and F. Gilmore, "Dust-cloud effects on aircraft engines: emerging issues and new damage mechanisms," *Paper No. RDA-TR-120012-001*, 1982.

[4] C. A. Neal, T. J. Casadevall, T. P. Miller, J. W. Hendley II, and P. H. Stauffer, "Volcanic ash-danger to aircraft in the north pacific," US Geological Survey,, Tech. Rep., 1997.

[5] R. C. Daw, "Aviation accident final report," Washington D.C., Tech. Rep., 1992.

[6] E. Miller, "Volcanic ash warning for pilots," in *34th Aerospace Sciences Meeting and Exhibit*, 1996, p. 140.

[7] R. Whittle, "Fatal crash prompts marines to change osprey flight rules," *Breaking Defense, available at http://breakingdefense. com/2015/07/fatal-crash-prompts-marines-to-change-osprey-flight-rules/(accessed 15 August 2016, 16 July 2015*, 2015.

[8] N.-G. Heo, J.-H. Lim, J.-W. Lee, J.-S. Lee, S.-J. Yook, and K.-H. Ahn, "Development of a sampling probe for representative sampling of pm at freestream velocities in the range from 0 to 300 km h1," *Journal of Atmospheric and Oceanic Technology*, vol. 35, no. 4, pp. 727–738, 2018.

[9] N.-G. Heo, S.-H. Woo, J.-H. Lim, S.-J. Yook, and K.-H. Ahn, "Investigation of a double shrouded probe for particle sampling in high velocity airflows," *Advanced Powder Technology*, vol. 29, no. 5, pp. 1085–1091, 2018.

[10] C. Briones, Bichal, "Aspiration efficiencies of a soot-particulate sampling probe with dilution under gas turbine conditions," *AIAA*, 2008.

[11] A. Whiteley and L. Reed, “The effect of probe shape on the accuracy of sampling flue gases for dust content,” *J. Inst. Fuel*, vol. 32, p. 316, 1959.

[12] I. Davis, “Sampling probes for duct and stack sampling in: Acgih, editor,” *Air sampling instruments for evaluation of atmospheric contaminants. 4th ed. Cincinnati, Ohio*, pp. L11–L13, 1972.

[13] N. Fuchs, “Sampling of aerosols,” *Atmospheric Environment (1967)*, vol. 9, no. 8, pp. 697–707, 1975.

[14] A. Y. Varaksin, *Turbulent particle-laden gas flows*. Springer, 2007.

[15] C. T. Crowe, *Multiphase flow handbook*. CRC press, 2005.

[16] E. Poursaeidi, A. Mohammadi Niaei, M. Lashgari, and K. Torkashvand, “Experimental studies of erosion and corrosion interaction in an axial compressor first stage rotating blade material,” *Applied Physics A: Materials Science and Processing*, vol. 124, no. 9, 9 2018. [Online]. Available: https://link.springer.com/article/10.1007/s00339-018-2007-5

[17] D. Mayo, K. Daniel, K. Todd Lowe, and W. F. Ng, “Experimental investigation of a heated supersonic jet with total temperature non-uniformity,” *23rd AIAA/CEAS Aeroacoustics Conference, 2017*, no. June, pp. 1–14, 2017.

[18] A. J. Saltzman, K. T. Lowe, and W. F. Ng, “250 khz three-component doppler velocimetry at 32 simultaneous points: a new capability for high speed flows,” *Measurement Science and Technology*, vol. 31, no. 9, p. 095302, 2020.

[19] R. J. Adrian and J. Westerweel, *Particle image velocimetry*. Cambridge university press, 2011, no. 30.

[20] C. Kähler, B. Sammler, and J. Kompenhans, “Generation and control of tracer particles for optical flow investigations in air,” *Experiments in fluids*, vol. 33, no. 6, pp. 736–742, 2002.

[21] W. Brevis, Y. Niño, and G. Jirka, “Integrating cross-correlation and relaxation algorithms for particle tracking velocimetry,” *Experiments in Fluids*, vol. 50, no. 1, pp. 135–147, 2011.

[22] R. Moffat, “Contributions to the theory of single-sample uncertainty analysis,” 1982.

[23] Adam Equipment. (2019) Luna precision balances: Ltb 2602e. https://www.adamequipment.com/ltb-2602e/, [Accessed April 30, 2022].

[24] Kelly Pneumatics. (2021) Digital mass flow sensor. https://kellypneumatics.com/product/digital-mass-flow-sensor/, [Accessed April 30, 2022].

6. Performance Assessment of an Anisokinetic Particle Sampling Probe at the Inlet of a Gas Turbine Engine

6.1 Introduction

This chapter represents a continuation of the research initiated in Chapter 5, wherein the particle sampling probe, as described previously, was installed in the inlet duct of a gas turbine engine upstream of the inlet guide vane section. The present study constitutes the first instance of particle ingestion tests on a functional engine at Virginia Tech. The primary objective of this research is to evaluate the sampling efficacy of the probe in an operational environment, encompassing various complexities of inlet fluid flow and sources of vibration. The researchers seek to address two crucial inquiries concerning the performance of the sampling probe by sampling particles at the inlet plane:

1. Is it possible to establish that the sample collected by the probe matches that of the control sample of the test dust?
2. Can a localized concentration estimate be approximated from the collected sample?

As this chapter is supplementary to the research presented in Chapter 5 and Chapter 7, it is not intended to be exhaustive. Thus, certain details regarding the experimental setup and facility description have been omitted for concision. For a thorough depiction of the engine test facility, the interested reader may refer to Chapter 3; for a complete characterization of the test dust, see Chapter 5; and for a comprehensive account of the particle seeding mechanism, consult Chapter 4.

6.2 Experimental Methods

6.2.1 Experimental Setup

The tests described in this work were performed at the Virginia Tech Particle Ingestion Engine Stand using a Rolls-Royce model M250-C20B engine operating at ground idle condition. This condition resulted in an engine mass flow rate of 0.744 $\mathrm{kg\,s^{-1}}$ and a bulk flow velocity of 64 $\mathrm{m\,s^{-1}}$ as recorded by the test cell data acquisition system. Test dust was introduced into the inlet flow at two conditions, a full loading condition and a half-loading condition, with the former yielding a particle concentration of 45 $\mathrm{mg\,m^{-3}}$ and the latter resulting in 22.5 $\mathrm{mg\,m^{-3}}$. These values were

Engine Condition	$\dot{m}_{M250}$ (kg s^{-1})	Run	Duration (min)	σ_p (mg m^{-3})	Loading Condition
Ground Idle	0.744	1	12:46	Variable	Mixed Loading
		2	26:41	45	High Concentration
		3	13:22	Variable	Mixed Loading
		4	10:10	22.5	Low Concentration

Table 6.1: Engine test conditions given the engine throttle condition, engine air mass flow rate ($\dot{m}_{M250}$), the run number, the duration of the run, the calibrated particle mass concentration (σ_p), and the condition being tested. The variable loading cases were necessitated by a parallel study and may be thought of as unsteady concentration oscillations over the time period.

selected based on prior evidence indicating that exposure at these levels may lead to significant engine deterioration and erosive damage [1]. Four sampling measurements were conducted in total, with two samples taken at mixed loading conditions and one sample taken at each of the described loading conditions from above. This experiment was conducted in parallel with other investigations which necessitated mixed loading conditions. These mixed loading conditions can be described as uneven oscillations in loading concentration over a long span of time. Therefore, it was determined that the data taken durning these runs would not be suitable for analysis when estimating particle concentration measured by the sampling probe. However, due to the length of these runs, significant samples of test dust could be obtained. Therefore, these data are ideal for assessing the particle size distribution collected by the sampling probe. A summary of the testing conditions can be seen in Table 6.1.

The present study focuses on the ingestion and sampling of MIL E-5007C, also referred to as C-Spec, which is a commercially available blend of crushed quartz. This material is known for its extensive range of particle sizes which mimic dust typically found in aircraft operational environments. Particle sizes of C-Spec range between 50-1300 μm. The manufacturer's particle size distribution shows that only 3% of particles are smaller than 75 μm, while 50% of particles are larger than 200 μm on a mass basis [2]. The particle density of C-Spec is assumed to be 2650 $\mathrm{mg\,m^{-3}}$ owing to its near-exclusive composition of quartz.

As shown in Figure 6.1, the particle sampling probe was positioned directly upstream of the M250 engine inlet, concentric to the inlet duct with the probe face normal to the direction of flow. The probe exit is routed, via anti-static tubing, to a two way valve. This valve then diverts the particle-laden flow to one of two sample collection jars placed inside of a plenum chamber. The collection jars are fitted with a 50 μm filter to allow the pressure within the jar to equilibrate with

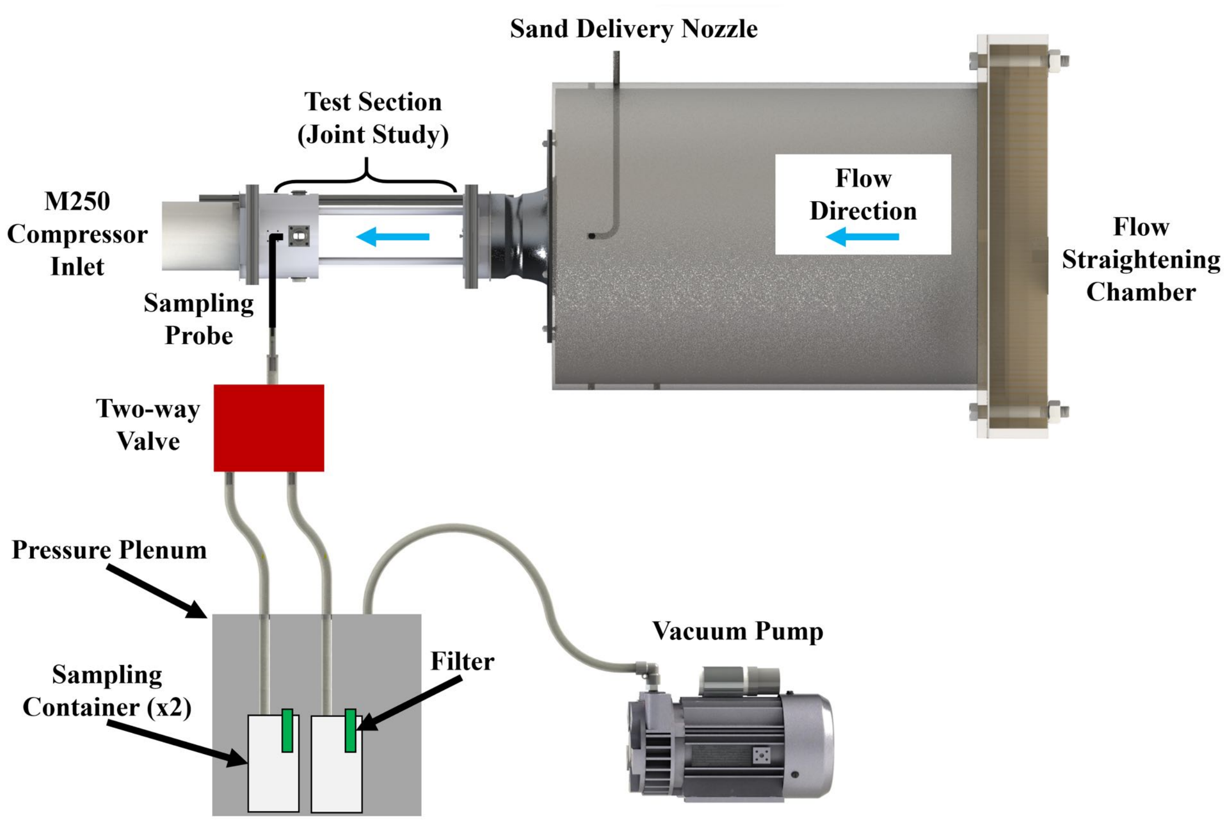

Figure 6.1: Experimental setup schematic showing the approximate location of the sampling probe in relation to the M250 engine while also showing the arrangement of the accompanying sampling apparatus.

that of the plenum while simultaneously ensuring the sample remains in the collection container. A suction pressure is applied to the system using a vacuum pump resulting in a suction pressure at the probe exit of approximately 57.57 kPa (8.35 psi). This setup allows researchers to take two subsequent remote particle measurements, a necessity for sampling during live engine tests. At the conclusion of the engine test, the sampling apparatus is disassembled and all tubing and valves are inspected to ensure no residual particles remain. Finally, the samples are weighed and stored for further analysis. Care was taken to ensure accurate test dust mass measurements were obtained by weighing the individual sampling jars prior to the engine tests. The sample mass is then determined as the accumulated mass from the post-test measurement. All measurements were taken using an Adam Equipment LTB 2602E high precision scale.

6.2.2 Measurement Uncertainty Considerations

To assess the precision of the reported results, an uncertainty analysis was performed. Overall uncertainty was calculated using a root-sum-square of individual uncertainty contributions as

$$\delta R = \left\{ \left(\frac{\partial R}{\partial x_1} \delta x_1 \right)^2 + \left(\frac{\partial R}{\partial x_2} \delta x_2 \right)^2 + \ldots \left(\frac{\partial R}{\partial x_N} \delta x_N \right)^2 \right\}^{1/2} \tag{6.1}$$

where δR is the absolute uncertainty and $(\partial R/\partial x_i)\,\delta x_i$ are the individual contributions [3]. For all data, engineering judgement was used to account for major sources of uncertainty. Additional sources of ambiguity were determined to be either negligible or outside of the scope of the current investigation.As previously stated, there are two primary research objectives for this study: to analyze the collected sample against a control sample of test dust to determine the probe's ability to capture a representative sample, and to determine local concentration using the sampling probe.

Local particle concentration, σ_p, is estimated using the total mass collected by the probe (Δm), the collection time as measured using a stop watch (Δt), and the probe volumetric flow rate as determined using a digital flowmeter as

$$\sigma_p = \frac{\Delta m}{\dot{V}_p \Delta t} \tag{6.2}$$

where $\dot{V}_p$ is the volumetric flow rate through the sampling probe. For this study, primary sources of uncertainty included the instrument uncertainty of the scale used for measuring the mass accumulated by the probe (Δm) and the instrument uncertainty of the flowmeter used to determine the volumetric flow rate inside the sampling probe ($\dot{V}_m$). Manufacturers of both instruments provide measurement uncertainty estimates. The uncertainty of the scale was assumed to be ± 0.02 g and the uncertainty of the flowmeter was taken to be $\pm 8.87 \times 10^{-6}$ m^3/s [4, 5]. With these assumptions a maximum uncertainty of measured concentration was found to be $\delta\sigma_p = \pm 28.2\ \mathrm{mg\,m^{-3}}$. Other possible sources of uncertainty, such as those associated with particle residue inside of the sampling probe were more difficult to quantify and were not included in this analysis.

For sample size analysis, researchers in the Virginia Tech department of Geosciences used microscopy techniques and the image processing software ImageJ to establish particle size and shape characteristics. Figure 6.2 provides an example of what this analysis looks like. To establish particle parameters, the user must manually select the long axis of a random selection of particles using a drawing tool. The software is then calibrated to estimate the approximate length of this

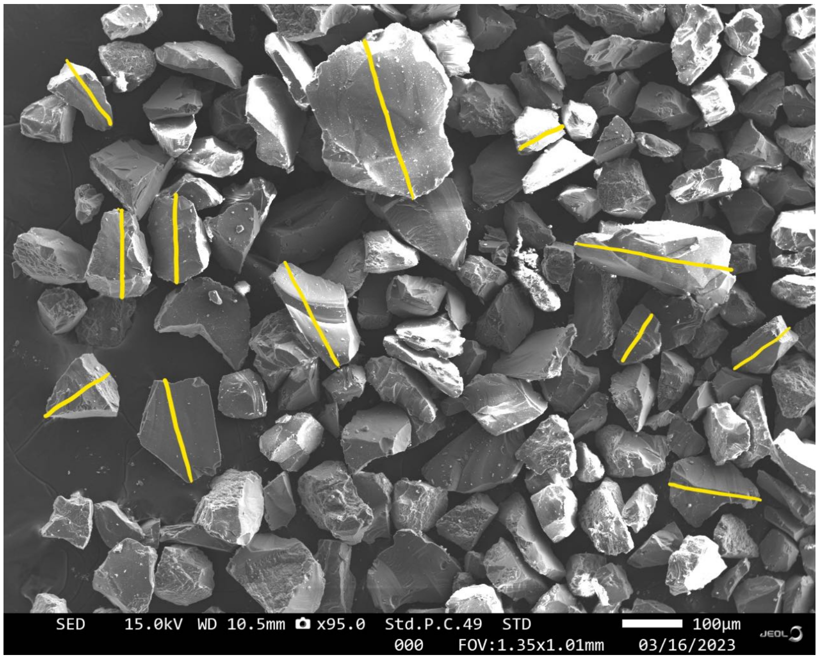

Figure 6.2: Image showing microscopy technique for establishing particle size. The yellow lines shown are manually drawn by the user and processed by the software package to determine particle characteristics.

long axis and subsequent parameters are established with that information. Here, it is clear that some user inconsistency is to be expected. This selection relies on visual inspection and should therefore be considered a primary source of uncertainty. As such, the uncertainty of the long axis length was determined to be $\delta l_p = \pm 5$ μm. For any value selected in this range, the plotted lines would still have provided a reasonable measurement estimate. While additional uncertainty may be present in the ImageJ software, providing an estimate of this uncertainty as it relates to a manually established length was deemed to be beyond the scope of this work. However, it should be noted that user consistency across samples should ensure that any bias or uncertainty is reduced through randomization. Namely, while some of the estimated lengths are shorter or longer than the actual particle length, it is expected that with a sufficiently large data set the influence of this uncertainty is reduced. This is especially relevant when comparing two samples for similarity, rather than relying solely on the absolute size estimate, as is the case with the current study.

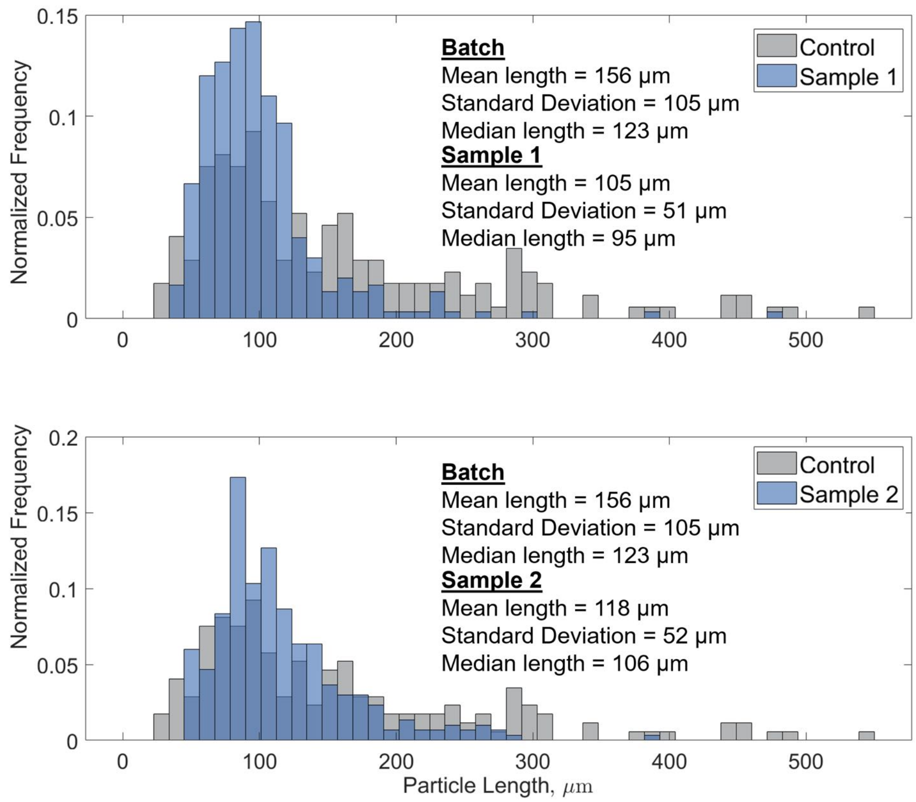

Figure 6.3: Normalized particle size distributions of the two collected dust samples compared to a control sample taken from the same batch.

6.3 Results

6.3.1 Particle Size Distribution

Figure 6.3 shows the normalized particle size distributions for the two collected samples as compared to a control sample of the C-Spec test dust. The Control sample was taken directly from a storage container provided by the manufacturer. The two samples correspond to the respective run numbers. Therefore, Sample 1 was collected from engine test run 1 and Sample 2, run 2. Basic statistical quantities are calculated for each of the samples to include mean and median particle length as well as standard deviation about the mean. The control sample contained particles with a mean length of 156 μm and a standard deviation about the mean of 105 μm. The median length of particles for the control sample was 123 μm. Through inspection of Figure 6.3 it is clear that both of the collected samples appear to have higher percentages of smaller particles than that of the control. This is confirmed with a calculated mean length of 105 μm for Sample 1 and 118 μm for

Sample	Loading Condition	Duration (min)	Collected Mass (mg)	Concentration ($\mathrm{mg\,m^{-3}}$)
1	Mixed Loading	12:46	150	417
2	High Loading	26:41	370	492
3	Mixed Loading	13:22	200	531
4	Low Loading	10:10	70	245

Table 6.2: Engine test conditions and sample concentration estimates

Sample 2. Both standard deviations are also considerably less as well with both sample's standard deviation being roughly half of that of the control. Initially, this may suggest particle sampling bias by the sampling probe. While the control distribution ranges from approximately 25-550 µm, the vast majority of particles for the two samples can be contained within a range of roughly 50-300 µm. However it is clear in both samples that large particles are capable of being collected with Sample 1 containing particles as large as almost 500 µm and Sample 2 containing particles as large as 400 µm.

It was determined in Chapter 5 that the sampling probe can be expected to perform sub-isokinetically under the tested conditions. That is, the suction of the probe is not sufficiently large enough to equilibrate the freestream velocity and the sampling velocity. So, the fluid streamlines diverge as they approach the sampling probe. Therefore, the flow physics of the system would suggest an *under-sampling* of small particles, the opposite of what is observed. This conclusion is also confirmed in relevant literature such as [6, 7]. With this knowledge it is important to consider that it is possible that the sampling probe may have not been exposed to a representative percentage of the largest particles contained in the test dust. One interesting observation made in Chapter 4 showed that during the experiment, a higher percentage of particles were present in the lower half of the domain than in the upper half. Presumably the influence of gravity contributed to this occurrence. It would then be a logical assumption to suggest that these particles would be large, implying that fewer large particles would have been in the path of the concentrically located sampling probe. A system level consideration of the test along with the results of Figure 6.3 suggest that further analysis may be required before a definitive conclusion can be drawn about the sampling probe's ability to capture a representative sample of the test dust of interest.

6.3.2 Particle Number Density

Previous attempts to estimate concentration using the particle sampling probe have proved inconclusive. In Chapter 5, results estimated the concentration sampled by the probe to be signif-

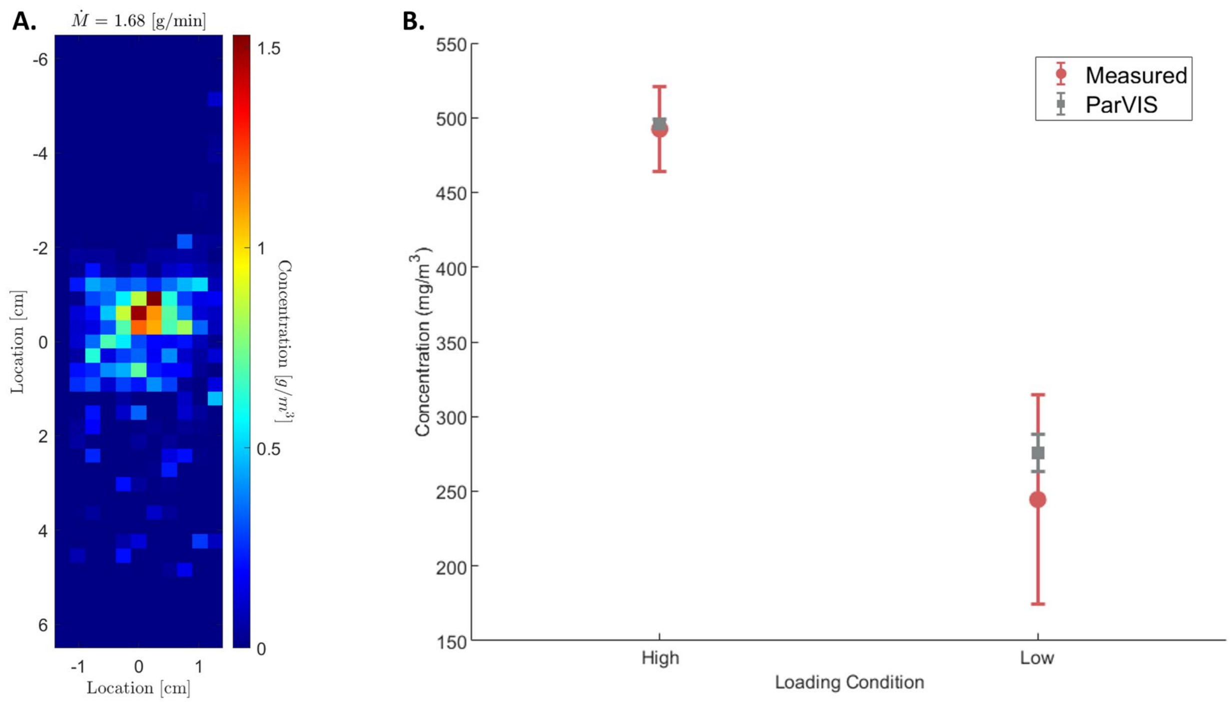

Figure 6.4: Local concentration map of the time-averaged data showing an overall non-uniform particle distribution (A). Concentration estimates of the ParVIS technique and the particle sampling probe are compared. Results indicate that the two estimates match within the uncertainty bounds of the sampling probe data.

icantly higher than the known concentration of the free jet. Attempts were made to account for this discrepancy with little success. Table 6.2 provides estimated concentration values for the sampling probe during the experimental runs using equation 6.2. As previously stated, the test dust was introduced to the engine inlet at two different loading conditions; a high loading condition corresponding to an inlet concentration of 45 $\mathrm{mg\,m^{-3}}$ and a low loading condition resulting in a concentration at the inlet of 22.5 $\mathrm{mg\,m^{-3}}$. Comparing the values to the estimated concentration values in Table 6.2, we again see that the probe seemingly overpredicts the concentration of the flow. However, previous analysis in Chapter 4 showed that the test dust local concentration map was highly non-uniform. This suggests the possibility that the local concentration in the region of the probe may have been higher than the predicted value.

In an attempt to achieve a more accurate estimate of the local concentration in the sampling region, the local concentration map provided by the illumination technique (ParVIS) of Chapter 4 is again considered. Here, the binning region is increased to equal the area of the sampling face as seen in Figure 6.4A and data from runs with high and low particle loading are analyzed. Unfortunately, data for the sample runs analyzed above were not available for the illumination technique. Therefore, the comparison of local concentration values provided in Figure 6.4B are not of the same engine run. However, the compared data are from the same test conditions, just gathered at different times. The objective of comparing the concentration estimates between these two data sets is to provide a possible explanation for the previously observed discrepancy and to support the efficacy of a concentration estimate by the particle sampling probe. The results shown in Figure 6.4B show agreement between the two methods well within the uncertainty bounds of the measurement. Here, both cases estimate the local concentration in the near-probe region to be roughly ten times that of the calibrated particle concentration provided in Table 6.1. This is again consistent with the previous estimates of concentration by the probe which were significantly higher than the calibrated value. While the number of data points is admittedly limited, this result provides the first evidence to support the local concentration value reported by the particle sampling probe. Analysis coupling the particle sampling probe with the ParVIS technique may be an avenue for further verifying the accuracy of the reported concentration by the sampling probe and is recommended for future investigation.

6.4 Conclusion

In this study, a particle sampling probe which is under continued development is tested during a live engine run using a Rolls-Royce M250-C20B turboshaft engine at the Virginia Tech Sand Ingestion Engine Test Cell. The particle sampling probe was placed directly upstream of the engine inlet and subjected to particle ingestion at two different particle loading regimes at engine ground idle conditions. There were two scientific objectives of this investigation: to determine whether the sampling probe is capable of collecting a representative sample of C-Spec test dust, and whether the concentration estimated by the sampling probe is accurate. Results are preliminary but particle size distribution comparisons show that the probe may be capable of sampling representative quantities. However, further analysis is advised before a conclusive verdict may be reached.

To analyze the validity of the concentration estimates by the sampling probe, a previously developed technique was leveraged to compare results. The particle illumination technique discussed in Chapter 4 was used to interrogate the local concentration in the near probe region during high and low particle loading tests. The results are compared with estimates using the mass gathered by the sampling probe. While only two sets of data are analyzed, the results show good agreement with the measured concentration estimates by the sampling probe. This suggests that coupling the illumination technique to sampling probe measurements may be a feasible method to achieve conclusive verification of the reported concentration. Finally, the concentration estimate obtained is consistent with the illumination technique, but the measurement still contains significant uncertainty. To ensure archival quality results, it is essential to minimize this error. The precision scale used during the tests resulted in a relatively high uncertainty in the collected sample mass. Thus, to obtain more accurate measurements in the future, it is recommended to use a higher precision scale or to collect a larger mass of the sample.

References

[1] R. J. Clarkson, E. J. E. Majewicz, and P. Mack, "A re-evaluation of the 2010 quantitative understanding of the effects volcanic ash has on gas turbine engines," *Proceedings of the Institution of Mechanical Engineers, Part G: Journal of Aerospace Engineering*, vol. 230, no. 12, pp. 2274–2291, 2016.

[2] "Mil e-5007 and mil-av-e-8593f." [Online]. Available: œMilE-5007andMil-AV-E-8593F, PowderTechnologyInc.Available:https://www.powdertechnologyinc.com/product/mil-e-5007/
.

[3] R. Moffat, "Contributions to the theory of single-sample uncertainty analysis," 1982.

[4] Adam Equipment. (2019) Luna precision balances: Ltb 2602e. https://www.adamequipment.com/ltb-2602e/, [Accessed April 30, 2022].

[5] Kelly Pneumatics. (2021) Digital mass flow sensor. https://kellypneumatics.com/product/digital-mass-flow-sensor/, [Accessed April 30, 2022].

[6] S. L. Soo, J. J. Stukel, and J. M. Hughes, "Measurement of mass flow and density of aerosols in transport," *Environmental Science & Technology*, vol. 3, no. 4, pp. 386–393, 1969.

[7] Davies, "The entry of aerosols into sampling tubes and heads," 1968.

7. Aerodynamic Assessment of an Anisokinetic Particle Sampling Probe - A Numerical Study

As in Chapter 6, the contents of this chapter serve as a direct continuation of the investigation in Chapter 5. Here, results from that work are reassessed and new conclusions are drawn using computational fluid dynamics investigations. It is the intent of the author that this work serve as a significant contribution to a publication that will be completed at a later date in cooperation with additional authors.

Abstract

The present study assesses the performance of an anisokinetic particle sampling probe currently under development by researchers at Virginia Tech for use in a turboshaft engine undergoing solid particulate ingestion. Building on results from previous studies, a numerical investigation is conducted using the commercially available software, Simcenter STAR CCM+. Results confirm previous findings that the sampling probe operates sub-isokinetically for the flow regimes of interest. Additionally, the aerodynamic performance of the probe suggests that efficiency is inversely proportional to both Mach Number and yaw angle relative to the fluid freestream. A new definition for the calculation of the aerodynamic efficiency parameter is presented which may provide a more robust assessment of probe performance under a wide range of flow scenarios. Finally, a design modification is offered which may be of interest to future investigations. By transitioning from an internal chamfer design to an external chamfer design, researchers show a more than threefold increase in aerodynamic efficiency over the previous design. These results indicate that the proposed geometry modification may offer an attractive solution to increasing effectiveness of the particle sampling probe under a wider range of particle sizes and flow regimes in future investigations.

7.1 Introduction

In harsh environments, the ingestion of solid particulates has long been known to hinder the performance of gas turbine engines. These particulates can range from ash to sand to dust, and their ingestion can cause engine failure, a temporary flameout, and reduced engine performance. Flameout is an event that occurs when the flame in the combustion chamber of a jet engine has been extinguished, resulting in a total loss of power. In conventional aircraft, the ingestion of significant dust is not uncommon, particularly during takeoff and landing. Historically, the effects of particulate ingestion have had significant impacts on aviation, resulting in equipment damage, logistics issues, and, in extreme cases, loss of life. For example, the Lockheed L-100 aircraft experienced two engine failures and two temporary engine flameouts while flying over Mount St. Helens after a volcanic eruption [1]. Similarly, the KLM Royal Dutch Airlines Boeing 747-400, equipped with four General Electric CF6-80C2 engines, entered an ash cloud caused by the eruption of Mt. Redoubt and experienced a four-engine flameout, forcing the flight crew to make an emergency landing [2, 3].

Vertical takeoff and landing (VTOL) aircraft, as well as helicopters, are particularly at risk due to their tendency to generate significant debris during takeoff and landing operations. The US military has raised concerns about this risk. For instance, a Marine Corps MV-22 Osprey crashed during a training exercise in Hawaii, leading to the death of two US Marines and injuring 20 other personnel [4]. The cause of the fatal crash was attributed to dust ingestion resulting in an engine failure. Additionally, during Operation Iraqi Freedom, the United States Army experienced a reduced availability of its CH-47 helicopters due to premature engine failures of between 75% to 95%, which were directly linked to sand ingestion [5]. Although solid particulate ingestion is inevitable for aircraft operating in hazardous environments, research has demonstrated that it can cause premature engine wear. Researchers have expressed an interest in investigating how ingested sand particles traverse an aircraft engine compressor. While civilian aircraft fleets are typically prone to the ingestion of high-atmospheric particles, such as volcanic ash, military aircraft are more typically damaged by dust and sand particles when flying near the ground. Helicopters and VTOL aircraft operating in desert environments are at the greatest risk of solid particulate ingestion. To mitigate these risks, researchers and manufacturers continue to explore new ways to reduce the effects of ingestion of solid particulates by aircraft engines. Overall, continued research into this phenomenon is critical for ensuring the safety and reliability of air travel in hazardous environments.

To this end, an anisokinetic particle sampling probe is under continued development by researchers at Virginia Tech for the purpose of passively offtaking particles from a gas stream inside a gas turbine engine [6]. In that work, the aerodynamic performance of the probe was assessed using a free jet rig at Mach numbers ranging from ($0.25 \leq M \leq 0.70$) and at yaw angles of ($\theta = 0°, 20°, 45°$) relative to the freestream. Additionally, the probe demonstrated effective sampling of a range of particle sizes ($100\mu m \leq d_p \leq 1300\mu m$) at these conditions. However, it was determined that for the relevant flow scenarios, the probe performed sub-isokinetically which leaves the possibility of undersampling the particle flow and biasing the results of the gathered sample. The objective of the present study is to use commercially available computational tools to further examine the conclusions drawn by the previous investigation and determine if a more effective design may be considered.

7.2 Background

The use of aerodynamic probes has been a useful diagnostic approach for researchers for over two centuries, with the Pitot probe first introduced by Henri de Pitot in 1732 [7] and improved upon by Darcy in 1858 [8] being one of the most widely used instruments in aviation. Although aerodynamic probes can now take on various shapes and sizes, they continue to be an invaluable tool for evaluating complex flow conditions. With the rapid increase in computational abilities, it is becoming increasingly common to inform probe design decisions through computational fluid dynamics (CFD) studies. For instance, Vincent et al. investigated the behavior of a total temperature probe using CFD and conjugate heat transfer analysis, gaining a better understanding of the probe geometry's impact on heat transfer properties, leading to the presentation of an analysis methodology for improved design capabilities [9].

There have also been several modifications to traditional probes using CFD analysis to increase efficiency and operating range. For example, a radially traversing temperature probe for use on gas turbines was developed, and researchers successfully modified existing probe geometries to improve efficiency and operating range [10]. Shumeli et al. used Ansys CFX simulations to inform the design of a non-standard Pitot probe, demonstrating the possibility of using sampling probes within gas-liquid systems [11].

Today, particle sampling probes are the default method for capturing airborne particles for atmospheric research, nuclear gas stack sampling, or any measurement involving the physical sampling of aerosol media. As such, much research has focused on the most efficient methods of design of these instruments under a wide range of flow scenarios [12–21]. Historically, these investigations have primarily focused on particles classified as aerosol Particulate Matter (PM) 2.5 or PM10. That is, particles with a mean diameter of 2.5 μm (PM2.5) or of 10 μm (PM10). Additionally, these investigations have typically studied particles traveling at speeds less than 50 $m\,s^{-1}$ [22].

Although the investigation of these systems has been ongoing for more than 80 years, several complexities remain that impede their flawless deployment. These complexities include particle bounce from wall interactions, particle-particle collisions, deposition, sampling probe intrusive effects on flow fields, momentum transfer between phases, and departure from isokinetic conditions. Despite the challenges, substantial progress has been made, especially with respect to the isokinetic sampling of aerosol material. The literature shows that measurement error is minimized for a sampling probe that is sharp-edged and thin-walled [21, 23, 24]. Researchers have also investigated measurement error due to anisokinetic sampling conditions and considered the effect of flow direction relative to the sampling face [13, 20, 25–28]. Sansone and Ruping accounted for measurement effect by probe bend [25, 29]. Also, velocity slip between the carrier and dispersed phases has been studied for large particles [28, 30].

Generally, achieving an isokinetic condition is critical for an accurate calculation of particle concentration. In many cases, this can be achieved by aspirating the pressure within the probe with a suction flow [31, 32]. Other work has modified the inlet pressure by increasing the fluid temperature at the probe face using either a hot wire or electric heating [33]. Once particles have been sampled, it is customary to collect the sample to determine particle mass flux. To establish an accurate estimate of particle mass flow that mitigates the effects of unsteady sampling, it is suggested that two samples, m_{p1} and m_{p2}, be taken over two distinct sampling periods, Δt_1 and Δt_2 [31]. Literature suggests that for the sampling of aerosols, the particle Reynolds number at terminal velocity remains within the Stokes regime for particles less than 60 $\mu\mathrm{m}$ with a typical density of 2000 $\mathrm{kg\,m^{-3}}$ [31]. Therefore, a time-averaged particle concentration can be estimated given particle mass flux and the determination of time-averaged particle velocity.

7.2.1 Parameter Characterization

For particles suspended in flow, a primary metric of characterization is the particle Stokes number where

$$St = \frac{\tau_p}{\tau_f} \tag{7.1}$$

and τ_p is the momentum response time of a particle and the characteristic time scale of the carrier phase is τ_f. The particle response time is defined as

$$\tau_p = \frac{\rho_p d_p^2}{18\mu_f C} \tag{7.2}$$

where ρ_p is the particle density, d_p is the particle diameter, μ_f is the dynamic viscosity of the fluid, and C is the non-Stokesian correction factor

$$C = \begin{cases} 1 + Re_p^{2/3}/6 & \text{at} \quad Re_p \leq 10^3 \\ 0.11 Re_\mathrm{p}/6 & \text{at} \quad Re_p > 10^3 \end{cases}. \tag{7.3}$$

The particle Reynolds number, Re_p is

$$Re_p = \frac{\rho_p |u - v| d_p}{\mu_f}, \tag{7.4}$$

and $|u - v|$ is the relative velocity of the particle with respect to the fluid [34]. We define the characteristic timescale of the flow as

$$\tau_f = \frac{D_s}{U_B} \tag{7.5}$$

where U_B is the bulk velocity of the jet, and D_s is the probe outer diameter. This definition of Stokes number assumes the particle is spherical but is the standard definition used in relevant literature [34, 35].

In the previous study, the primary metric used to evaluate the aerodynamic performance of the probe is the aspiration efficiency (A_e) described as

$$A_e = \frac{A_0}{A_s} \tag{7.6}$$

where A_s is the frontal projected area of the probe and A_0 is the area of the undisturbed streamtube [6]. This ratio provides insight into the probe's ability to sample small particles with $St < 1$. The probe operating under the sub-isokinetic regime results in $A_e < 1$. Here, streamlines will diverge near the probe inlet, causing Stokesian particles to be undersampled. Conversely, the probe operating under super-isokinetic conditions results in $A_e > 1$, which means the streamlines will converge near the probe inlet, causing smaller particles to be oversampled. With this definition of aerodynamic efficiency, it follows that any value where $A_e \neq 1.0$ results in a condition that is anisokinetic. Typical probe design aims to achieve isokinetic sampling for the condition relevant to the flow being sampled. In the previous study, Olshefski et. al found that for all relevant flow scenarios, the sampling probe discussed performed sub-isokinetically. As previously stated, the aim of the current investigation is to determine if this performance may be improved by design modification through computational analysis.

7.2.2 Probe Design

The probe was designed with the constraint of the environment in which it is intended to be installed, inside the stator row of a turboshaft engine axial compressor. This required that the axial length of the sampling probe not exceed 25mm and that the frontal area be minimized. With this, the probe length was designed to 20 mm, the internal diameter was constrained to 2 mm, and the external diameter chosen was 4 mm. To maximize sampling area, the authors chose to incorporate an internal chamfer of 30°. An example of the finalized probe geometry can be seen in Figure 7.1.

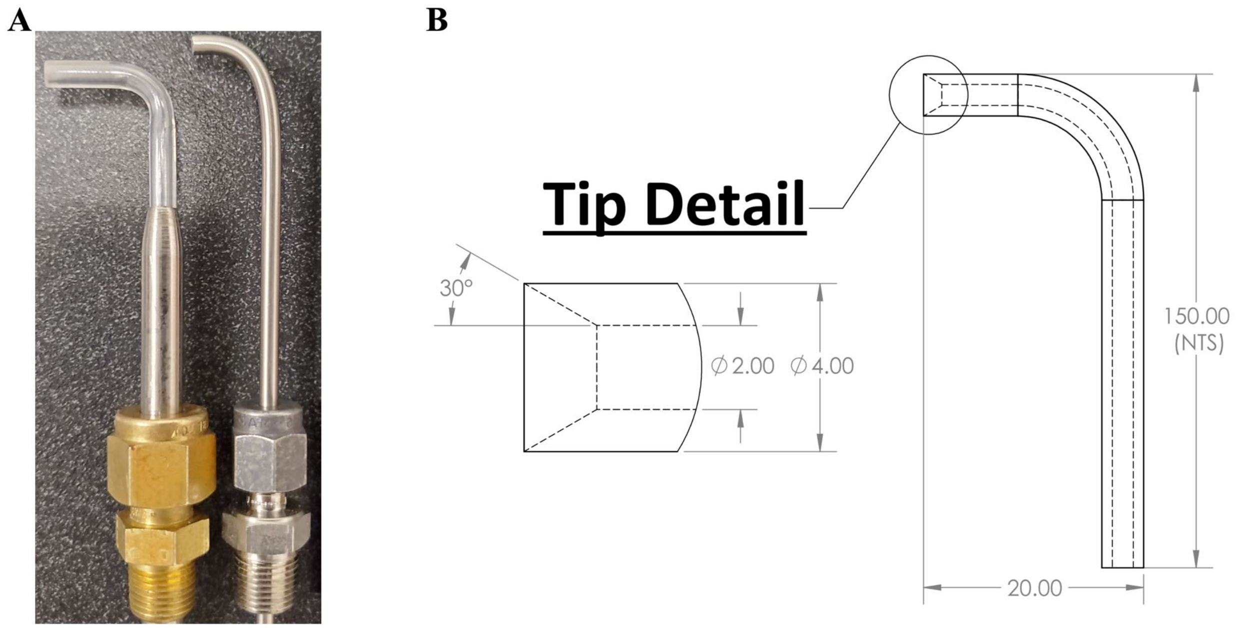

Figure 7.1: Sampling probe (left) placed next to early steel prototype (A) and probe dimensions in mm (B). Image taken from [6] with permission.

7.3 Numerical Approach

7.3.1 Methods Used

Steady state Reynolds Averaged Navier-Stokes (RANS) simulations are conducted using the commercially available software package, Simcenter STAR CCM+. Here, the fluid phase is solved for using Eulerian RANS equations and a two-equation κ-ω SST model is used to solve for turbulence physics. RANS simulations require the selection of a turbulence modeling scheme to provide accurate quantitative fluid properties for time averaged flow. While many such models have been developed in the past, the performance of the κ-ϵ and κ-ω models are well established. Literature suggests that the κ-ϵ model may predict velocity and friction factor of a system better than the κ-ω scheme [36]. However, the SST κ-ω model may provide a more stable and accurate estimation of turbulence intensity compared to other studied turbulence models, hence the SST κ-ω method is used for this study [37]. In addition to the above considerations, several additional physics models are implemented to ensure reality approximation. These include the incorporation of gravity, an All-y+ wall treatment which makes the model suitable for a wide range of wall-cell mesh densities, and a psuedo-time marching energy coupling scheme to ensure the solution remains conservative. All selected methods are at least second-order accurate as advised by [38]. The RANS solver is a

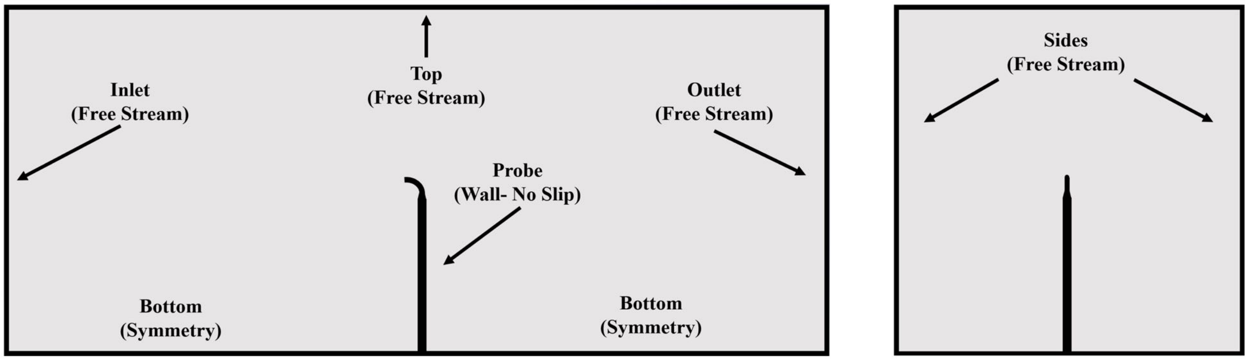

Figure 7.2: Side and front view schematics of 3-D computational domain with labeled boundary conditions.

pressure based coupled flow solver whereby the fluid phase density is computed using an ideal gas assumption. The boundary conditions selected for these studies can be seen in Figure 7.2 and are chosen to mimic the test conditions of the previous experiment.

7.3.2 Computational Domain and Boundary Conditions

The previous investigation placed the sampling probe concentric to and 2.54 cm upstream of a free jet. A primary assumption from that work was that the probe was sufficiently close to the nozzle exit as to assume the probe was fully entrained in the core region of the jet and therefore, the bulk flow velocity was uniform. For the current study, it was therefore determined that given a sufficiently large domain, a uniform velocity profile may be applied to the simulation. A rectangular domain was chosen as seen in Figure 7.2. While this domain differs from the experimental studies of Olshefski et. al. with the omittance of a jet flow source, the freestream physics should be nominally equivalent [6]. Previous studies have shown that a distance of 20 characteristic lengths between a body and boundary is sufficient for setting a freestream boundary condition [39–41]. Therefore, this criteria was enforced for this study as well. The probe sampling diameter is 4 mm and the probe stem is 6 mm in diameter. The axial length of the probe is 14 mm instead of the previously described 20 mm as this most closely matches the dimensions of the manufactured probe. At the boundary of the sampling probe exit, a mass flow condition was set to aspirate $5.72{\times}10^{-4}\ \mathrm{kg\,s^{-1}}$ of air from the probe, which matched experimental values.

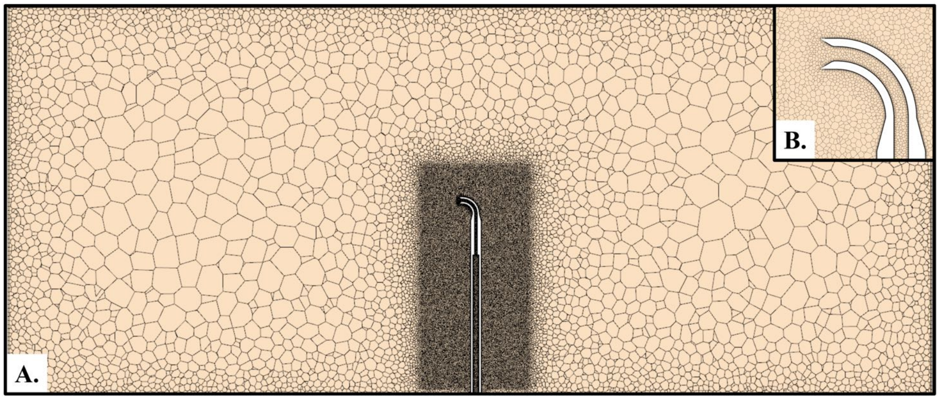

Figure 7.3: Side view of domain showing full mesh representation (A.) and near-probe detail (B.).

7.3.3 Mesh Details

The computational mesh was created using the built-in meshing capabilities of Simcenter STAR CCM+ and incorporated polyhedral cells with a base size of 6.25×10^{-4} m. The mesh representation can be seen in Figure 7.3. Fifteen prism layers were applied to the probe walls with an overall thickness of 5% of the base cell size. A local refinement region encloses the probe to increase near-probe fidelity while not increasing computational costs considerably. This resulted in a final grid with approximately 2.64M cells. A grid refinement study was conducted to ensure adequate resolution of scalar quantities of interest. This study was conducted in accordance with the guidance provided in [38]. Here, the cell count was halved from an initial mesh and freestream velocity profiles were analyzed at varying axial locations for consistency as seen in Figure 7.4. To achieve accuracy in the comparison of two distinct mesh sizes, the figure presented employed linear interpolation schemes to guarantee the co-location of spatial probing locations. Without such an interpolation method, a sufficient or satisfactory comparison would not be feasible, potentially leading to biased results. However, by utilizing the interpolation schemes, the figure was able to facilitate a precise comparison between the mesh sizes. Negligible difference was found between the two meshes suggesting that the fine mesh is acceptable for ongoing analysis.

7.4 Results and Discussion

As discussed in Section 7.1 the sampling probe was previously tested at two different Mach numbers (M={0.25, 0.70}) and three different yaw angles (θ={0°, 20°, 45°}). For this study, it was determined that the inclusion of the θ=45° test case was unnecessary as it exceeds the conditions

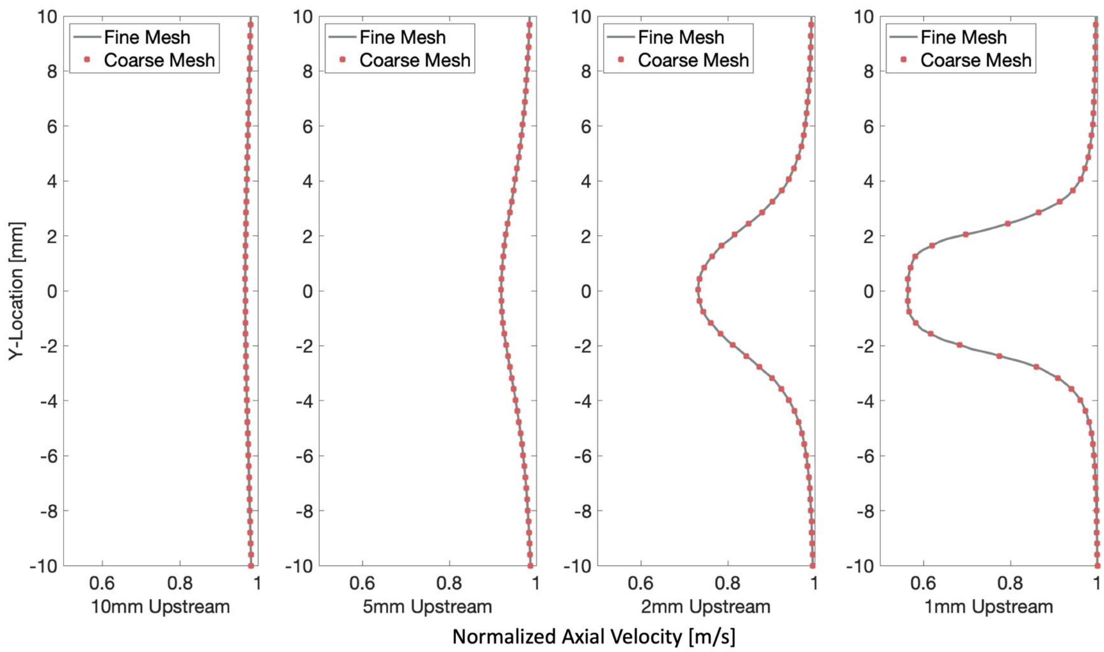

Figure 7.4: Axial velocity profiles at locations upstream of the sampling probe face ($M = 0.25, \theta = 20°$)

which will be seen inside the engine environment. For this reason, simulations were conducted at the two Mach numbers (M={0.25, 0.70}) and at yaw angles of θ = {0°,20°}. There were three primary conclusions drawn in the previous study [6] with regard to the aerodynamic performance of the particle sampling probe:

1. Sampling velocity is reduced markedly near the probe face.
2. The sampling probe operates sub-isokinetically for all relevant flow scenarios as determined by the assessment of the aerodynamic efficiency (A_e).
3. Probe aerodynamic efficiency (A_e) is inversely proportional to freestream Mach number (M) and yaw angle (θ).

The current study aims to computationally recreate these results and provide further commentary on their implications. First, an initial model validation is required to ensure that the system being modeled appropriately captures the dynamics which occurred during the physical experiment. The results of these validation studies are compared to experimental results. Having built confidence in the model and replicated experimental results within reasonable certainty, further analysis may be initiated.

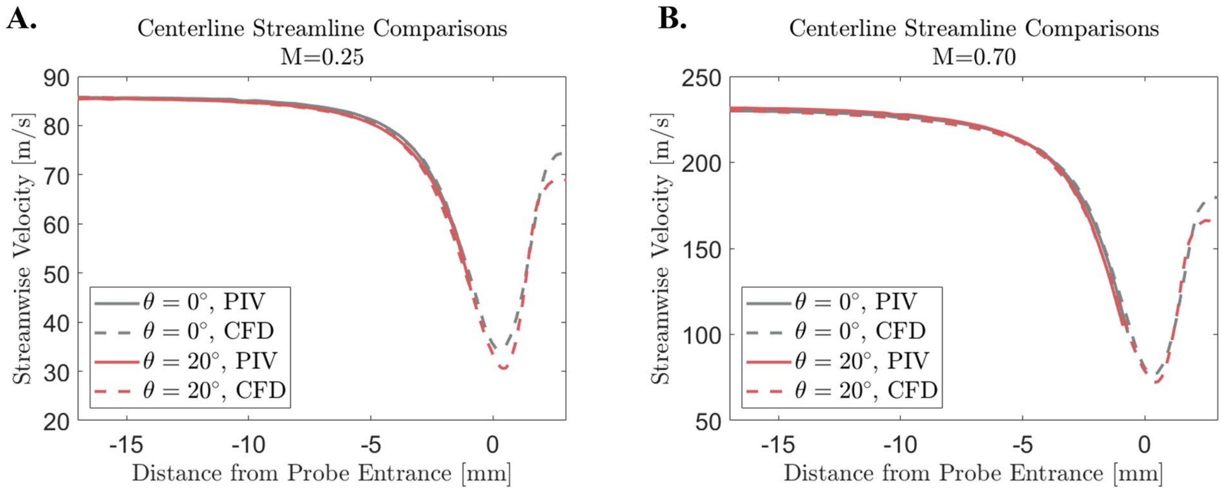

Figure 7.5: A comparison of experimental and computational results of axial velocity located concentrically to the probe sampling face. A marked reduction in velocity is seen in the near-probe region for all cases.

7.4.1 Model Validation

Having an aerodynamic understanding of the probe behavior is critical for predicting particle sampling performance. As a measure to compare results from the PIV study and the CFD study, Figure 7.5 compares the axial velocity along a streamline which is concentric with the centerline of the sampling probe for the M=0.25 case (7.5A) and for the M=0.70 case (7.5B) at yaw angles of θ={0°,20°}. Both experimental PIV and simulated CFD results are compared. Here, it is clear that the results from the two modalities are in excellent agreement. It is also evident however, that the data from the PIV investigations is not as complete as that for the CFD. The reason for this is twofold. First, the CFD data is able to account for the flow within the probe where the laser sheet is unable to penetrate, one of the primary advantages of the simulation approach. Secondly, the experimental data needed to be manually truncated approximately one millimeter upstream of the sampling probe entrance due to the presence of nonphysical data in this region. This is likely due to the fidelity of the PIV experiment and does not invalidate the present study.

7.4.2 Velocity Reduction

With the results of Figure 7.5, we determine that the boundary conditions of the simulation sufficiently mirror the conditions seen by the experimental study for all cases and that subsequent analysis is well-founded. In this figure, a considerable reduction in axial velocity near the probe

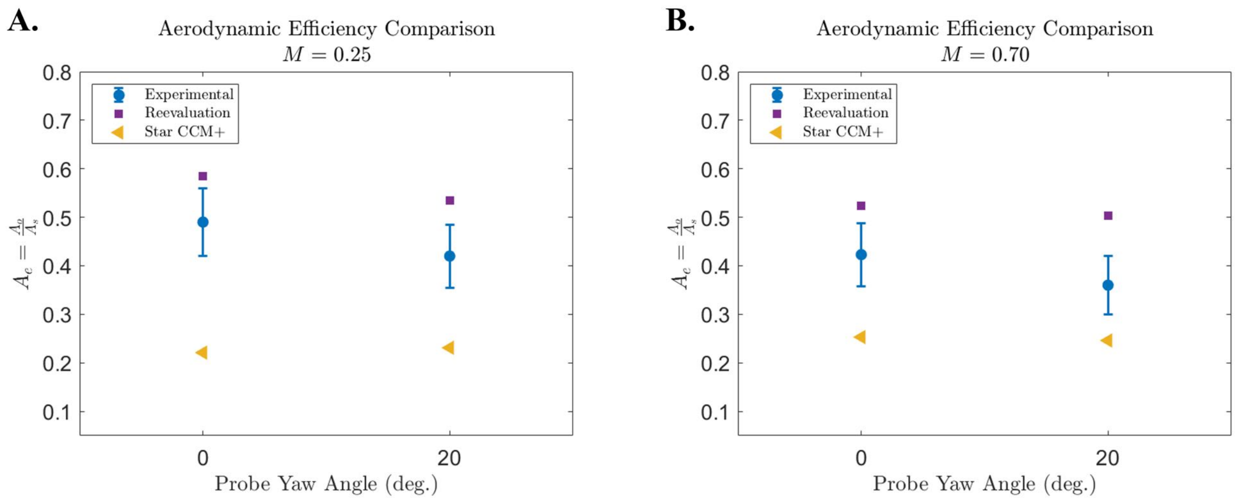

Figure 7.6: A comparison of experimental and computational results of aerodynamic efficiency.

face is observed. The previous study concluded that this decline may be as much as 55%. However, the CFD results suggest that the reduction may be even more severe. For the low Mach case (M=0.25) the centerline velocity is reduced from 85 $\mathrm{m\,s^{-1}}$ to approximately 36 $\mathrm{m\,s^{-1}}$ for the zero degree yaw angle case. For the twenty degree case, the velocity is further reduced to 27 $\mathrm{m\,s^{-1}}$. For the high Mach case (M=0.70), the velocity is reduced from 230 $\mathrm{m\,s^{-1}}$ to roughly 79 $\mathrm{m\,s^{-1}}$ for the zer degree case and to 72 $\mathrm{m\,s^{-1}}$ for the twenty degree case. Worth noting however, the simulation results show that after passing the probe face region, the velocity begins to increase before finally reaching a final velocity peak. For the low Mach case the velocity increases to a maximum value of approximately 75 $\mathrm{m\,s^{-1}}$ and for the high Mach case the centerline velocity develops to roughly 189 $\mathrm{m\,s^{-1}}$. In each case, this velocity peak is short-lived before declining to zero at the aft wall of the probe as would be expected. The observed increase in velocity is rationalized by considering conservation principles and the area reduction due to the internal chamfer design of the probe.

7.4.3 Aerodynamic Efficiency

As discussed in Section 7.2.1 the aerodynamic efficiency, the primary parameter used to determine aerodynamic performance of the sampling probe, is defined as the ratio of the area of the undisturbed streamtube to the projected sampling area and it was established by measuring the streamtube diameter at these locations from the experimental data. This is achieved by manually estimating the streamline position at locations of interest. In Figures 7.6A and 7.6B, the original estimates (marked as blue circles) show a decline in efficiency with both Mach number and yaw angle. However, when the CFD data (amber triangles) were analyzed, there was a noticeable discrepancy between the two methods. Because of this discrepancy, a reevaluation of the original PIV data was conducted (purple squares). Here we see again that there is a considerable difference between values of the reevaluation and the originally published result. Additionally, for all cases, the simulated data consistently underpredicts the efficiency of the probe when compared to the experimental data. From Figure 7.5 we observed that data near the probe face was unreliable. From this we can conclude that it is only possible to obtain streamtube diameter information upstream of the probe face using the experimental data whereas with the idealistic simulated results, it is possible to make these estimates with a high degree of certainty. This explains the regular occurrence of the underpredicted performance of the probe as the streamtube diameter roughly one millimeter upstream (the location of where the PIV data drops off) will be smaller than that at the probe face, causing an artificial increase in perceived probe performance. Additionally, it should be noted that researchers do not believe that these results suggest a deficiency in the simulated data. Conversely, it is likely that the fidelity of the previous experiment affected the prior estimates. From this effort there are two major conclusions which can be drawn:

1. There is considerable variability in the estimated streamtube area at the probe face, particularly for the PIV data, suggesting initial uncertainty estimates may have been generous.
2. The absence of experimental data in the near-probe region plays a significant role in an accurate estimate of aerodynamic efficiency.

Figure 7.6 also shows that the simulated data predicts an *increase* in efficiency with yaw angle for the low Mach case and that the efficiency remains nearly constant for the high Mach case. This counter-intuitive result motivated a reassessment of the definition of the efficiency parameter. For all previous studies, the aerodynamic efficiency has been defined as in equation 7.6 where the sampling area, A_s, is taken as the frontal projected area of the probe. This selection allows the definition to account for changes in yaw angle. However, historically pitot type probe performance is defined in relation to an idealized case as seen in Figure 7.7 which is taken from [42]. Here, the authors show the change in performance of various probe geometries with respect to changes in yaw angle using the θ=0°case as a baseline.

The previous analysis of Figure 7.6 is repeated using the methodology described by Tropea, Yarin, and Foss and is displayed in Figure 7.8. Here, it is shown that by using the θ=0° case to define the sampling area A_s and keeping this value constant, a more intuitive and appropriate trend is observed in all cases. As a point of interest, it should be noted that the major conclusions drawn

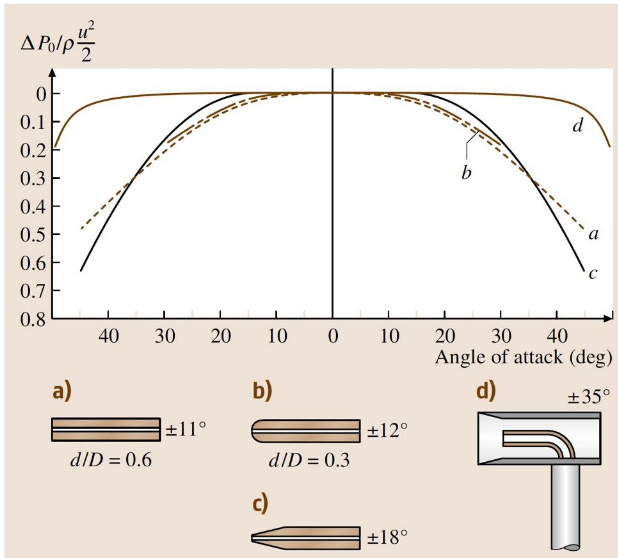

Figure 7.7: A comparison of the performance of various pitot probe geometries with respect to yaw angle [42].

by the previous study remain unchanged with this new analysis and are confirmed using the CFD results. That is, the sampling probe performs sub-isokinetically for all relevant flow scenarios and the aerodynamic efficiency of the probe is inversely proportional to both Mach number and yaw angle. However, it is the position of the current study that this updated definition provides a more appropriate assessment of the probe's performance under a wide range of flow scenarios.

7.4.4 Design Modification

In an attempt to raise the aerodynamic efficiency of the probe and to more closely approach an isokinetic condition, a design modification is considered. It is hypothesized that a more streamlined probe face may reduce the pressure gradient observed in the near-probe region of the current design. Therefore, the internal chamfer of the current design is removed and an external chamfer of the same slope is substituted as shown in Figure 7.9. Additionally, the probe is designed as a two-piece design with a stem and an elbow. The elbow is press-fit into the stem and brazed for security. This design choice was made to reduce the likelihood of particle clogging as they are transported through the probe.

The performance of this new design was simulated at a yaw angle of θ=0° for the high and low Mach number cases (M={0.25, 0.70}) to determine if any increase in performance may be predicted. Again, near-probe velocity reduction is examined for the new design and compared to

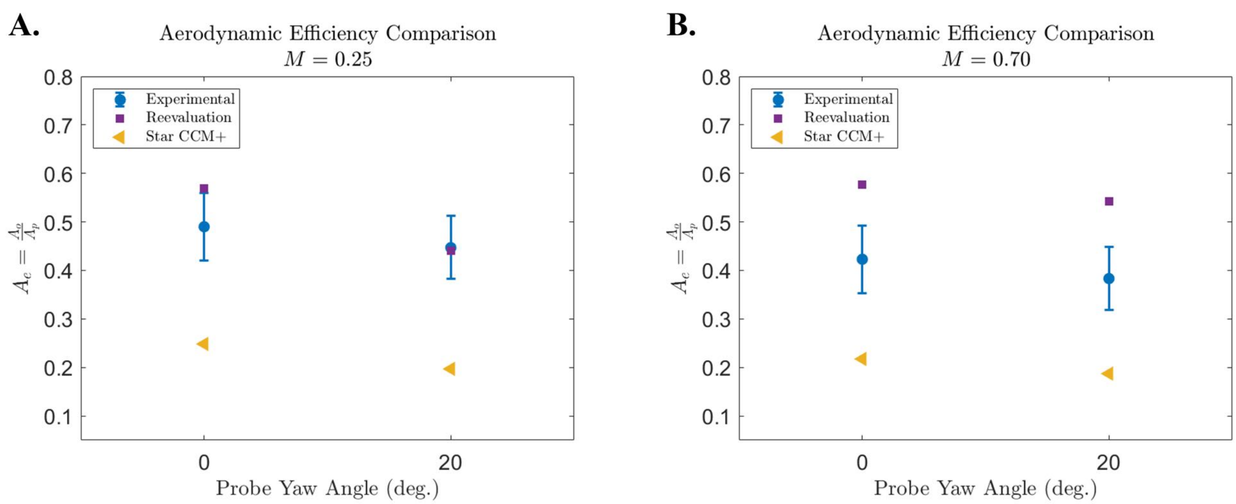

Figure 7.8: Experimental and computational results of aerodynamic efficiency using a newly proposed definition of A_e.

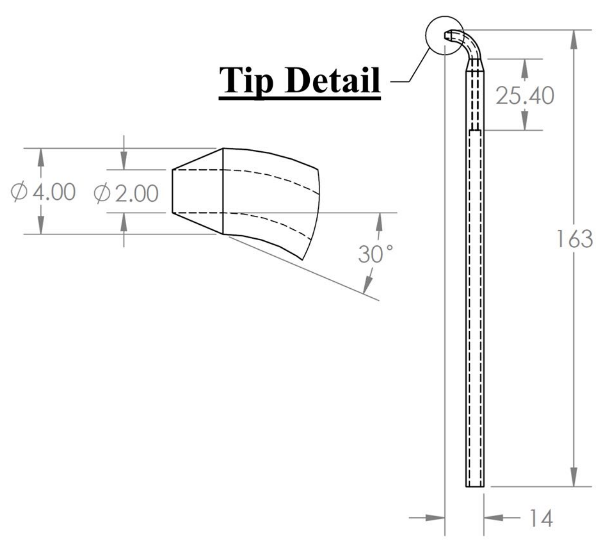

Figure 7.9: Proposed sampling probe design modification incorporating an external 30° chamfer and decreased axial length.

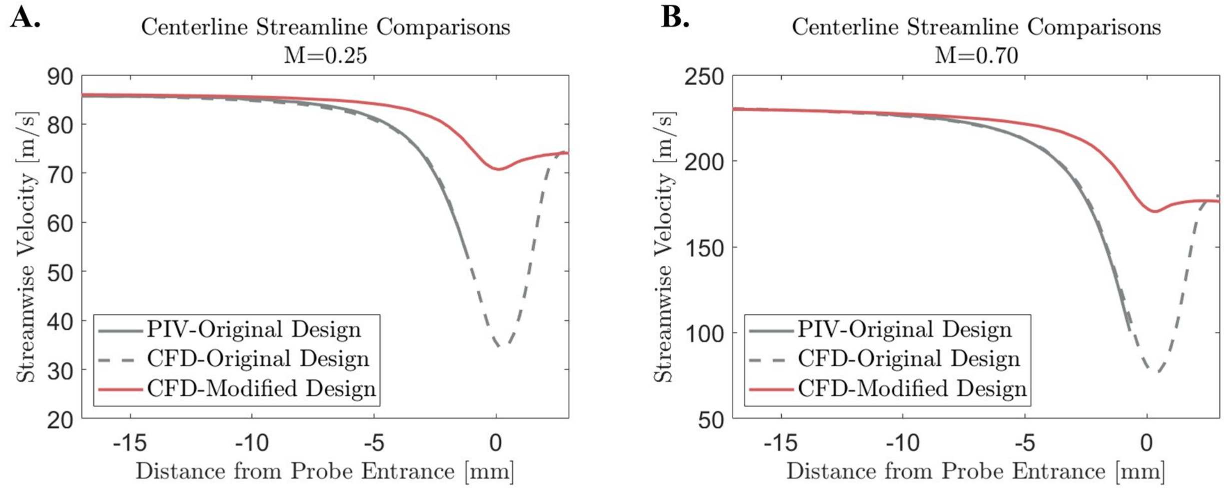

Figure 7.10: Results of axial velocity profile located concentrically to the probe sampling face for the new design case is compared to the original study findings and initial CFD study.

the original geometry in Figure 7.10. For both the low Mach and high Mach cases, the velocity reduction near the probe face is significantly improved. For the low Mach case, the minimum velocity observed is 71 $\mathrm{m\,s^{-1}}$. This results in a 18% velocity reduction versus a 60% reduction by the original design. For the M=0.70 case the new design results in a minimum velocity of approximately 170.5 $\mathrm{m\,s^{-1}}$, or a reduction of 26% whereas the previous design at this condition saw a 67% velocity decline. Additionally, the aerodynamic efficiency is analyzed in Figure 7.11 and compared to the original experimental and simulated results. Here, a dramatic increase in efficiency is observed. The efficiency parameter increases from a value of 0.25 to a values of 0.71 for the low Mach case and from a value of 0.22 to a value of 0.70 for the high Mach number case. These results suggest that the newly proposed design may offer a significant performance increase over the current design from an aerodynamic perspective. However, it is important to consider the primary objective of the sampling probe design. While the proposed geometry does offer significant performance enhancements over the original design aerodynamically, it ultimately reduces the particle sampling area of the probe. The original design offers the opportunity for particles to enter the probe at a diameter of 4 mm. Not all particles in this range will ultimately be sampled by the probe as there is the possibility for particles to bounce off of the chamfered face and return to the flow. But, the new design limits the particle sampling diameter to 2 mm which may reduce the total number of particles sampled. In the previous work, Olshefski et. al determined that the aerodynamics of the sampling probe did not notably alter the samplability of the particles of interest as the particle Stokes numbers were sufficiently high to allow the majority

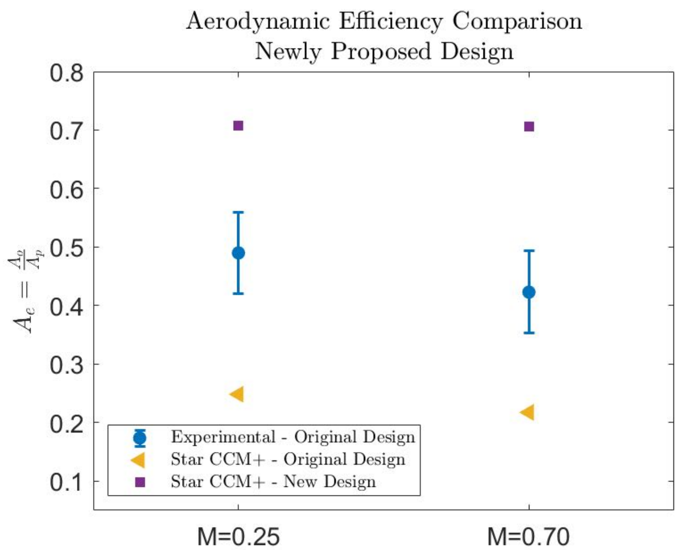

Figure 7.11: The aerodynamic efficiency parameter is compared for the original design probe geometry and the new design profile. Here, there is a clear increase in efficiency for the novel design case.

of particles to behave ballistically. Although, this conclusion will not be universal and may need to be reconsidered for each flow scenario and particle type studied. Therefore, unless the primary objective of the study is to capture the maximum number of particles, incorporating the design change presented above should only serve to enhance the performance of the sampling probe and increase the consistency of results.

7.5 Conclusions

In this work, the performance of a particle sampling probe which is under continued development is explored using computational fluid dynamics by way of the commercial software Simcenter STAR CCM+. An initial investigation ensured that computational results mimicked the boundary conditions seen by a prior experimental study and a mesh convergence study was conducted. With model validation established, follow-on simulations sought to gain additional insight into the aerodynamic performance of the sampling probe. Results confirmed prior findings that there is a significant velocity reduction of the fluid flow in the near-probe region, that the probe operates sub-isokinetically for all flow cases, and that aerodynamic efficiency is inversely proportional to both Mach number and yaw angle relative to freestream.

With these results, a new definition for the calculation of the aerodynamic efficiency parameter, A_e, is proposed based on similar estimates for traditional pitot probe geometries. The new definition does not significantly alter the results or conclusions drawn by the data of this study but may offer a more robust formulation for future studies. Additionally, a design modification is proposed to increase the aerodynamic performance of the probe. This modification includes altering the probe tip from an internal chamfer design to an external chamfer design. While this design ultimately reduces the particle sampling area, a dramatic increase in aerodynamic performance is observed suggesting that such an alteration may benefit future work. Consideration is given to the objective of the sampling probe design and a case may be made that the prior design is superior in limited cases. However, unless the objective of the study is to capture the maximum number of particles, it is the conclusion of this work that incorporating the design modification presented should only serve to provide more consistent results with higher efficiency.

References

[1] H. Mitchell and F. Gilmore, "Dust-cloud effects on aircraft engines: emerging issues and new damage mechanisms," *Paper No. RDA-TR-120012-001*, 1982.

[2] C. A. Neal, T. J. Casadevall, T. P. Miller, J. W. Hendley II, and P. H. Stauffer, "Volcanic ash-danger to aircraft in the north pacific," US Geological Survey,, Tech. Rep., 1997.

[3] R. C. Daw, "Aviation accident final report," Washington D.C., Tech. Rep., 1992.

[4] R. Whittle, "Fatal crash prompts marines to change osprey flight rules," *Breaking Defense, available at http://breakingdefense. com/2015/07/fatal-crash-prompts-marines-to-change-osprey-flight-rules/(accessed 15 August 2016, 16 July 2015*, 2015.

[5] K. Brun, M. Nored, and R. Kurz, "Particle transport analysis of sand ingestion in gas turbine engines," vol. 134, no. 1, 2012, Journal Article.

[6] K. Olshefski, A. Collins, T. Coulon, T. Lowe, and W. Ng, "Development of an anisokinetic particle sampling probe for use in a gas turbine engine compressor," *Frontiers in Mechanical Engineering*, 2022.

[7] G. O. Brown, "Henry darcy's perfection of the pitot tube," in *Henry PG Darcy and Other Pioneers in Hydraulics*, 2003, pp. 14–23.

[8] H. Darcy, "Note relative à quelques modifications à introduire dans le tube de pitot," in *Annales des ponts et chaussées*, vol. 1, 1858, pp. 351–359.

[9] T. G. Vincent, "Total temperature probe performance for subsonic flows using mixed fidelity modeling," Thesis, 2019.

[10] Wilson, "A robust radial traverse temperature probe for application to a gas turbine hp/ip

stage," 2012.

[11] A. Shmueli, T. E. Unander, and O. J. Nydal, "Experimental and numerical evaluation and optimization of a non standard pitot/sampling probe," *Engineering*, vol. 5, no. 12, p. 967, 2013.

[12] C. N. Davies, *Dust is dangerous*. Faber & Faber, 1954.

[13] H. H. Watson, "Errors due to anisokinetic sampling of aerosols," *Am Ind Hyg Assoc Q*, vol. 15, no. 1, pp. 21–5, 1954. [Online]. Available: https://www.ncbi.nlm.nih.gov/pubmed/13138521

[14] L. Levin, "The intake of aerosol samples," *Izv. Akad. Nauk SSSR Ser. Geofiz*, vol. 7, pp. 914–925, 1957.

[15] Badzioch, "Collection of gas-borne dust particles by means of an aspirated sampling nozzle," 1959.

[16] Davies, "The entry of aerosols into sampling tubes and heads," 1968.

[17] J. Vincent, D. Stevens, D. Mark, M. Marshall, and T. Smith, "On the aspiration characteristics of large-diameter, thin-walled aerosol sampling probes at yaw orientations with respect to the wind," *Journal of aerosol science*, vol. 17, no. 2, pp. 211–224, 1986.

[18] P. Å. TUFTO and K. WILLEKE, "Dependence of particulate sampling efficiency on inlet orientation and flow velocities," *American Industrial Hygiene Association Journal*, vol. 43, no. 6, pp. 436–443, 1982.

[19] H. Glauberman, "The directional dependence of air samplers," *American Industrial Hygiene Association Journal*, vol. 23, no. 3, pp. 235–239, 1962.

[20] S. Badzioch, "Correction for anisokinetic sampling of gasborne dust particles," *J. Inst. Fuel.*, vol. 33, pp. 106–110, 1960.

[21] N. Fuchs, "Sampling of aerosols," *Atmospheric Environment (1967)*, vol. 9, no. 8, pp. 697–707, 1975.

[22] S. Chandra and A. R. McFarland, "Shrouded probe performance: Variable flow operation and effect of free stream turbulence," *Aerosol Science and Technology*, vol. 26, no. 2, pp. 111–126, 1997.

[23] A. Whiteley and L. Reed, "The effect of probe shape on the accuracy of sampling flue gases for dust content," *J. Inst. Fuel*, vol. 32, p. 316, 1959.

[24] I. Davis, "Sampling probes for duct and stack sampling in: Acgih, editor," *Air sampling instruments for evaluation of atmospheric contaminants. 4th ed. Cincinnati, Ohio*, pp. L11–L13, 1972.

[25] G. Ruping, "The importance of isokinetic suction in dust flow measurement by means of

sampling probes," *Staub-Reinhalt. Luft*, vol. 28, no. 4, pp. 1–11, 1968.

[26] A. Addlesee, "Anisokinetic sampling of aerosols at a slot intake," *Journal of Aerosol Science*, vol. 11, no. 5-6, pp. 483–493, 1980.

[27] C. Zhu, "Dynamic behavior of unsteady turbulent motion in pipe flows of dense gas-solid suspensions," Ph.D. dissertation, University of Illinois at Urbana-Champaign, 1991.

[28] ——, "Isokinetic sampling and cascade samplers," in *Instrumentation for Fluid Particle Flow*. Elsevier, 1999, pp. 9–46.

[29] E. B. Sansone and P. M. Giever, "Sampling airborne solids in a duct following a 90° bend," *Journal of the Air Pollution Control Association*, vol. 17, no. 9, pp. 605–606, 1967.

[30] K. Ito, S. Kobayashi, and M. Tokuda, "Mixing characteristics of a submerged jet measured using an isokinetic sampling probe," *Metallurgical Transactions B*, vol. 22, no. 4, pp. 439–445, 1991.

[31] S. L. Soo, *Instrumentation for fluid particle flow*. Univ. Press of Mississippi, 2013.

[32] Higashitani, *Powder Technology Handbook*, 2020.

[33] R. Boothroyd, "An anemometric isokinetic sampling probe for aerosols," *Journal of Scientific Instruments*, vol. 44, no. 4, p. 249, 1967.

[34] A. Y. Varaksin, *Turbulent particle-laden gas flows*. Springer, 2007.

[35] C. T. Crowe, *Multiphase flow handbook*. CRC press, 2005.

[36] S. Vijiapurapu and J. Cui, "Performance of turbulence models for flows through rough pipes," *Applied Mathematical Modelling*, vol. 34, no. 6, pp. 1458–1466, 2010.

[37] D. C. Lim, H. H. Al-Kayiem, and J. C. Kurnia, "Comparison of different turbulence models in pipe flow of various reynolds numbers," in *AIP Conference Proceedings*, vol. 2035, no. 1. AIP Publishing LLC, 2018, p. 020005.

[38] I. B. Celik, U. Ghia, P. J. Roache, and C. J. Freitas, "Procedure for estimation and reporting of uncertainty due to discretization in cfd applications," *Journal of fluids Engineering-Transactions of the ASME*, vol. 130, no. 7, 2008.

[39] L. G. Trapp and H. G. Argentieri, "Evaluation of nacelle drag using computational fluid dynamics," *Journal of Aerospace Technology and Management*, vol. 2, pp. 145–154, 2010.

[40] T. Bykerk, D. Verstraete, and J. Steelant, "Low speed longitudinal dynamic stability analysis of a hypersonic waverider using unsteady reynolds averaged navier stokes forced oscillation simulations," *Aerospace Science and Technology*, vol. 103, p. 105883, 2020.

[41] F. Hartshorn, "Analysis of asymmetric aircraft aerodynamics due to an experimental wing glove," in *29th AIAA Applied Aerodynamics Conference*, 2011, p. 3352.

[42] C. Tropea, A. L. Yarin, J. F. Foss *et al.*, *Springer handbook of experimental fluid mechanics*.

Springer, 2007, vol. 1.

8. Conclusions and Future Outlook

This dissertation details the development of two novel instruments for use in a gas turbine engine which is undergoing solid particulate ingestion. The primary conclusions from each work and suggestions for future work are discussed below.

8.1 Conclusions

The study in Chapter 3 details the development of a gas turbine engine test cell. This test cell is designed for the express purpose of studying solid particle ingestion effects on a turboshaft engine, a one-of-a-kind capability for a university. Here, the authors provide an account of the extensive hydro-mechanical subsystems, data acquisition suite, and engine controls developed to result in a fully functional test stand. Preliminary test results are presented and emphasis is placed on analysis of particle size change at different engine locations. While not the primary focus of the dissertation work, the work contained in this chapter sets the stage for the follow-on work to occur and has helped to establish Virginia Tech as a leader in investigations of aircraft engine ingestion events.

The manuscript in Chapter 4 delves into the intricate details of a novel particle illumination technique that has been developed to effectively visualize the distribution of particles when they are entering the inlet section of a gas turbine engine. The methodology employed in this study involves the utilization of a simple setup comprised of a single laser plane and imaging camera. By using this technique, users are able to obtain both qualitative and quantitative information regarding the particle distribution. Specifically, the technique provides a reliable estimate of the particle mass flow and localized particle number density estimates. This is made possible by implementing an in-situ calibration constant that takes into account the particle mass flow rate and integrated particle intensity over the captured region, and assumes a proportionate relationship between the two variables. To the best of the authors' knowledge, although the method has certain limitations that have been duly acknowledged, it still represents a noteworthy breakthrough in the field as it is the first attempt to offer a comprehensive depiction of the particles present at the inlet section of an aircraft engine.

The research presented in Chapters 5, 6, and 7 shifts focus to the development of a physical particle sampling probe that has been specifically designed to operate within the axial compressor section of a turboshaft engine. The aim of the probe is to enable researchers to obtain a more nuanced understanding of the propensity of particles to break and the susceptibility of components to erosion, by facilitating sampling of the particles present in the gas path of the engine.

Chapter 5 provides a detailed account of three separate studies that were conducted to evaluate the performance of the probe, namely an aerodynamic study, a particle tracking study, and a particle sampling study. These studies were carried out using a free jet and allowed the researchers to establish a baseline understanding of the instrument's performance under flow conditions that are similar to those observed in an operational engine environment. The results indicated that the probe exhibited sub-isokinetic behavior throughout all tests, indicating that there was a shortfall in its aerodynamic sampling capabilities. However, this inefficiency did not have a significant impact on the probe's ability to capture the particles of interest, which were found to be traveling at high enough velocities and were large enough to be inertially dominant. The conclusion drawn by the authors was that the instrument was successful in capturing large particles at velocities that had not been previously examined, thus constituting a noteworthy advancement in the field.

Chapter 6 is a self-contained section of the report that provides a detailed description of a subsequent experiment involving the particle sampling probe previously discussed. In this study, the probe was situated at the inlet of a gas turbine engine while particles were introduced into the inlet flow at ground idle conditions. The main objective of the investigation was to evaluate whether the sampling probe could accurately estimate particle concentration and collect a representative sample of the ingested test dust. The findings yielded mixed results, indicating that a representative sample may be obtained, but it is uncertain whether the probe has been exposed to the entire range of particle sizes present in the control sample. To assess the probe's ability to predict local particle concentration, the illumination technique discussed earlier was compared with the sample collected by the probe. The results demonstrate that the concentration estimates obtained by the two methods are in good agreement, thus providing the first evidence supporting the local concentration value reported by the particle sampling probe.

The manuscript presented in Chapter 7 serves as a valuable addition to the current literature and is intended to be submitted to a journal publication at a later date. The study focused on numerical investigations aimed at further elucidating the aerodynamic deficiencies of the particle sampling probe discovered in Chapter 5. The results affirm earlier findings that the probe operates sub-isokinetically within the relevant flow regimes. Additionally, the aerodynamic performance of the probe was observed to be inversely proportional to both Mach number and yaw angle relative to the fluid freestream. A novel approach to calculate the aerodynamic efficiency parameter is presented, which may provide a more comprehensive assessment of the probe's performance under diverse flow scenarios. Furthermore, a design modification is proposed that may be of interest to future research. Transitioning from an internal chamfer design to an external chamfer design led to a more than threefold increase in aerodynamic efficiency over the previous design. These findings suggest that the proposed geometry modification could offer an attractive solution to improve the effectiveness of the particle sampling probe in future investigations for a broader range of particle sizes and flow regimes.

8.2 Outlook

The dissertation presented herein offers several opportunities for further analysis and expansion of techniques. To this end, several recommendations for future investigations are outlined below:

Particle Illumination Technique

- The full realization of the technique would include imaging a complete cross section of the inlet plane. The initial investigation attempted this but was plagued with excessive glare and reflection from a parallel study. By imaging the full inlet area, uncertainties which were present in the initial study may be reduced. Namely, the study presented in Chapter 4 assumed that all particles present in the flow were captured by the one inch laser strip which was centered on the inlet plane.
- It has been determined that the method employed may be subject to significant uncertainty when utilized to characterize a test dust containing particles of varying sizes and shapes, as is the case with C-Spec. Analysis presented in Figure 4.1 demonstrates that the intensity of scattering exhibited by a particle may differ markedly based on its size and shape. Consequently, it is recommended that future investigations take steps to minimize the potential impact of this effect, either by utilizing dust samples with a narrower particle size distribution, or by incorporating a more thorough analysis of the associated variability.
- It is recommended that future investigations focus on assessing the effectiveness of the proposed technique under conditions of increased particle density and finer particle size distributions, which may result in higher levels of measurement uncertainty. Such studies may provide valuable insights into the limitations of the technique and identify potential modifications or enhancements that can be made to improve its performance in such scenarios.

Particle Sampling Probe

- It is recommended that the computational studies presented in Chapter 7 be extended to include particle simulations. These investigations can provide valuable insight into the performance of the proposed design modification and may help address the outstanding questions surrounding the ability of the particle sampling probe to accurately assess localized concentration and sample large particles. Therefore, it is suggested that future investigations should be undertaken to study the performance of the probe under a range of particle sizes and flow conditions, and to assess the effectiveness of the proposed design modification in improving overall probe efficiency.

- The design modification presented in Chapter 7 should be manufactured and tested using the Virginia Tech 4.5 inch suction wind tunnel. Here, the prototype can be tested using a wide range of test dusts and yaw angles and a comprehensive understanding of the probe performance may be gathered. In light of the inconclusive assessment presented in Chapter 6, efforts should be made to evaluate the capability of the particle sampling instrument to effectively capture very large particles ($D_p \geq 500$ µm).
- To achieve the desired outcome of providing a local concentration estimate using the particle sampling probe, it is recommended that future research focus on the integration of the particle illumination technique, as described in Chapter 4, with the particle sampling probe. As demonstrated in Chapter 6, such an integration may offer a promising avenue for assessing the accuracy of the probe's measurement. Further exploration of this technique combination is therefore suggested as a priority for future studies.